Analysis and Damping Techniques for Torque Ripple reduction in a 24-Slot 16-Pole Fractional Slot Winding PMASynRel motor

Laureando:

Riccardo Fusar

Relatore:
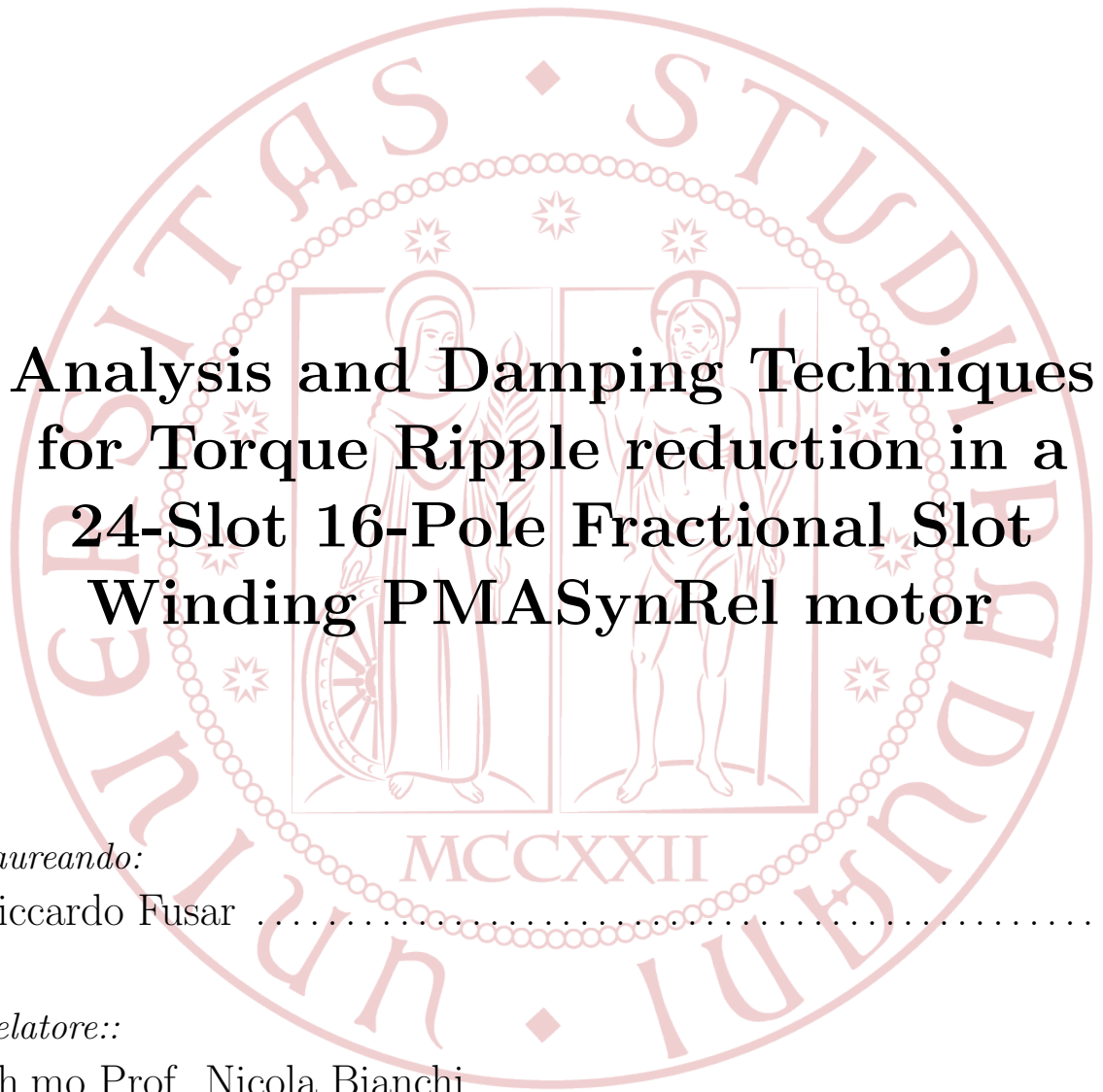
Ch.mo Prof. Nicola Bianchi

Anno accademico 2014/2015

Analysis and Damping Techniques for Torque Ripple reduction in a 24-Slot 16-Pole Fractional Slot Winding PMASynRel motor

Laureando:
Riccardo Fusar ....

Relatore::
Ch.mo Prof. Nicola Bianchi ....

A tutti coloro che mi hanno permesso di arrivare fino a qui.

Al prof. Nicola Bianchi,
che ha saputo trattarmi più da amico
che da studente.

Abstract

This work deals with a 24-Slot and 16-Pole Fractional Slot (FS) Winding Synchronous Reluctance motor, Assisted by Permanent Magnets (PMASynRel), with non-overlapped coils.
Moving from distributed to concentrated windings, a general decrease of performance occurs. In the 24/16 configuration, then, this loss is extremely heavy, especially in terms of torque ripple.

The following study has two purposes. On one hand, to look for practical design strategies able to reduce torque ripple, without modifying the average torque (or, better, increasing it). On the other hand, studies have been carried out in order to understand the reasons of the poor performance.
The thesis is split into 4 parts. After a brief recall of SynRel machines, some FS configurations are developed, starting from the distributed motor. The 24/16 motor, therefore, is analysed from the torque behaviour point of view. The second and the third parts gather a set of design strategies which act on the stator and on the rotor, respectively. They are called: Slot-Deformation, Tooth Cut, Stator Shifting, Optimization and Skewing. The last part, finally, consists on a deep analysis of the 24/16 motor. An analytical model of the machine and a possible explanation about the high torque ripple are developed.

The implemented strategies permit to reach very low values of ripple ($T_{ripple} < 10\%$), also if a reduction of the average torque can not be neglected.

Contents

Chapter 1

Background on PMARel Machines

The purpose of this chapter is to present the electrical model of Synchronous Reluctance Machines (*SynRels*), and -more generally- the model of SynRel motors assisted by inner magnets (*PMASynRels*).

A basic two-pole machine is considered and it is studied starting from a real *abc* reference frame. However, the most convenient manner of analyzing sinusoidal machines, as it is well known, uses instantaneous current, voltage and flux linkage phasors in a synchronous-rotating reference frame locked to the rotor. Therefore, the $abc \rightarrow \alpha\beta\gamma$ transformation -firstly- and the $\alpha\beta\gamma \rightarrow dq\gamma$ transformation -then- are applied to the model, in order to obtain the voltage and torque equations for the machine in the reference frame illustrated in Fig. 1.1.

This frame is drawn with the following rules: d axis identifies the minimum reluctance magnetic path, while the q axis is fixed at 90 $^{el\ deg}$ ahead the first one. In addition, the magnet (if present) is aligned with the $-q$ axis direction.
These set of conventions is known as *Reluctance Reference* and it will be used throughout the rest of this thesis.
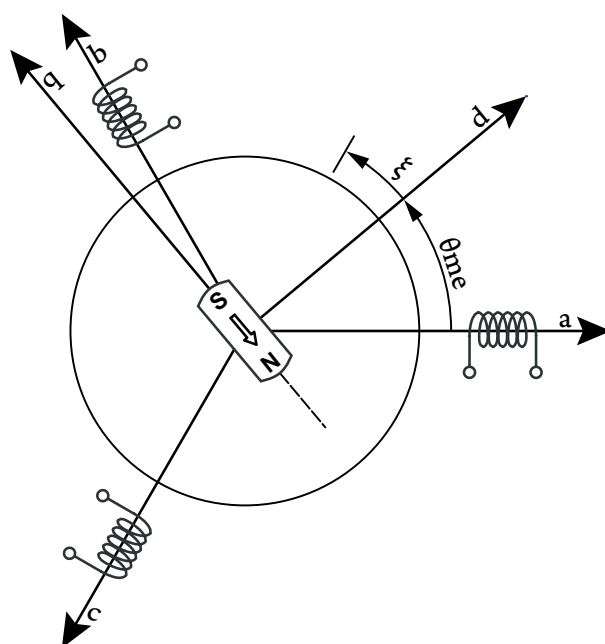

Figure 1.1: Reference frame

In the generic real *abc* reference frame, voltages can be written as:

$$
\begin{bmatrix} u_a \\ u_b \\ u_c \end{bmatrix} = [R]_{abc} \cdot \begin{bmatrix} i_a \\ i_b \\ i_c \end{bmatrix} + \frac{d}{dt} \cdot \begin{bmatrix} \lambda_a \\ \lambda_b \\ \lambda_c \end{bmatrix} = [R]_{abc} \cdot \begin{bmatrix} i_a \\ i_b \\ i_c \end{bmatrix} + \frac{d}{dt} \cdot \begin{bmatrix} \lambda_{a,i} + \lambda_{a,PM} \\ \lambda_{b,i} + \lambda_{b,PM} \\ \lambda_{c,i} + \lambda_{c,PM} \end{bmatrix} \tag{1.1}
$$

where winding resistance is the same for all the coils, while flux linkages due to the stator currents and magnets are supposed to be sinusoidally-distributed:

$$
\begin{bmatrix} R_a & 0 & 0 \\ 0 & R_b & 0 \\ 0 & 0 & R_c \end{bmatrix} = R \cdot \begin{bmatrix} 1 & 0 & 0 \\ 0 & 1 & 0 \\ 0 & 0 & 1 \end{bmatrix} \qquad \Rightarrow \qquad [R]_{abc} = R \cdot [I] \tag{1.2}
$$

$$
\begin{bmatrix} \lambda_{a,i} \\ \lambda_{b,i} \\ \lambda_{c,i} \end{bmatrix} = \begin{bmatrix} l_a(\theta_m^e) & m_{ab}(\theta_m^e) & m_{ac}(\theta_m^e) \\ m_{ba}(\theta_m^e) & l_b(\theta_m^e) & m_{bc}(\theta_m^e) \\ m_{ca}(\theta_m^e) & m_{cb}(\theta_m^e) & l_c(\theta_m^e) \end{bmatrix} \cdot \begin{bmatrix} i_a \\ i_b \\ i_c \end{bmatrix} \quad \Rightarrow \quad [\lambda_i]_{abc} = [L]_{abc} \cdot [i]_{abc} \tag{1.3}
$$

$$
\begin{bmatrix} \lambda_{a,PM} \\ \lambda_{b,PM} \\ \lambda_{c,PM} \end{bmatrix} = \begin{bmatrix} \Lambda_{PM} \cdot cos\left(\theta_m^e - \frac{\pi}{2}\right) \\ \Lambda_{PM} \cdot cos\left(\theta_m^e - \frac{\pi}{2} - \frac{2}{3}\pi\right) \\ \Lambda_{PM} \cdot cos\left(\theta_m^e - \frac{\pi}{2} + \frac{2}{3}\pi\right) \end{bmatrix} \quad \Rightarrow \quad [\lambda_{PM}]_{abc} = \Lambda_{PM} \cdot e^{j\left(\theta_m^e - \frac{\pi}{2}\right)} \tag{1.4}
$$

with self and mutual inductances which are supposed to vary sinusoidally: $[L]_{abc} =$

$$
= \begin{bmatrix} L_1 + L_2 \cdot cos\left(2\theta_m^e\right) & -\frac{L_1}{2} + L_2 \cdot cos\left[2\left(\theta_m^e - \frac{\pi}{3}\right)\right] & -\frac{L_1}{2} + L_2 \cdot cos\left[2\left(\theta_m^e + \frac{\pi}{3}\right)\right] \\ -\frac{L_1}{2} + L_2 \cdot cos\left[2\left(\theta_m^e - \frac{\pi}{3}\right)\right] & L_1 + L_2 \cdot cos\left[2\left(\theta_m^e - \frac{2\pi}{3}\right)\right] & -\frac{L_1}{2} + L_2 \cdot cos\left(2\theta_m^e\right) \\ -\frac{L_1}{2} + L_2 \cdot cos\left[2\left(\theta_m^e + \frac{\pi}{3}\right)\right] & -\frac{L_1}{2} + L_2 \cdot cos\left(2\theta_m^e\right) & L_1 + L_2 \cdot cos\left[2\left(\theta_m^e + \frac{2\pi}{3}\right)\right] \end{bmatrix}
$$

A non-orthogonal $abc \to \alpha\beta\gamma$ transformation is now applied. In (1.5) and (1.6) the transformation rules and the conversion matrix are reported. Then, the transformed inductances matrix, $[L]_{\alpha\beta\gamma}$, and the PM-fluxes array, $[\lambda_{PM}]_{\alpha\beta\gamma}$, are calculated in (1.7). Finally, the transformed voltages are derived in (1.9):

$$
\begin{cases} [u]_{\alpha\beta\gamma} &= \left[T_{\substack{abc \\ \alpha\beta\gamma}}\right]^{-1} \cdot [u]_{abc} \\ [i]_{\alpha\beta\gamma} &= \left[T_{\substack{abc \\ \alpha\beta\gamma}}\right]^{-1} \cdot [i]_{abc} \\ [Z]_{\alpha\beta\gamma} &= \left[T_{\substack{abc \\ \alpha\beta\gamma}}\right]^{-1} \cdot [Z]_{abc} \cdot \left[T_{\substack{abc \\ \alpha\beta\gamma}}\right] \\ [\lambda]_{\alpha\beta\gamma} &= \left[T_{\substack{abc \\ \alpha\beta\gamma}}\right]^{-1} \cdot [\lambda]_{abc} \end{cases} \qquad \begin{cases} [u]_{abc} &= \left[T_{\substack{abc \\ \alpha\beta\gamma}}\right] \cdot [u]_{\alpha\beta\gamma} \\ [i]_{abc} &= \left[T_{\substack{abc \\ \alpha\beta\gamma}}\right] \cdot [i]_{\alpha\beta\gamma} \\ [Z]_{abc} &= \left[T_{\substack{abc \\ \alpha\beta\gamma}}\right] \cdot [Z]_{\alpha\beta\gamma} \cdot \left[T_{\substack{abc \\ \alpha\beta\gamma}}\right]^{-1} \\ [\lambda]_{abc} &= \left[T_{\substack{abc \\ \alpha\beta\gamma}}\right] \cdot [\lambda]_{\alpha\beta\gamma} \end{cases} \tag{1.5}
$$

$$\begin{bmatrix} T_{abc} \\ {}_{\alpha\beta\gamma} \end{bmatrix} = \begin{bmatrix} 1 & 0 & 1 \\ -\dfrac{1}{2} & \dfrac{\sqrt{3}}{2} & 1 \\ -\dfrac{1}{2} & -\dfrac{\sqrt{3}}{2} & 1 \end{bmatrix} \qquad \begin{bmatrix} T_{abc} \\ {}_{\alpha\beta\gamma} \end{bmatrix}^{-1} = \dfrac{2}{3} \cdot \begin{bmatrix} 1 & -\dfrac{1}{2} & -\dfrac{1}{2} \\ 0 & \dfrac{\sqrt{3}}{2} & -\dfrac{\sqrt{3}}{2} \\ \dfrac{1}{2} & \dfrac{1}{2} & \dfrac{1}{2} \end{bmatrix} \qquad (1.6)$$

$$[L]_{\alpha\beta\gamma} = \begin{bmatrix} l_\alpha(\theta_m^e) & m_{\alpha\beta}(\theta_m^e) & 0 \\ m_{\beta\alpha}(\theta_m^e) & l_\beta(\theta_m^e) & 0 \\ 0 & 0 & l_\gamma(\theta_m^e) \end{bmatrix} \qquad [\lambda_{PM}]_{\alpha\beta\gamma} = \Lambda_{PM} \cdot \begin{bmatrix} sin(\theta_m^e) \\ -cos(\theta_m^e) \\ 0 \end{bmatrix} \qquad (1.7)$$

where: $[L]_{\alpha\beta\gamma} =$

$$= \dfrac{3}{2} \cdot \begin{bmatrix} \big[L_1 + L_2 \cdot cos(2\theta_m^e)\big] & L_2 \cdot sin(2\theta_m^e) & 0 \\ L_2 \cdot sin(2\theta_m^e) & \big[L_1 - L_2 \cdot cos(2\theta_m^e)\big] & 0 \\ 0 & 0 & 0 \end{bmatrix} \qquad (1.8)$$

$$[u]_{\alpha\beta\gamma} = \begin{bmatrix} T_{abc} \\ {}_{\alpha\beta\gamma} \end{bmatrix}^{-1} \cdot [u]_{abc} = [R]_{\alpha\beta\gamma} \cdot [i]_{\alpha\beta\gamma} + \dfrac{d}{dt}\Big([\lambda]_{\alpha\beta\gamma}\Big) =$$

$$= [R]_{\alpha\beta\gamma} \cdot [i]_{\alpha\beta\gamma} + \dfrac{d}{dt}\Big([L]_{\alpha\beta\gamma} \cdot [i]_{\alpha\beta\gamma} + [\lambda_{PM}]_{\alpha\beta\gamma}\Big) =$$

$$= [R]_{\alpha\beta\gamma} \cdot [i]_{\alpha\beta\gamma} + [L]_{\alpha\beta\gamma} \cdot \dfrac{d}{dt}\Big([i]_{\alpha\beta\gamma}\Big) + \dfrac{d\theta_m^e}{dt} \cdot \dfrac{d}{d\theta_m^e}\Big([L]_{\alpha\beta\gamma}\Big) \cdot [i]_{\alpha\beta\gamma} + \qquad (1.9)$$

$$+ \dfrac{d\theta_m^e}{dt} \cdot \dfrac{d}{d\theta_m^e}\Big([\lambda_{PM}]_{\alpha\beta\gamma}\Big) =$$

$$= [R]_{\alpha\beta\gamma} \cdot [i]_{\alpha\beta\gamma} + [L]_{\alpha\beta\gamma} \cdot \dfrac{d}{dt}\Big([i]_{\alpha\beta\gamma}\Big) + \omega \cdot [F]_{\alpha\beta\gamma} \cdot [i]_{\alpha\beta\gamma} + \omega \cdot \dfrac{d}{d\theta_m^e}\Big([\lambda_{PM}]_{\alpha\beta\gamma}\Big)$$

The purpose, now, is to lock the α and β axes' rotation and, thus, to take the windings placed along normal axes independent each others (i.e. $m_{\alpha\beta} = m_{\beta\alpha} = 0$). In order to do this, an orthogonal $\alpha\beta\gamma \to dq\gamma$ transformation [1] is implemented, with the following conversion matrix:

---

[1] The condition of orthogonality is verified when $\begin{bmatrix} \bar{T}_{\alpha\beta\gamma} \\ {}_{dq\gamma} \end{bmatrix}^{-1} = \begin{bmatrix} \bar{T}^*_{\alpha\beta\gamma} \\ {}_{dq\gamma} \end{bmatrix}^{T}$, where the symbol $\bar{T}$ means that it is considered a generic complex matrix and the symbol * means "complex conjugate".
In this case, the connection laws can be written also as:

$$\begin{cases} [u]_{dq\gamma} = \begin{bmatrix} T_{\alpha\beta\gamma} \\ {}_{dq\gamma} \end{bmatrix}^{T} \cdot [u]_{\alpha\beta\gamma} \\[2mm] [i]_{dq\gamma} = \begin{bmatrix} T_{\alpha\beta\gamma} \\ {}_{dq\gamma} \end{bmatrix}^{T} \cdot [i]_{\alpha\beta\gamma} \\[2mm] [Z]_{dq\gamma} = \begin{bmatrix} T_{\alpha\beta\gamma} \\ {}_{dq\gamma} \end{bmatrix}^{T} \cdot [Z]_{\alpha\beta\gamma} \cdot \begin{bmatrix} T_{\alpha\beta\gamma} \\ {}_{dq\gamma} \end{bmatrix} \\[2mm] [\lambda]_{dq\gamma} = \begin{bmatrix} T_{\alpha\beta\gamma} \\ {}_{dq\gamma} \end{bmatrix}^{T} \cdot [\lambda]_{\alpha\beta\gamma} \end{cases} \qquad \begin{cases} [u]_{\alpha\beta\gamma} = \begin{bmatrix} T_{\alpha\beta\gamma} \\ {}_{dq\gamma} \end{bmatrix} \cdot [u]_{dq\gamma} \\[2mm] [i]_{\alpha\beta\gamma} = \begin{bmatrix} T_{\alpha\beta\gamma} \\ {}_{dq\gamma} \end{bmatrix} \cdot [i]_{dq\gamma} \\[2mm] [Z]_{\alpha\beta\gamma} = \begin{bmatrix} T_{\alpha\beta\gamma} \\ {}_{dq\gamma} \end{bmatrix} \cdot [Z]_{dq\gamma} \cdot \begin{bmatrix} T_{\alpha\beta\gamma} \\ {}_{dq\gamma} \end{bmatrix}^{T} \\[2mm] [\lambda]_{\alpha\beta\gamma} = \begin{bmatrix} T_{\alpha\beta\gamma} \\ {}_{dq\gamma} \end{bmatrix} \cdot [\lambda]_{dq\gamma} \end{cases}$$

$$\left[T_{\alpha\beta\gamma \atop dq\gamma}\right] = \begin{bmatrix} cos(\theta_m^e) & -sin(\theta_m^e) & 0 \\ sin(\theta_m^e) & cos(\theta_m^e) & 0 \\ 0 & 0 & 1 \end{bmatrix} \tag{1.10}$$

and the voltages equation (1.9) becomes:

$$[u]_{dq\gamma} = \left[T_{\alpha\beta\gamma \atop dq\gamma}\right]^T \cdot [u]_{\alpha\beta\gamma} = [R]_{dq\gamma} \cdot [i]_{dq\gamma} + \frac{d}{dt}\left([\lambda_{dq\gamma}]\right) + \omega \cdot [J]_{dq\gamma} \cdot [\lambda_{dq\gamma}] \tag{1.11}$$

It is worth of noting that the $\alpha\beta\gamma \to dq\gamma$ transformation introduces a new term, $\omega \cdot [J]_{dq\gamma} \cdot [\lambda]_{dq\gamma}$, where:

$$[J]_{dq\gamma} = \begin{bmatrix} 0 & -1 & 0 \\ 1 & 0 & 0 \\ 0 & 0 & 0 \end{bmatrix}$$

This fact occurs because the conversion matrix, $\left[T_{\alpha\beta\gamma \atop dq\gamma}\right]$, is itself a function of variable θ_m^e. Therefore:

$$\begin{aligned}
[u]_{dq\gamma} = \left[T_{\alpha\beta\gamma \atop dq\gamma}\right]^T \cdot [u]_{\alpha\beta\gamma} &= \ldots + \left[T_{\alpha\beta\gamma \atop dq\gamma}\right]^T \cdot \frac{d}{dt}\left([\lambda]_{\alpha\beta\gamma}\right) = \ldots + \left[T_{\alpha\beta\gamma \atop dq\gamma}\right]^T \cdot \frac{d}{dt}\left(\left[T_{\alpha\beta\gamma \atop dq\gamma}\right] \cdot [\lambda]_{dq\gamma}\right) \\
&= \ldots + \left[T_{\alpha\beta\gamma \atop dq\gamma}\right]^{\cancel{T}} \cdot \left[\cancel{T_{\alpha\beta\gamma \atop dq\gamma}}\right] \cdot \frac{d}{dt}\left([\lambda]_{dq\gamma}\right) + \left[T_{\alpha\beta\gamma \atop dq\gamma}\right]^T \cdot \frac{d}{dt}\left[T_{\alpha\beta\gamma \atop dq\gamma}\right] \cdot [\lambda]_{dq\gamma} \\
&= \ldots + \frac{d}{dt}\left([\lambda]_{dq\gamma}\right) + \omega \cdot [J]_{dq\gamma} \cdot [\lambda]_{dq\gamma}
\end{aligned} \tag{1.12}$$

Being $[\lambda]_{dq\gamma} = \left([L]_{dq\gamma} \cdot [i]_{dq\gamma} + [\lambda_{PM}]_{dq\gamma}\right)$, and recognizing that the $\alpha\beta\gamma \to dq\gamma$ transformation leads the matrix $[L]_{dq\gamma}$ and $[\lambda_{PM}]_{dq\gamma}$ to take only real and constant coefficients,

$$[L]_{dq\gamma} = \begin{bmatrix} L_d & 0 & 0 \\ 0 & L_q & 0 \\ 0 & 0 & L_\gamma \end{bmatrix} = \frac{3}{2} \cdot \begin{bmatrix} L_1 + L_2 & 0 & 0 \\ 0 & L_1 - L_2 & 0 \\ 0 & 0 & 0 \end{bmatrix} \qquad [\lambda_{PM}]_{dq\gamma} = \Lambda_{PM} \cdot \begin{bmatrix} 0 \\ 1 \\ 0 \end{bmatrix}$$

then, the following voltages equations system, is immediately obtained:

$$\begin{cases} u_d = Ri_d + L_d \cdot \dfrac{di_d}{dt} - \omega L_q i_q + \omega \Lambda_{PM} \\[2em] u_q = Ri_q + L_q \cdot \dfrac{di_q}{dt} + \omega L_d i_d \\[2em] u_\gamma = Ri_\gamma \end{cases} \tag{1.13}$$

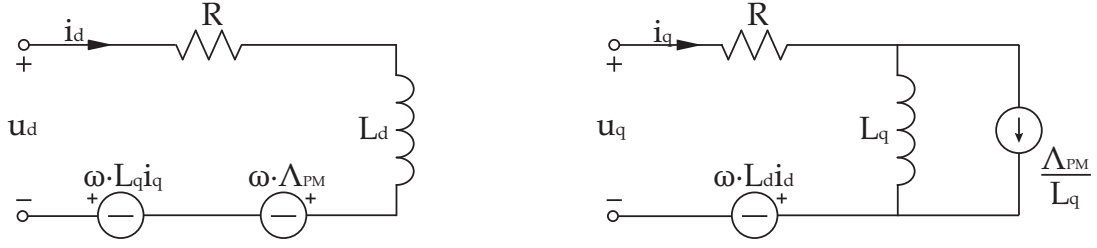In Fig. 1.2 a graphical representation of the electric circuits of $d-$axis and $q-$axis is reported.

Figure 1.2: Equivalent circuit in the $dq-$reference frame

From (1.13) it is possible to calculate the electromagnetic torque, T_{dq}, by defining the instantaneous electric power absorbed by the machine. If the adopted transformations had been been all orthogonals, the electric power has been simply calculated as:

$$p_{ist} = u_a i_a + u_b i_b + u_c i_c = u_\alpha i_\alpha + u_\beta i_\beta + u_\gamma i_\gamma = u_d i_d + u_q i_q + u_\gamma i_\gamma \tag{1.14}$$

Having used non-orthogonal transformations with not invariant power, (1.14) becomes:

$$p_{ist} = u_a i_a + u_b i_b + u_c i_c = \frac{3}{2} \cdot \left(u_\alpha i_\alpha + u_\beta i_\beta + u_\gamma i_\gamma \right) = \frac{3}{2} \cdot \left(u_d i_d + u_q i_q + u_\gamma i_\gamma \right) \tag{1.15}$$

Therefore:

$$
\begin{aligned}
p_{ist} &= \frac{3}{2} \cdot \left(u_d i_d + u_q i_q + u_\gamma i_\gamma \right) = \\
&= \frac{3}{2} \cdot \left(R i_d^2 + L_d i_d \cdot \frac{di_d}{dt} - \omega L_q i_d i_q + \omega \Lambda_{PM} i_d \right) + \\
&\quad + \frac{3}{2} \left(R i_q^2 + L_q i_q \cdot \frac{di_q}{dt} + \omega L_d i_d i_q \right) + \frac{3}{2} \cdot \left(R i_\gamma^2 \right) = \\
&= \underbrace{\frac{3}{2} R \cdot \left(i_d^2 + i_q^2 + i_\gamma^2 \right)}_{P_{Joule}} + \underbrace{\frac{3}{2} \cdot \left(L_d i_d \cdot \frac{di_d}{dt} + L_q i_q \cdot \frac{di_q}{dt} \right)}_{P_{Storage}} + \underbrace{\frac{3}{2} \omega \cdot \left(L_d - L_q \right) \cdot i_d i_q + \frac{3}{2} \omega \Lambda_{PM} i_d}_{P_{em}}
\end{aligned}
\tag{1.16}
$$

From (1.16), three different terms can be identified: the losses, P_{Joule}, a term of power associated to the stored magnetic energy into the air-gap, $P_{storage}$, and the converted power from electrical to mechanical nature, P_{em}.

P_{em} is equal to the product between the torque and the mechanical angular speed. Thus:

$$T_{dq} = \frac{P_{em}}{\omega_m} = p \cdot \frac{P_{em}}{\omega} = \underbrace{\left[\frac{3}{2} \cdot p \cdot (L_d - L_q) \cdot i_d \cdot i_q \right]}_{T_{REL}} + \underbrace{\left[\frac{3}{2} \cdot p \cdot \Lambda_{PM} \cdot i_d \right]}_{T_{PM}} \tag{1.17}$$

1.1 Reluctance component

In (1.17), two different torque components can be identified: a *cylindrical torque*, T_{PM}, due to the magnets, and a *reluctance component*, T_{REL}, associated to the presence of an anisotropy of

the rotor.

Let's consider a simple two-poles SynRel machine (i.e. with no PMs): the purpose of this Section is to fast summarize the design of reluctance component and, in particular, to understand the reason of the quite complex geometry of Fig. 1.3(a), rather than the simpler and more known geometry with saliencies of Fig. 1.3(b). The question to be answered is:

Why the machine anisotropy is not obtained through saliencies, as in Fig. 1.3(b)?

(a) SynRel Machine   (b) Machine with saliencies
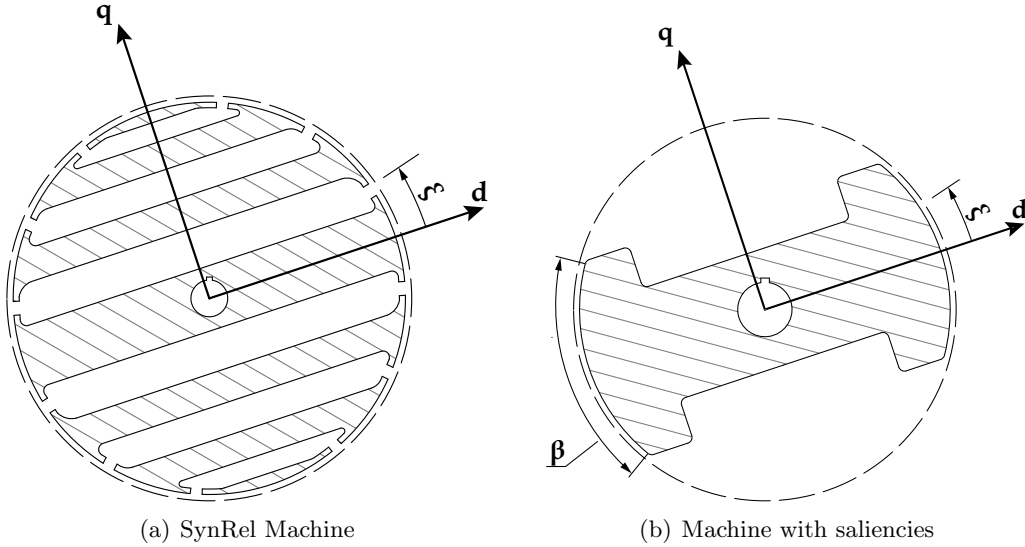
Figure 1.3: Possible synchronous anisotropic machines

Answer is immediately found by referring to the torque expression of (1.17): torque is proportional to the **difference** between the inductances of direct and quadrature axes. Therefore, the aim is to act simultaneously in order to:

1- increase the direct axis inductance, L_d;

2- reduce, as much as possible, the quadrature axis inductance, L_q.

1.1.1 Saliency rotor

Firstly, a classical solution with saliencies, as in Fig. 1.3(b), is taken into account. Magnetic linearity is assumed and the hypothesis is made (for simplicity of the analysis) that there is no flux at the air-gap except over the pole-shoe. In order to evaluate the maximum reluctance torque, it is necessary to express the L_d and L_q inductances as functions of the angular variable, β. It is the value which identifies the pitch of pole-shoes. For the following analysis, superposition principle is used and the axes d and q are considered separately.

D-AXIS. A unit $D-$axis magnetomotive force, $mmf_d \propto cos(\xi)$, is applied. In general, it is:

$$B(\xi) = \mu_0 \cdot \frac{U_s(\xi) - U_r(\xi)}{g(\xi)} \tag{1.18}$$

where: B is the flux density, μ_0 is the vacuum magnetic permeability, $(U_s - U_r)$ is the magnetic voltage drop at the gap (strictly speaking, it is a scalar magnetic potential difference between stator and rotor), and g is the gap length.

Being the gap, g, constant as ξ changes, and $(U_s - U_r) \propto cos(\xi)$, then also the flux density will be: $B_d(\xi) \propto cos(\xi)$. This is true only over the shoe, while it will be zero elsewhere, for the hypotheses done:

$$mmf_d \propto cos(\xi)$$

$$B_d \propto \begin{cases} cos(\xi) & \left[-\dfrac{\beta}{2}; \dfrac{\beta}{2}\right] \\ \\ 0 & elsewhere \end{cases}$$
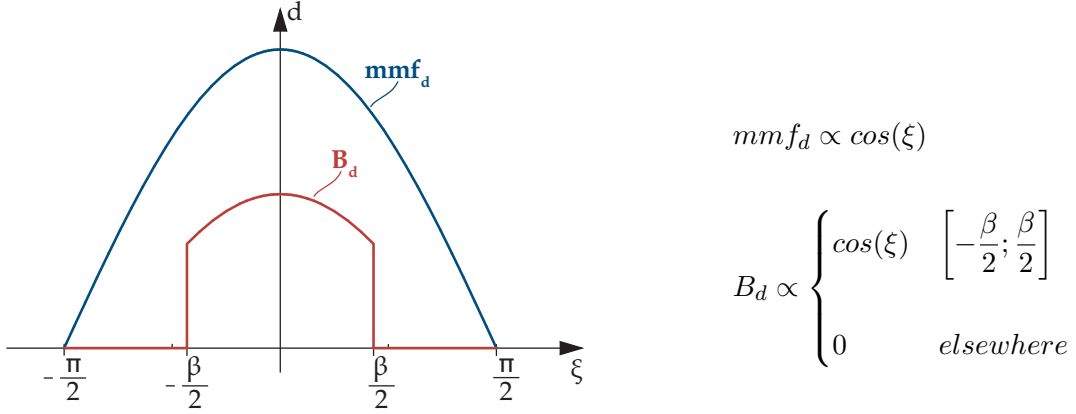
Figure 1.4: $d-$axis mmf and flux density

Defined c a constant which depends on the geometry, the direct-axis inductance is:

$$L_d = c \cdot \int_0^{2\pi} mmf_d \cdot B_d \cdot d\xi = 2c \cdot \int_{-\beta/2}^{+\beta/2} cos^2(\xi) \cdot d\xi = 2c \cdot \left(\frac{\beta}{2} + \frac{1}{2}sin(\beta)\right) = c \cdot \left(\beta + sin(\beta)\right)$$

Q-AXIS. The same considerations are now repeated when a $Q-$axis magnetomotive force, $mmf_q \propto sin(\xi)$, is applied. By referring to the same reference frame, as previously, magnetomotive-force, mmf_q, and flux density, B_q, will be as in Fig. 1.5. Then, the computation of L_q inductance will be derived below:

$$mmf_q \propto sin(\xi)$$

$$B_q \propto \begin{cases} sin(\xi) & \left[0; \dfrac{\beta}{2}\right] \\ \\ 0 & \left[\dfrac{\beta}{2}; \dfrac{\pi}{2}\right] \\ \\ symmetric & elsewhere \end{cases}$$

Figure 1.5: $q-$axis mmf and flux density

$$L_q = c \cdot \int_0^{2\pi} mmf_q \cdot B_q \cdot d\xi = 4c \cdot \int_0^{\beta/2} sin^2(\xi) \cdot d\xi = 4c \cdot \left(\frac{\beta}{4} - \frac{1}{4}sin(\beta)\right) = c \cdot \left(\beta - sin(\beta)\right)$$

7

The developed torque will be a function of the angle β, and its maximum value will be reached when $sin(\beta) = 1$:
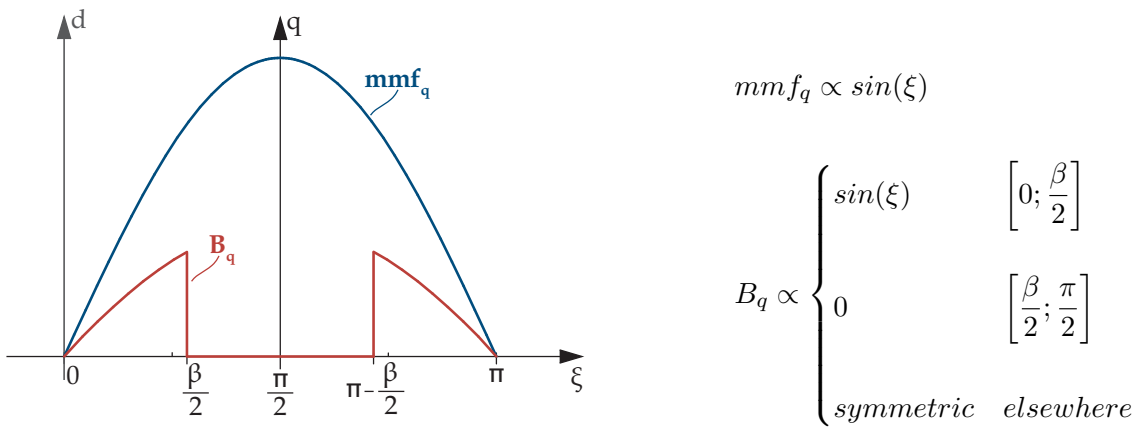
$$T_{dq,REL}(\beta) = \frac{3}{2}p \cdot \left(L_d - L_q\right) \cdot i_d i_q = \frac{3}{2}p \cdot c \cdot \left(\cancel{\beta} + sin(\beta) - \cancel{\beta} + sin(\beta)\right) \cdot i_d i_q =$$
$$= \frac{3}{2}p \cdot c' \cdot sin(\beta) \cdot i_d i_q$$

Ultimately, in order to obtain the maximum torque from the reluctance motor with saliencies, a pole-shoe with a span of $\beta = \dfrac{\pi}{2}$, that is an half of the pole pitch, is necessary. With this value of β, however, a very low *saliency ratio* of $\dfrac{L_d}{L_q} = 4.5$ is obtained[2].

This fact implies some consequences: on one hand, power factor, $cos(\varphi)$, is very low and, so, an oversizing design of the inverter is necessary; on the other one, torque, too, is influenced because -also if the difference $(L_d - L_q)$ is optimal- the direct axis inductance remains low.

From this considerations, two design goals, which must be verified simultaneously, are fixed:

- to maximize L_d (up to values as close as possible to the induction motor ones);

- to minimize L_q (up to values as low as possible).

1.1.2 SynRel rotor

These two conditions are pretty well verified by the *SynRel* machine, which has a rotor geometry as in Fig. 1.3(a). A detailed theory of the multiple-barrier *SynRel* rotors can be found in [1,2]. Only an introduction of this theory is reported here.

Let's consider a SynRel two-poles and single-barrier motor. The procedure is similar to the previous one: a slotless machine is considered and the real windings are substituted by a *mmf* distribution at the gap. The problem is split in two parts and the superposition principle is used.

D-AXIS. The first step is to fed the motor with a $D-$axis magnetomotive force, $mmf_d \propto cos(\xi)$. A convenient way to understand what happens is the $d-$axis equivalent magnetic circuit, which is reported in Fig. 1.6. Here, a cross section of the rotor is illustrated, while the dashed line defines the inner diameter of the stator. Obviously, the air-gap is not in scale, because there was the necessity of space to put the gap reluctances, R_g. With circles the mmf_d generators are indicated, while arrows identify the fluxes paths. The symbol of "earth" corresponds to the reference zero potential, and the symbol of "resistance" means "reluctance".

The figure shows the same behaviour for all the three portions of the rotor: the magnetic circuits are characterized only by the gap reluctance, R_g, which doesn't change along the gap. Assuming there are no magnetic drops into the iron, all the rotor is at the same magnetic scalar potential, with respect to the stator: $U_r = 0A$ everywhere.

---

[2]This number, in any case, is an optimistic appraisal, valid only for an ideal motor with all the hypotheses mentioned above. For the applications to whom this motor is intended, possible reference values of the saliency ratio could be: $\dfrac{L_d}{L_q} \approx 20$.
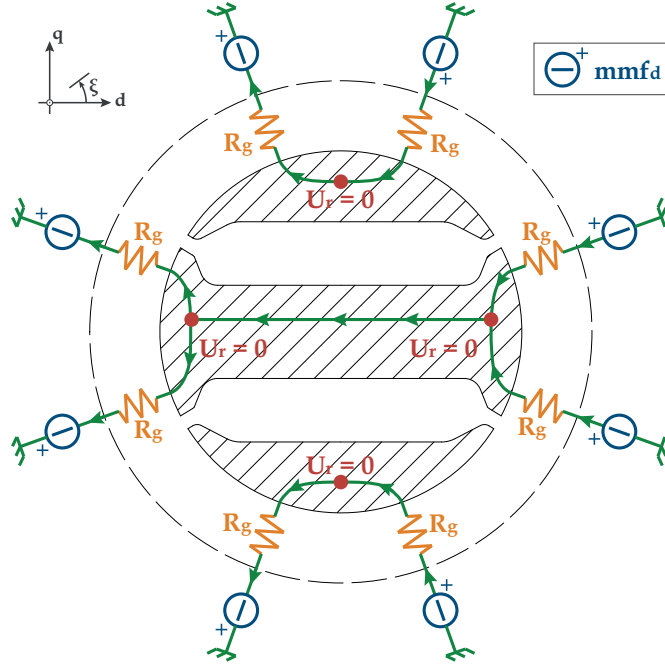
Figure 1.6: $d-$axis equivalent magnetic circuit

Fluxes follow trajectories as in figure and they are limited only by the gap reluctances. This implies that the $D-$axis inductance remains high: $L_d|_{SynRel} \to L_d|_{IND}$.

Analytically, it is the same of what has been done for the saliency rotor: because of g is constant and $U_r = 0A$ everywhere, the flux density has a sinusoidal behaviour, for (1.18). Then:

$$L_d = c \cdot \int_0^{2\pi} mmf_d \cdot B_d \cdot d\xi = c \cdot \int_0^{2\pi} cos^2(\xi) \cdot d\xi = c \cdot \pi$$

Q-AXIS. When, instead, a $Q-$axis magnetomotive force, $mmf_q \propto sin(\xi)$, is applied, the motor behaves as in Fig. 1.7, while the equivalent magnetic circuit becomes as in Fig. 1.8:

(a) 2-poles 1-barrier SynRel rotor

(b) $Q-$axis mmf and reaction function

Figure 1.7: Possible synchronous anisotropic machines

9

Figure 1.8: $q-$axis equivalent magnetic circuit

If the motor is analysed as ξ changes from 0 to π, referring to the meaning of letters a and b as in Fig. 1.7(a), it is:
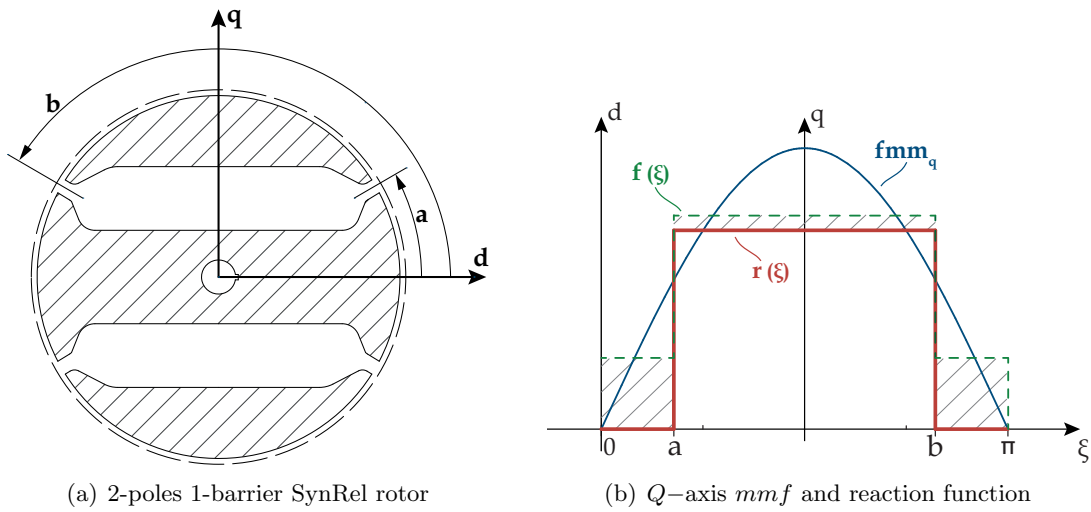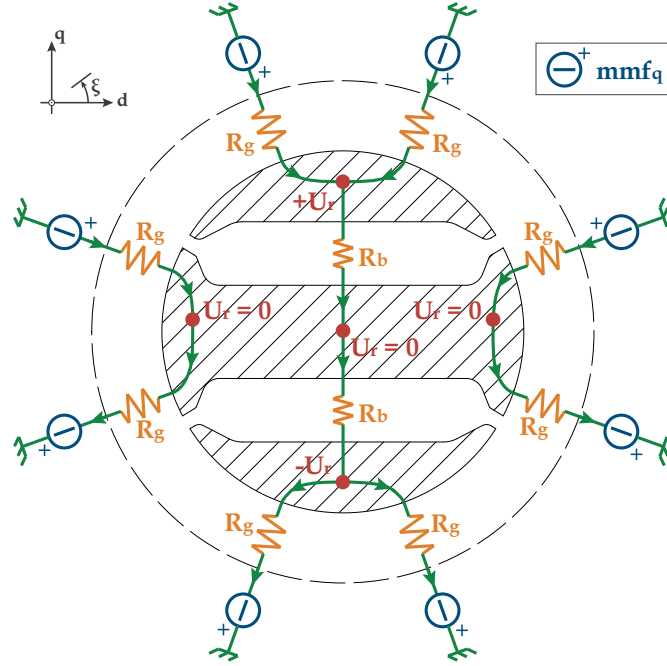
- for $\xi = [0; a[$, the rotor portion over this angles is the central one. Here, the circuit is characterized by two mmf generators (on the right of Fig. 1.8) which drive the flux in the same anticlockwise direction. Therefore, the only magnetic voltage drops are related to the gap reluctance, R_g (which is constant over the interval) and the rotor magnetic scalar potential remains null. If the values of U_r are considered as a function of the variable ξ, a new function, $r(\xi)$, called *reaction*, can be defined. It is highlighted with a thick and red line in Fig. 1.7(b) and, since here U_r is always zero, also $r(\xi) = 0$ for $\xi = [0; a[$;

- for $\xi =]a; b[$, the rotor portion interested is the upper "island". Here, the mmf generators are set so that the fluxe can't close itself directly: the only possibility is to pass through the air barriers, as illustrated.
  Doing it, the scalar magnetic potential will be zero when the flux passes through the central rotor portion, while it must be positive in the upper island and negative in the lower island. This implies that, for $\xi =]a; b[$ it is: $r(\xi) = +U_r$;

- for $\xi =]b; \pi]$, the same situation of the first point is obtained.

Now, the computation of L_q is simplified if the inductance is seen as the sum of two contribution: an inductance due to the circulating fluxes around the ribs (not considered here) and a second inductance linked to the flux which flows through the barriers. The flux density due to this latter component can be written as:

$$B_{f,q}(\xi) = f(\xi) - r(\xi) \tag{1.19}$$

where: $B_{f,q}$ means "Flowing through the barriers" flux density, $f(\xi)$ is a function[3], set up by the average values of $sin(\xi)$ over each angular interval cited above, while $r(\xi)$ is the *reaction*.

---

[3]The function $f(\xi)$ is highlighted in Fig. 1.7 with a dashed green line.

The inductance, then, can be approximated as:

$$L_q = c \cdot \int_0^{2\pi} mmf_q \cdot B_q \cdot d\xi \approx c \cdot \int_0^{2\pi} mmf_q \cdot B_{f,q} \cdot d\xi = c \cdot \int_0^{2\pi} sin(\xi) \cdot [f(\xi) - r(\xi)] \cdot d\xi$$

The difference $[f(\xi) - r(\xi)]$ is very low (especially for $\xi =]a;b[$) and, thus, L_q will be low, too.

Definitively: thanks to the magnetic insulation of the rotor pieces, due to the rotor barriers, two different values of L are obtained: an **high** L_d, because the fluxes flow only into the iron (except for the gap), where there are negligible magnetic drops, and a **low** L_q, because flux is forced to flow through the air barriers, increasing a lot the total reluctance of the circuit.
A reference value of the saliency ratio, in this case, could be: $L_d/L_q \approx 15$. This is greater than the saliency ratio found for the saliency rotor, and this is the confirmation of the better quality of SynRel motors, respect to the saliency ones.

1.2   SynRel or PMASynRel?

In general, the cylindrical torque contribution, T_{PM}, is rather scarce. It is due to the fact that, in this kind of machines, magnets of poor quality (ferrites) are generally employed. At this point, a spontaneous question should be suggested:

> *Why the presence of (however expensive) magnets into the machine, if they don't imply sensible advantages to the torque?*

In PMASynRel motors, magnets have not the main purpose of giving a contribution in terms of torque: they are used to increase the quality of the machine's performances, especially in terms of power factor, $cos(\varphi)$, which is generally low in reluctance machines.

Magnet can be simply seen as a current generator. The flux produced by the magnet, Λ_{PM}, closes itself through the rotor ribs, saturating them. Thus, it is no more necessary to draw upon the magnetizing stator current: by reducing this current, also the inductance L_q decreases and -thus- the absorption of reactive power, too, is limited.

Another way to explain the presence of the magnets is the graphical one. Let's consider the working points **A** and **B** reported in Fig. 1.9:
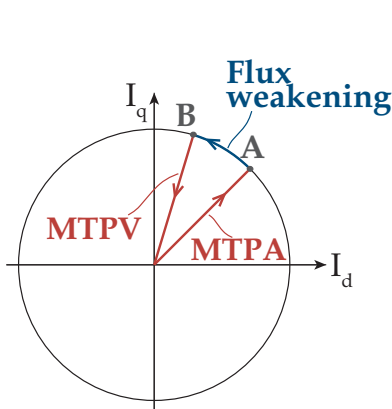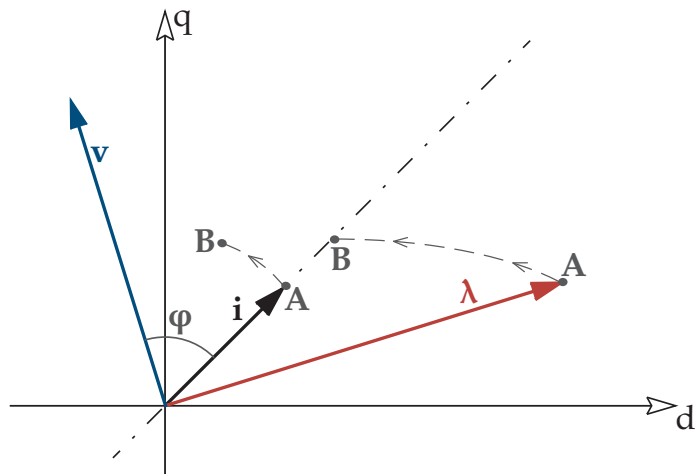

Figure 1.9: Working points

Figure 1.10: Vector diagram with no PMs

The first one identify the MTPA working point of the machine, from the zero-speed condition up to the achievement of the base speed. Beyond the latter, the motor can still work, but only in flux-weakening conditions, which are highlighted in blue (from **A** to **B**). Once the flux-weakening reaches the voltage limit, the machine is forced to reduce the magnitude of the current vector, and -thus- the MTPV trajectory is traveled.

Let's focus, now, on the MTPA working point, **A**.
As it can be seen in Fig. 1.10, a SynRel machine with no magnets is characterized by a flux vector, $\bar{\lambda}$, rather far from the direct axis. Since that, for the Faraday-Newmann law, it is:

$$\bar{v} = \frac{d\bar{\lambda}}{dt} = j\omega\bar{\lambda} \tag{1.20}$$

the voltage phasor must be at 90 $^{el\ deg}$ ahead the flux one, at a distance φ from the current. This angle (the phase shift between $\bar{v}$ and $\bar{i}$) is wide and, therefore, a low power factor is obtained. Other remark: as it is highlighted by dotted grey curves in Fig. 1.10, the flux and current vectors move themselves while the machine works in flux-weakening conditions. In particular, the flux phasor follows an elliptical trajectory up to the intersection of the plane bisector, while the current rotates, from the bisector until a position $\in]45;90[\ ^{deg}$.
From these considerations, it follows that the **B** point must be exist and -consequently- the flux-weakening range is limited.

If, now, the magnets are added into the rotor barriers, with the *Reluctance Reference* conditions (i.e. $\bar{\lambda}_{PM}$ along $-q$ direction), the working points and the phasor diagram of Fig. 1.9 and Fig. 1.10, change as follow:
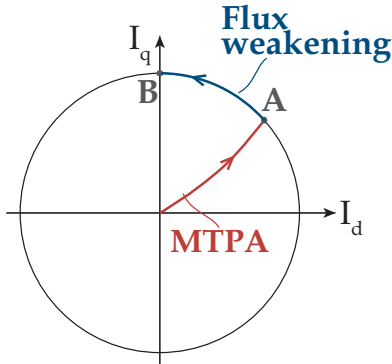
Figure 1.11: Working points
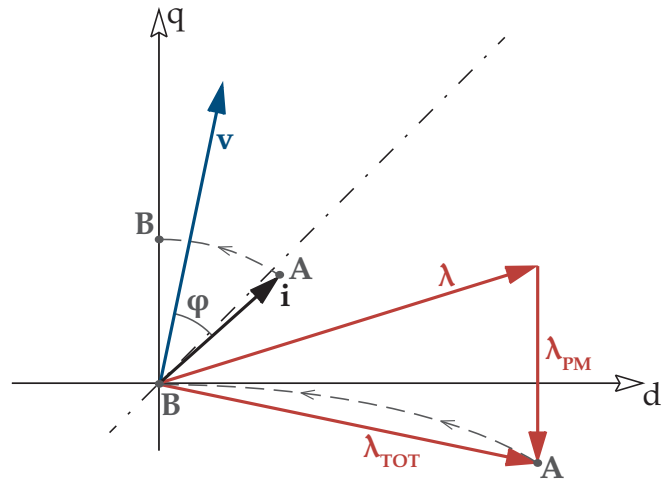
Figure 1.12: Vector diagram with PMs

The flux due to the magnet, $\bar{\lambda}_{PM}$, combines itself with the stator one, $\bar{\lambda}$. The result of these vector sum is the total flux, $\bar{\lambda}_{TOT}$.
The effect of this clockwise rotation, in terms of power factor, is immediately clear if the voltage phasor is observed, instead of talking about the flux vector. The rotation of these two quantities is the same because they are strictly linked each others. Thus, also the voltage phasor rotates itself in clockwise direction and the angle φ reduces itself. The power factor, therefore, increases. In addition, from the point of view of flux-weakening behaviour of the machine, it is worth noting that, with an appropriate design of the magnets, it is possible to create a vector, $\bar{\lambda}_{TOT}$, with

an elliptical trajectory located totally in the $+d/-q$ plane. In this case, the ellipse crashes with the bisector only in the origin, (0;0). In other words: with the supplement of magnets, the working points' chart changes, too, because they extend the flux-weakening operation of the machine so much that the MTPV trajectory disappears.

1.3 Summary and conclusions

A PMASynRel motor is an electric machine which uses both, reluctance and magnets, in order to produce torque. This latter is derived in (1.17) and reported here:

$$T_{dq} = p \cdot \frac{P_{em}}{\omega} = \left[\frac{3}{2} \cdot p \cdot (L_d - L_q) \cdot i_d \cdot i_q \right] + \left[\frac{3}{2} \cdot p \cdot \Lambda_{PM} \cdot i_d \right]$$

The presence of magnets is not particularly important from the point of view of torque development, but their presence into the rotor barriers implies:

- an improvement of the power factor, $cos(\varphi)$;

- an extension of the flux-weakening working range;

- a shift of the short circuit current value (i.e. the center of voltage limit curve) toward the $q-$axis;

- a consequent convergence of the MTPV trajectory into a point.

It is important to note, finally, that the dq-torque, T_{dq}, written above is the answer to a very simplified problem: strong hypotheses have been done, as the magnetic linearity and perfectly sinusoidal fields and distributions at the air-gap. These restrictions lead to correct appraisals of the average torque, but the same cannot be said for the torque ripple.
This is the reason why, henceforth, developed torque will be calculated through the finite element analysis and, in particular, via Maxwell Stress Tensor's method, rather than through the analytical expression, T_{dq}.

Chapter 2

Work introduction

This thesis is inserted into the research activity of University of Padua's Electrical Drives Laboratory and, in particular, it is the continuation of a study commissioned by ABB Italia S.p.a. - Discrete Automation and Motion Division.
The company's request consists on the sizing and the design of PMASynRel motors intended to lift applications. The aim is to understand if better results are possible, with respect on the current technology (SPM with rare earths), in terms of performances or -alternately- in terms of cheapness, with no excessive lost of performances.

At the beginning of this work, some designs had already been done and the best found solution consisted on a 72-slot 16-pole PMASynRel with distributed windings. This solution will be called **Motor #1** into this report, for simplicity.

From it, the nature of winding has been changed and fractional-slot motors with non-overlapped coils (i.e. $y_q = 1$) have been studied. The advantages of fractional-slot machines are beyond the scope of this research and [3] can be used as a considerable reference.
To begin with, all the possible combinations of slots and poles have been defined. They are reported in Tab. 2.1:

Q	$2p$	q	y_q	t
18	16	0.3750	1	2
21	16	0.4375	1	1
24	16	0.5000	1	8
27	16	0.5625	1	1
30	16	0.6250	1	2

Table 2.1: Possible fractional-slot motors

Between them, only the first three have been taken into account, here. Following, a fast exposition of the analysed motors is presented.

2.1   Motor #1

Motor #1 is a 72/16 PMASynRel motor with distributed windings. It is made up with a Terni lamination and Ferrite magnets. Its geometrical data are reported in Tab. 2.2, while in Fig. 2.1 these data are illustrated:
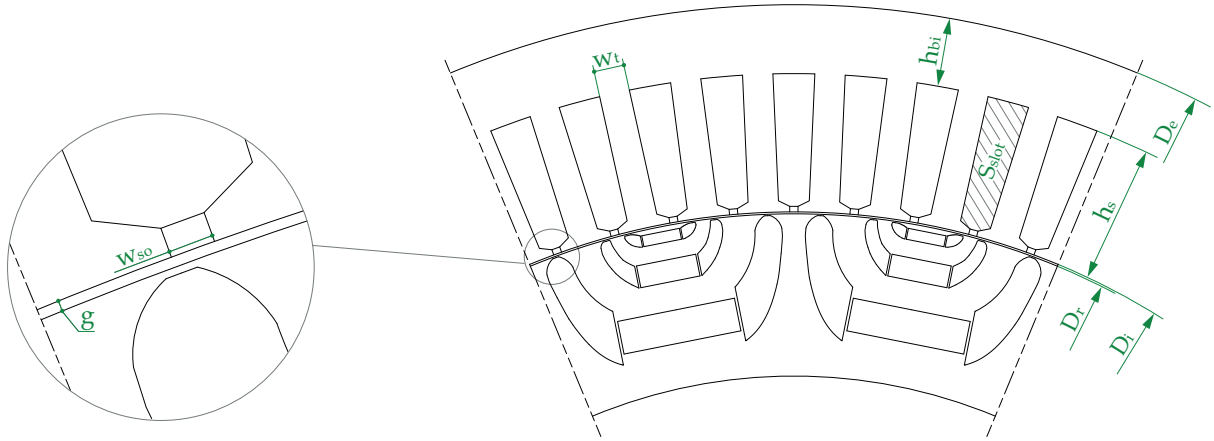
Figure 2.1: Motor #1 Cross Section

Stator				**Rotor**			
D_e	650	mm	External diameter	D_r	498.6	mm	Rotor diameter
D_i	500	mm	Stator inner diameter	D_f	200	mm	Rotor inner diameter
Q_s	72	$[-]$	Slot number	b	3	$[-]$	Number of barriers
S_{slot}	621	mm^2	Slot cross section area	**Other**			
w_t	11	mm	Tooth width	$2p$	16	$[-]$	Pole number
w_{so}	3	mm	Slot opening width	L_{stk}	235	mm	Stack length
h_s	50	mm	Slot height	g	0.7	mm	Air-gap thickness
h_{bi}	25	mm	Stator yoke height	m	3	$[-]$	Phase number

Table 2.2: Motor #1 data

This motor has been simulated by means of the freeware FE software FEMM®, in order to obtain an appraisal of torque behaviour. To do this, the same following procedure is applied for all the motors of this work:

1. firstly, the designed machine is simulated in off-load conditions and with the change of mechanical rotor position, θ_m. This operation is called *rotor alignment* and it has got the aim:

   - to know where the $d-$ and $q-$ axes are with respect to the *abc* steady state reference frame;

   - to ensure that the fluxes produced by the currents and the magnets are properly oriented (according to *Reluctance Reference*).

2. secondly, the MTPA working point is researched. The current vector angle, α_{ie}, is varied while the rotor mechanical angle is kept fixed (machine is always simulated in position $\theta_m = 0^{deg}$). The result consists on a graph where the torque trend is plotted with respect to the α_{ie} angle. The value of the latter, for which the maximum torque is obtained (hereafter called $\alpha_{ie,opt}$), identifies the MTPA working point;

3. finally, machine is simulated as the mechanical rotor position changes, in conditions under load, i.e. while the current vector has an amplitude different from zero and it is rotated locked to the rotor at the fixed shift angle, $\alpha_{ie,opt}$. Obviously, it is not necessary to rotate the rotor completely: simulations are characterized by a rotation of 180 or 360 electrical degrees, that correspond to:

$$\theta_m = \frac{\theta_{me}}{p} = \frac{\theta_{me}}{8} \qquad \Rightarrow \qquad \begin{array}{l} 180 \; ^{el\ deg} = 22.5 \; ^{deg} \\ 360 \; ^{el\ deg} = \;\;\; 45 \; ^{deg} \end{array}$$

Results in Fig. 2.2 and Fig. 2.3 are referred to Motor #1, fed by a current phasor of amplitude $|\bar{I}| = 1200A$:
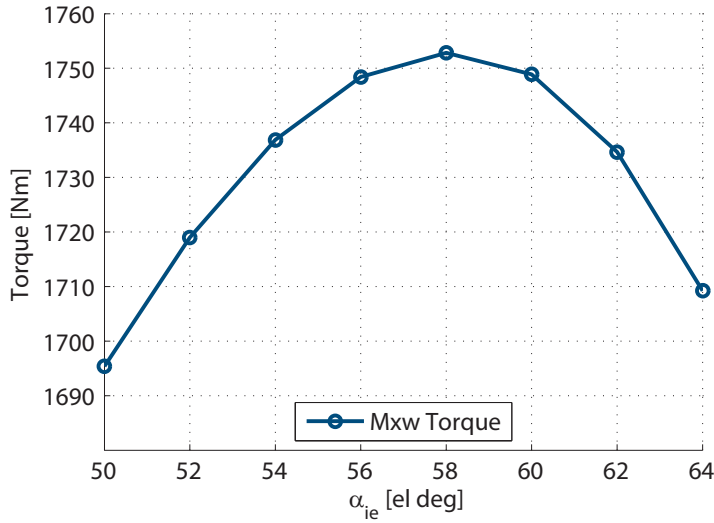
The maximum torque is developed at a current angle of $\alpha_{ie,opt} = 58 \; ^{el\ deg}$. Therefore it is the value with whom simulations will be implemented.
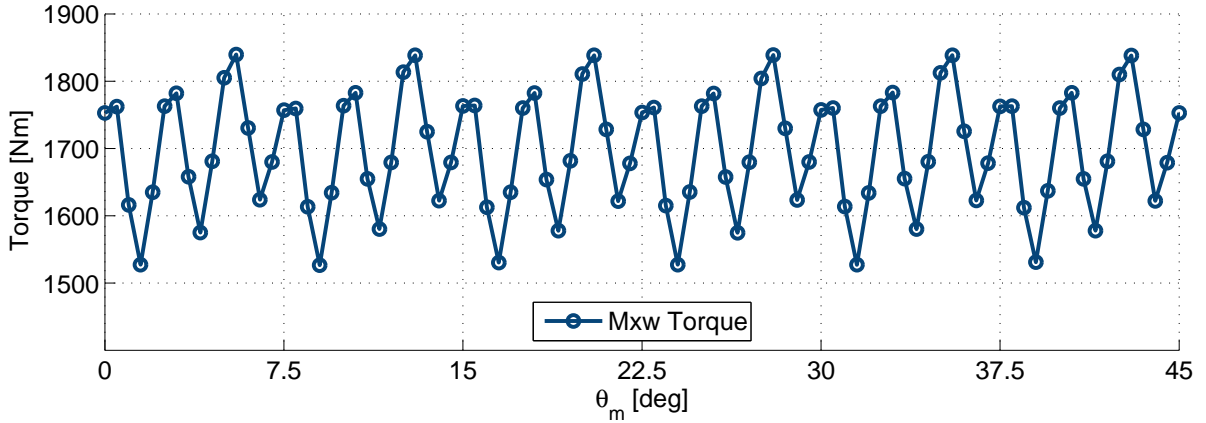
Figure 2.2: MTPA working point research

Figure 2.3: Motor #1 torque ripple at $\alpha_{ie} = 58 \; ^{el\ deg}$

Fig. 2.3 shows the torque ripple developed by the motor. Here it is possible to note how the machine presents an high value of average torque and a relatively low ripple. In particular:

- Average Torque developed: $T_{avg} = 1696Nm$

- Torque Ripple: $T_{ripple} = 18.45\%$

17

2.2 Fractional-slot motors

2.2.1 18-Slot 16-Pole configuration

18-Slot 16-Pole PMASynRel motor has the same geometric characteristics of Motor #1: for a better comparison, in fact, only the slots number -and consequently their cross section area- are adapted, while all the other parameters remain unchanged. Slot currents are modified in order to maintain the same electric loading. Therefore, if $k_{w,i}$ is the winding factor of the i-th motor, it is:

$$|\bar{I}|_{18/16} = |\bar{I}|_{72/16} \cdot \frac{Q_{S,\ 72/16}}{Q_{S,\ 18/16}} \cdot \frac{k_{w,\ 72/16}}{k_{w,\ 18/16}} = 1200 \cdot \frac{72}{18} \cdot \frac{0.945214}{0.945214} = 4800A$$

Following, a motor cross section is illustrated in Fig. 2.4, while in Tab. 2.3 its geometrical data are reported. Data which change with respect on Motor #1 are highlighted in bold and red:
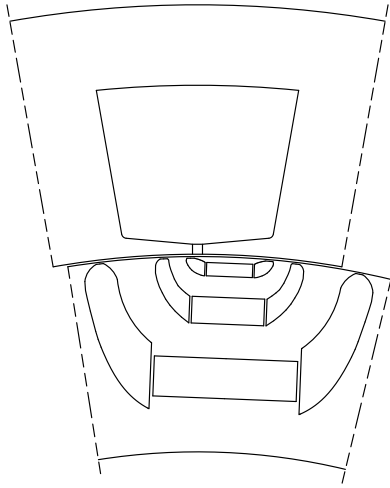
Figure 2.4: 18/16 Cross section

Stator			
D_e	650	mm	External diameter
D_i	500	mm	Stator inner diameter
Q_s	**18**	**[−]**	**Slot number**
S_{slot}	**2454**	mm^2	**Slot cross section area**
w_t	**44**	mm	**Tooth width**
w_{so}	3	mm	Slot opening width
h_s	50	mm	Slot height
h_{bi}	25	mm	Stator yoke height
Rotor			
D_r	498.6	mm	Rotor diameter
D_f	200	mm	Rotor inner diameter
b	3	[−]	Number of barriers
Other			
$2p$	16	[−]	Pole number
L_{stk}	235	mm	Stack length
g	0.7	mm	Air-gap thickness
m	3	[−]	Phase number

Table 2.3: 18/16 data

Figure 2.5: 18/16 torque ripple at $\alpha_{ie} = 40 \ ^{el\ deg}$

18

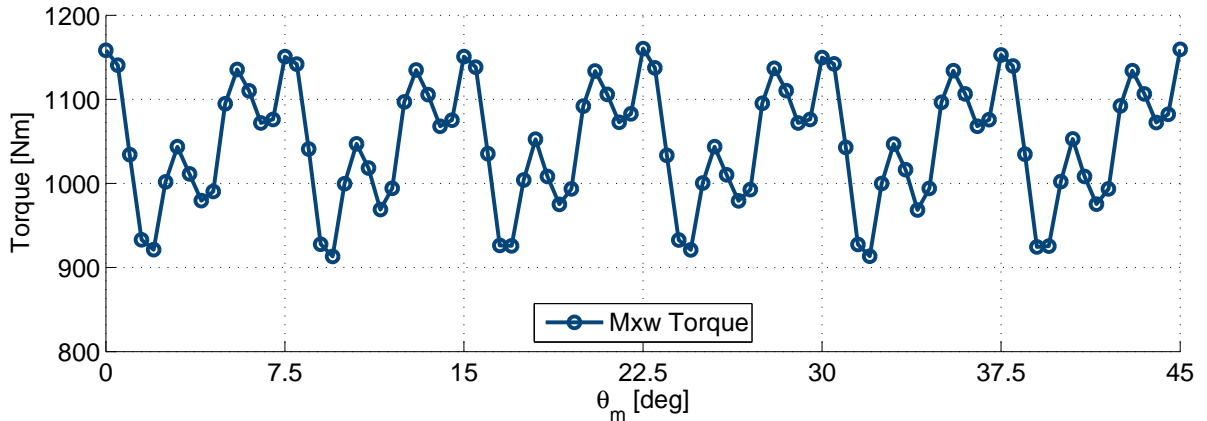It is immediately clear how the passage from distributed windings to concentrated ones implies a sensible reduction of the average torque, while ripple seems to keep low values. As a matter of fact, average torque is now $T_{avg} \approx 1049 Nm$, while ripple increases a few: $T_{ripple} = 22.37\%$.

An explanation of these high torque decrease is possible, by observing how the motor behaves over each pole. If torque is derived through a linear integral of the Maxwell Stress Tensor, where the way consists on an arc (at the air-gap) of length $360/18 = 20$ ^{deg} (that is the pole pitch), it is possible to split the total average torque into its contributions due to each pole. Since 18/16 PMASynRel motor has periodicity 2, the split has been led only for an half of the machine. Results are highlighted in Fig. 2.6 for $\alpha_{ie} = 40$ $^{el\ deg}$ and $\theta_m = 1$ ^{deg}:
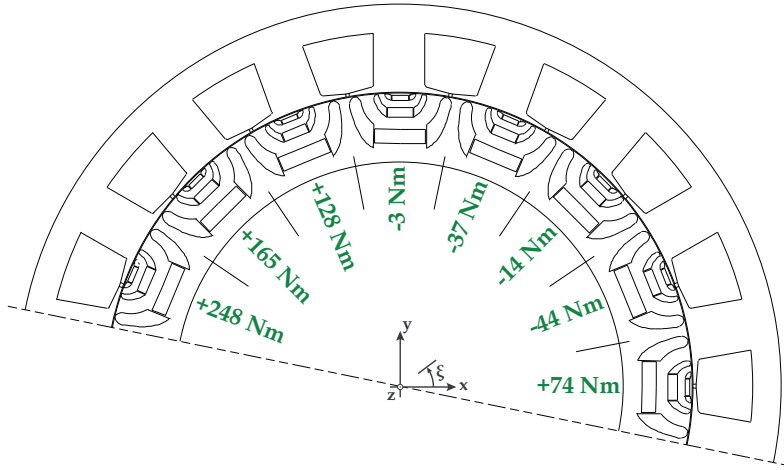

Figure 2.6: 18/16 torque contribution over each pole

NOTE: The analysis has been carried out for all the rotor mechanical positions, θ_m. The situation of figure is similar for all the angles, and this is the reason why only one θ_m is here taken into account. Fig. 2.6, in other words, can be considered as a description of the problem of torque for all the simulated rotor positions.

The reduction of slot number leaves a lot of space with teeth, and -thus- flux lines close themselves wrongly. The consequence is that each pole of the machine pushes or pulls rotor in a different way. It would expect that every pole tends to rotate the rotor in the same direction and, possibly, also with the same power. In this case, instead, there are some poles which pull the rotor in the correct direction (anti-clockwise rotation, signed with a +, in figure) and there are others which pull in the opposite way (signed -).
The sum of these contributions is still positive (in the sense of anti-clockwise rotation), but obviously the average value of torque is reduced.

2.2.2 21-Slot 16-Pole configuration

The same analysis has been developed for a 21-Slot 16-Pole PMASynRel motor and the considerations done for the previous motor are still effective. In this case, the magnitude of current vector is:

$$|\bar{I}|_{21/16} = |\bar{I}|_{72/16} \cdot \frac{Q_{S,\ 72/16}}{Q_{S,\ 21/16}} \cdot \frac{k_{w,\ 72/16}}{k_{w,\ 21/16}} = 1200 \cdot \frac{72}{21} \cdot \frac{0.945214}{0.889748} \approx 4370A$$

Following, the same informations shown for the 18/16 motor are reported and updated:
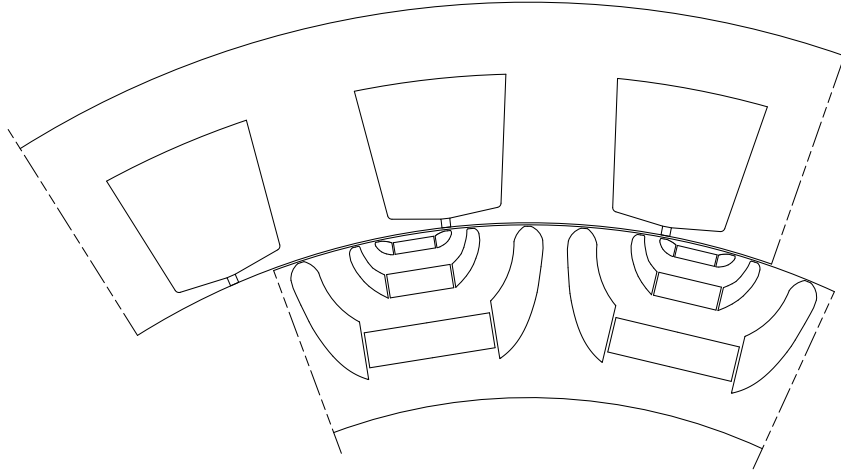

Figure 2.7: 21/16 Cross section

| **Stator**				**Rotor**			
D_e	650	mm	External diameter	D_r	498.6	mm	Rotor diameter
D_i	500	mm	Stator inner diameter	D_f	200	mm	Rotor inner diameter
Q_s	**21**	$[-]$	**Slot number**	b	3	$[-]$	Number of barriers
S_{slot}	**2084**	mm^2	**Slot cross section area**	**Other**			
w_t	**38**	mm	**Tooth width**	$2p$	16	$[-]$	Pole number
w_{so}	3	mm	Slot opening width	L_{stk}	235	mm	Stack length
h_s	50	mm	Slot height	g	0.7	mm	Air-gap thickness
h_{bi}	25	mm	Stator yoke height	m	3	$[-]$	Phase number

Table 2.4: 21/16 data
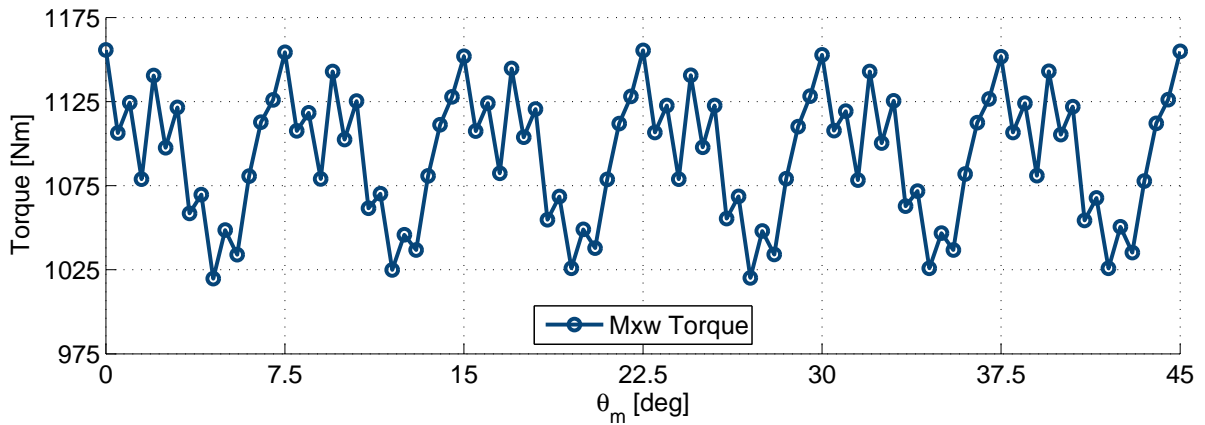
Figure 2.8: 21/16 torque ripple at $\alpha_{ie} = 39$ $^{el\ deg}$

Here, too, there are reductions of the average torque and a low ripple: $T_{avg} \approx 1093Nm$ and $T_{ripple} \approx 12.40\%$, respectively.

20

The situation is very similar to the previous one and this leads to think that the same results will be found from the total average torque split. In this case, however, machine periodicity is equal to unity (i.e. $t = 1$). Therefore, the overall machine must be analysed:
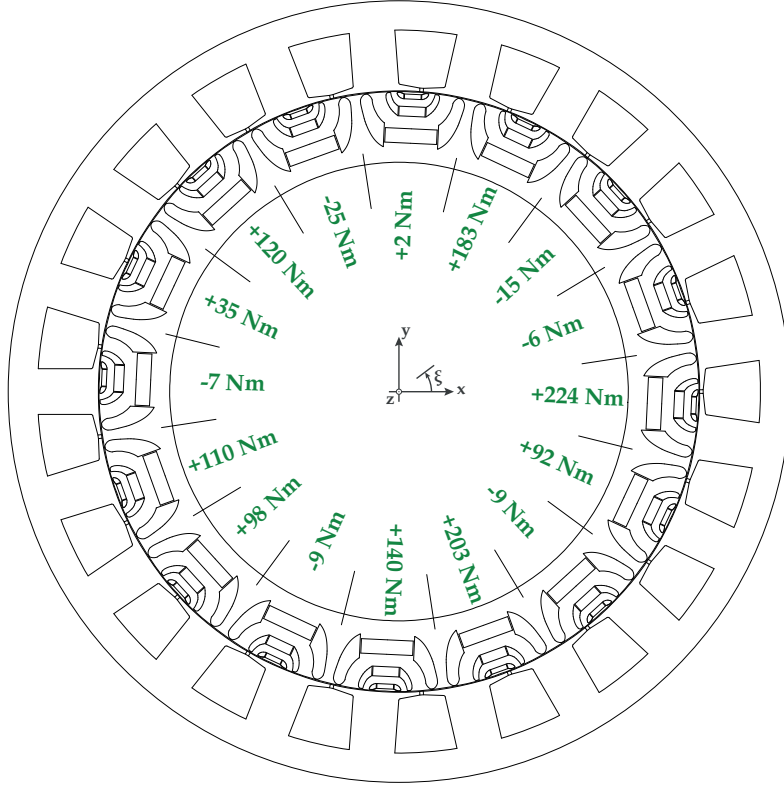

Figure 2.9: 21/16 torque contribution over each pole ($\theta_m = 2^{\ deg}$)

As expected, here too, there is a motor's behaviour where some poles work forward and others backward, getting the rotor to rotate clockwise.

2.2.3   24-Slot 16-Pole configuration

Last designed machine is a 24/16 PMASynRel motor. It distinguishes itself from the previous ones for its high periodicity ($t = 8$). This particular, as it will be possible to note further, leads to different considerations and different results, which are the opposite respect to what has been seen until now. In particular, machine has an average torque rather high: its decrease is around -25% of the Motor #1 's one (in the previous motors, torque reduction reached -40%). Viceversa, 24/16 motor shows a ripple extremely high, so that this machine becomes unacceptable for any real application.

For these reasons, this 24/16 motor is the configuration which will be examined in depth into this thesis, and it will be called, hereafter, **Reference motor**: the aim of the work is to act on the machine geometry in order to reduce the torque ripple as much as possible, without modifying the average torque value (or, better, increasing it).

In Figs. 2.10 - 2.13 and Tab. 2.5: a section of the motor, a scheme of the winding, the geometrical data, the research of $\alpha_{ie,opt}$ and the torque behaviour:
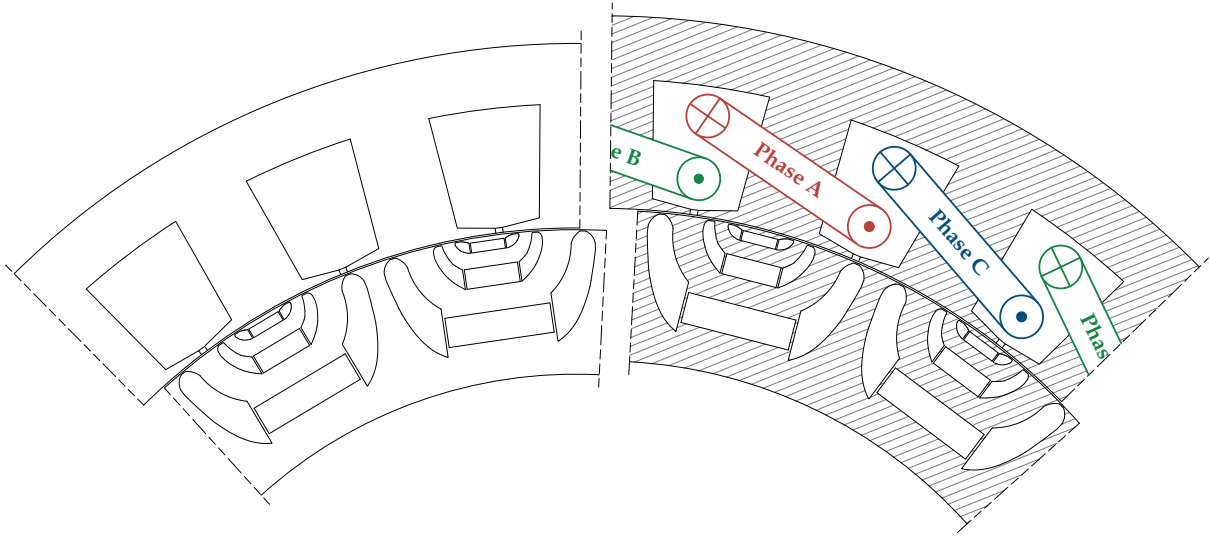
Figure 2.10: 24/16 Cross Section

Figure 2.11: 24/16 Winding

Stator		
D_e	650	mm
D_i	500	mm
Q_s	**24**	$[-]$
S_{slot}	**1866**	mm^2
w_t	**33**	mm
w_{so}	3	mm
h_s	50	mm
h_{bi}	25	mm
Rotor		
D_r	498.6	mm
D_f	200	mm
b	3	$[-]$
Other		
$2p$	16	$[-]$
L_{stk}	235	mm
g	0.7	mm
m	3	$[-]$
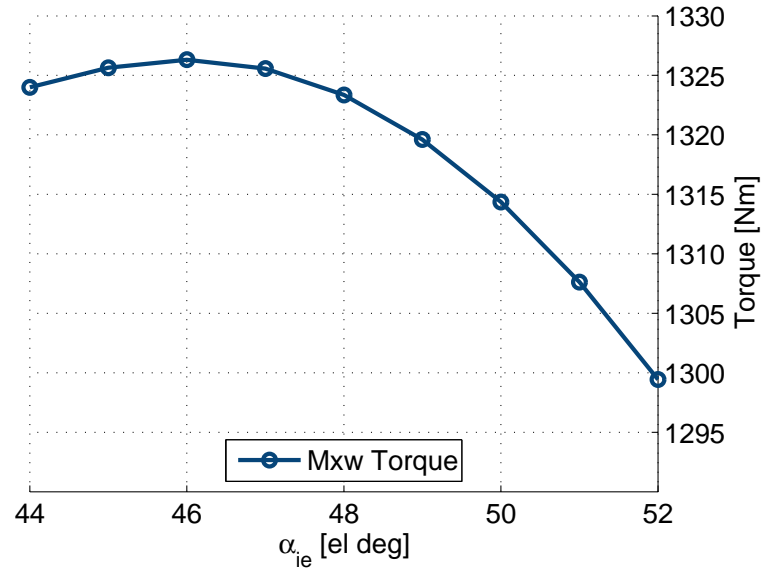
Table 2.5: 24/16 data

Figure 2.12: MTPA working point research

The research of MTPA working point fixes the phase of current vector to the value: $\alpha_{ie,opt} = 46\ ^{el\ deg}$. Its amplitude, instead, is calculated with the same rules seen before:

$$|\bar{I}|_{24/16} = |\bar{I}|_{72/16} \cdot \frac{Q_{S,\ 72/16}}{Q_{S,\ 24/16}} \cdot \frac{k_{w,\ 72/16}}{k_{w,\ 24/16}} = 1200 \cdot \frac{72}{24} \cdot \frac{0.945214}{0.866025} \approx 3930A$$
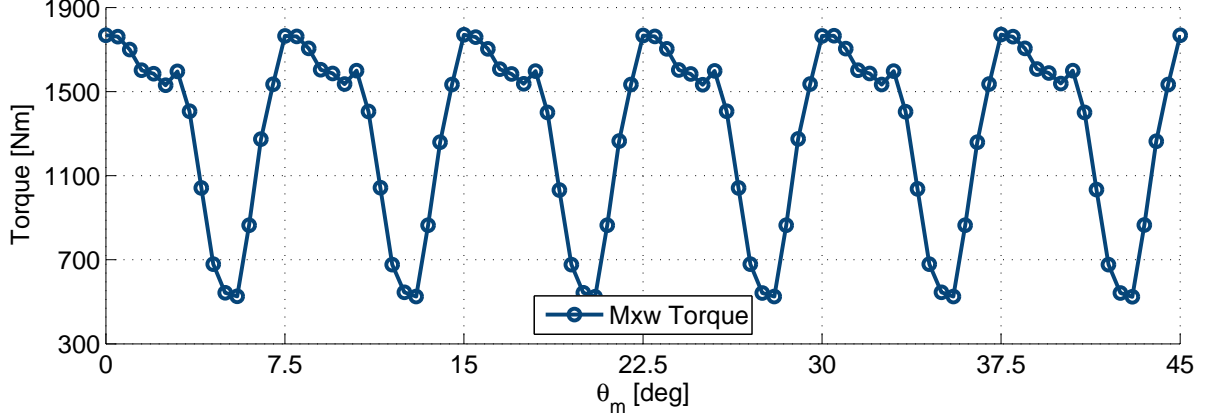
Figure 2.13: 24/16 torque ripple at $\alpha_{ie} = 46$ $^{el\ deg}$

From Fig. 2.13, the torque behaviour is very different from the previous ones: the average torque remains rather high ($T_{avg} \approx 1306Nm$), while ripple increases a lot: from values around $T_{ripple} \approx 15\%$ to $T_{ripple} = 97.36\%$.

This reference motor peculiarity encourages to additional deeper studies and, so, for an analysis of the just presented results, see next chapter.

2.3   Conclusions

In this chapter, a summary of what has been done at the beginning is present. Some fractional-slot PMASynRel motors have been analysed with different configurations of Slots/Poles: 18/16, 21/16, 24/16. All these motors have the same main geometrical data, for a better comparison between them and with the first designed motor, which is called **Motor #1**.

The passage from distributed winding to concentrated one leads to a collective decrease of average torque and to an increase of torque ripple. In Tab. 2.6 a summary of the obtained results is reported:

		Motor #1			Reference
Q_s	[-]	72	18	21	24
$2p$	[-]	16	16	16	16
$\bar{I}$	A_{peak}	1200	4800	4370	3930
α_{ie}	[el deg]	58	40	39	46
T_{avg}	[Nm]	1696	1049	1093	1306
	[%]	100	61.85	64.15	77.01
T_{ripple}	[%]	18.45	22.37	12.40	97.36

Table 2.6: Comparison between the motors

Particularly interesting is the solution PMASynRel 24/16: with respect to the other two configurations, it exhibits opposite characteristics, both in terms of average torque (rather high) and ripple (extremely high). This is the reason why the aim of this work, hereafter, will be focused

23

only on this last motor. For convenience, it will be called **Reference Motor**. The purposes, now, are twofold:

1. to look for an explanation on why the machine has got a so strange behaviour, respect to the other ones;

2. to try some advanced design strategies in order to improve the machine performance.

This thesis is organized as follow:

CHAPTER 3. An introduction on the 24/16 PMASynRel is presented. In particular some magnetic considerations are present. In addition, a numerical tool, which will be fundamental for deeper analyses, is explained.

CHAPTERS 4-5. Three different design strategies are reported. They act on the stator and are called *Slot Deformation*, *Tooth Cut* and *Stator Shifting*, respectively.

CHAPTER 6. A multi-objective evolutionary optimization algorithm is used to define the best shape for the rotors barriers, in terms of increase of average torque and reduction of ripple, at the same time. The algorithm was developed by *Alotto et al.* [4], and it has been adapted for this work.

CHAPTER 7. The well-known skewing technique is here exhibited and a new algorithm is developed to study the best combination of rotor skewed parts. The chapter, together with the previous one, defines the design strategies which act on the rotor.

CHAPTER 8. Deeper studies is finally conducted on the motor. In particular, from what has been discovered during the previous chapters, the machine analytical model is reconstructed and the main cause of the high ripple is found.

Chapter 3

The 24/16 Reference motor

3.1 Magnetic behaviour

Let's consider the 24/16 motor, fed by a current of magnitude $|\hat{I}| = 3930A$ and with a phase angle of $\alpha_i^e = 46$ $^{el\ deg}$. Fig. 3.1 shows the Maxwell torque behaviour for a rotation of 360 $^{el\ deg}$:
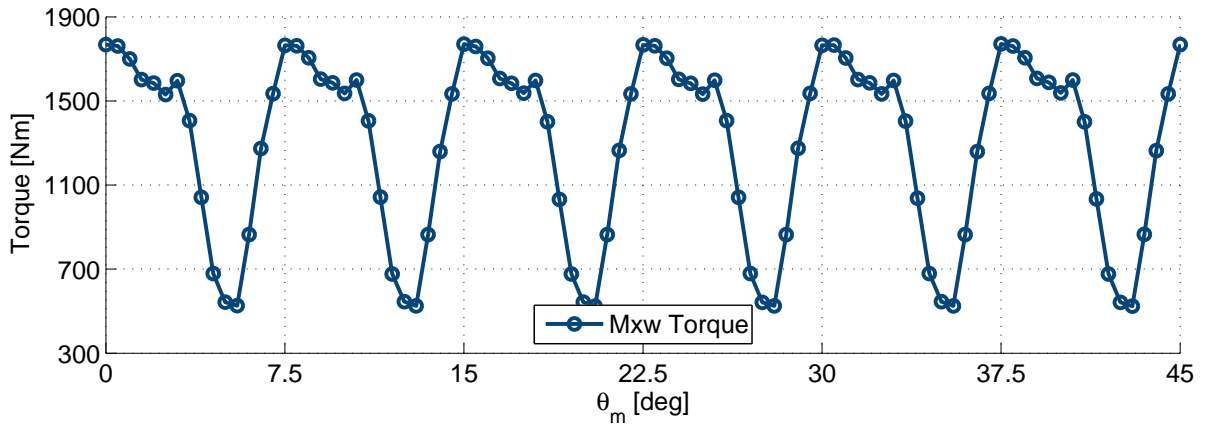

Figure 3.1: Maxwell Torque Ripple for PMASynRel 24/16 configuration

Figure shows that the torque remains high most of the time, while holes appear every 7.5 ^{deg} = 60 $^{el\ deg}$, in particular at $\theta_m = 5$ ^{deg}, $\theta_m = 12.5$ ^{deg}, $\theta_m = 20$ ^{deg}, and so on. In other words: the motor is characterized by an important contribution of the $6 - th$ torque harmonic.

From a magnetic point of view, the motor has a periodicity $t = 8$. It means that the magnetic behaviour of the machine can be studied only for a portion of 3 slots and 2 poles, because it repeats itself in the same way in the remaining part. Hereafter, hence, only a two-pole pitch (2-PP) is considered.

If we now consider a geometrical configuration, both when torque is high (e.g. at $\theta_m = 1.5$ ^{deg}, called *Good position* Ⓖ) and when it is low (e.g. at $\theta_m = 5$ ^{deg}, called *Bad position* Ⓑ), two different magnetic situations will be worth noting:

- when $\theta_m = 1.5$ ^{deg} (good condition Ⓖ), two different magnetic circuits are recognizable over the two-pole pitch. The first one, on the right of Fig. 3.2(a), links two neighbouring slots and it is associated to an equivalent negative current: $I_- = -2886 - 119 = -3005A$. The second one, on the left of the same figure, sorrounds only one slot, where a positive

current $I_+ = 3005A$ is present. In Fig. 3.2(a), the two different magnetic circuits are highlighted in thin red and thick green, respectively.

In this situation, the pole associated with the shorter magnetic circuits (the thick one, on the left), develops an high torque value of $T' \approx 143.4Nm$ each, while the other (associated with the longer magnetic circuits on the right), develops a lower but with the same direction torque of $T'' \approx 55.3Nm$. Consequently, the torque, T_{2-PP}, developed over a two-pole pitch is:

$$T_{2-PP}(\theta_m = 1.5 \ ^{deg}) = T' + T'' \approx 143.4 + 55.3 \approx 198.7Nm$$

NOTE: To derive the torque values just reported, the Maxwell Stess Tensor method has been used. In particular, with FEMM$^\circledR$ software, an arc covering each magnetic circuit has been defined and, then, the line integral has been used to calculate the torque from Maxwell Stress Tensor.
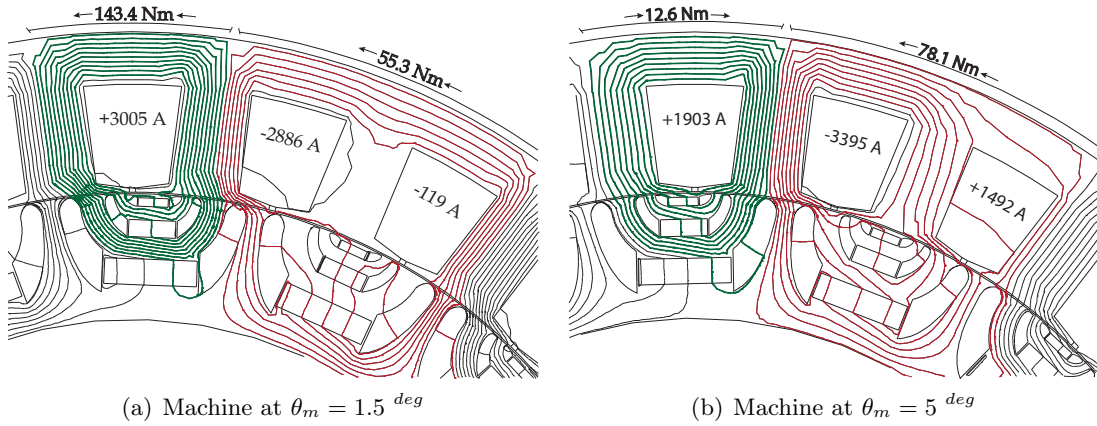

(a) Machine at $\theta_m = 1.5 \ ^{deg}$ (b) Machine at $\theta_m = 5 \ ^{deg}$

Figure 3.2: Magnetic circuits

- when $\theta_m = 5 \ ^{deg}$ (bad condition Ⓑ), the two different magnetic circuits are still recognizable and they involve the same slots as the previous position. Unfortunately, as illustrated in Fig. 3.2(b), the flux lines change and, in particular, they change in a negative way. The shorter magnetic circuit (the thick green one) presents an opposite misalignment respect to the previous situation, as highlighted in Fig. 3.3:

(a) Machine at $\theta_m = 1.5 \ ^{deg}$ (b) Machine at $\theta_m = 5 \ ^{deg}$
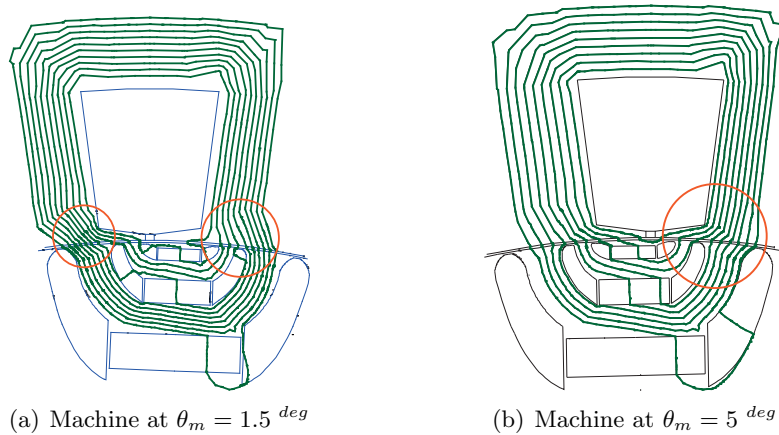
Figure 3.3: Misalignment of the short magnetic circuit

In Fig. 3.3(b), some flux lines tend to reduce the reluctance of the magnetic circuit, by aligning the pole with the slot. Thus, the overall magnetic force which arises will push the rotor from left to right and the contribution -in terms of torque- will be a negative value. In other words: the torque associated to the thick green circuit will get the rotor to rotate clockwise, rather than anticlockwise.

Furthermore, the other magnetic circuit (the thin red one) doesn't balance out this negative torque, adequately. The reason is clear if we consider the Hopkinson's Law:

$$N \cdot i = \oint_{\partial S} H \cdot dl \approx \phi_B \cdot \oint_{\partial S} \frac{dl}{\mu S} = \Re_H \cdot \phi_B \tag{3.1}$$

where: $N \cdot i$ is the *Magnetomotive Force*, $\Re_H$ is the *Magnetic Reluctance* of the circuit, and ϕ_B is the *Magnetic Flux*.

Due to the excessive alignment between the pole and the tooth, the overall reluctance of the circuit increases, because the length of the latter, ∂S, is greater. If this is not enough, a part of the flux lines links two neighbouring slots with opposite currents: the direct consequence is that also the Magnetomotive Force, $N \cdot i$ will decrease. All these peculiarities get the flux, ϕ_B, to be lower and -thus- the magnetic force, too.

The torque developed over a two-pole pitch is now:

$$T_{2-PP}(\theta_m = 5 \ ^{deg}) = T' + T'' \approx 78.1 - 12.6 \approx 65.5 Nm$$

3.2   Poles pursuit

Until now, only two significant rotor positions has been considered ($\theta_m = 1.5 \ ^{deg}$ and $\theta_m = 5 \ ^{deg}$). This section has, instead, the purpose to understand how the motor magnetically behaves, in a rotation equal to an entire electric period ($\theta_m = 45 \ ^{deg}$). The torque developed by each magnetic circuit should be considered as the rotor position changes. This operation, however, is long and difficult to realize, because we don't know -a priori- how the magnetic circuits are made. Anyway:

- The machine has an high periodicity. Therefore it is not necessary to consider the whole machine: considering the magnetic circuit relative only on one periodicity is enough;

- Fig. 3.2 shows that the magnetic circuits develop themselves over each pole. Therefore, a good approximation consists on taking into account the pole, rather than the single magnetic circuit.

In other words: following, the two poles which define a single periodicity of the machine will be observed. As the rotor position changes, the torque contribution due to each pole will be derived in the same way explained above. Finally, the behaviour of this "pole pursuit" will be graphed.

In Fig. 3.4 the torque contributions (T_{PP}) due to the two poles into a periodicity are reported. Each pole, during its rotation, alternates resting times, where the pole can be considered "unloaded", and peak times, where it actively contributes in torque development. This behaviour is identical for the two poles. The result consists on two curves equally spaced ($\Delta\theta_m = 7.5 \ ^{deg}$), as in figure:
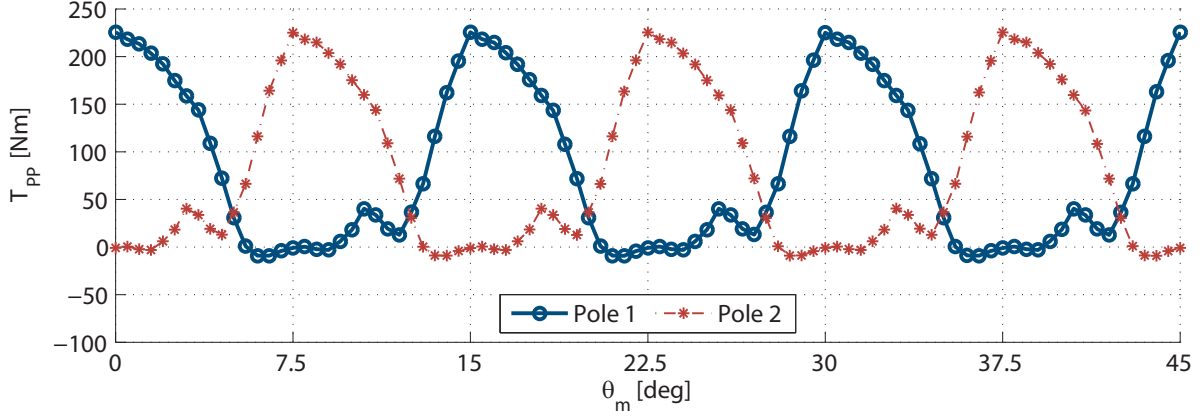
Figure 3.4: Pole pursuit in a single periodicity of Reference motor

The torque drops arise at the mechanical angles: $\theta_m = 5 + (7.5) \cdot k \ ^{deg}$, where $k \in \mathbb{N}$. The figure above shows that these angles correspond to that ones where a change from the Pole 1 (the thick blue line with point markers) to Pole 2 (the thin curve with star markers) occurs. In particular, referring to Fig. 3.4:

- There are 6 transitions between the two curves. This is the reason of a $6 - th$ harmonic of torque;

- The rising and falling edges are rather sharp. Then, the intersections between the two behaviours occur when:

  - the falling edge of the first curve has already reached low values of torque;
  - the rising edge of the second curve has just begin to increase (has yet to reach high values).

  This is the reason why the torque drops are so deep.

3.2.1 Generalization

From what has just been said, two general rules can be derived. Let's consider a generic fractional slots (FS) SynRel motor with X slots and Y poles. Called t the periodicity of the machine, it is possible to observe the latter only into a single portion (associated to one periodicity) in order to understand the magnetic behaviour of the whole motor. This portion is characterized by N_X slots-per-periodicity and N_Y poles-per-periodicity.

Then, there will be N_Y equispaced curves. By assuming that the shape of these curves remains rather similar for any configuration X/Y, then, the less N_Y is, the greater the torque drops will be deep:

Prop 1. *Let's consider a generic FS SynRel machine with p pole-pairs and periodicity t. Then, the less the ratio $N_Y = 2p/t$ is, the greater is the torque ripple of the machine.*

Secondly, it is possible to know -a priori- the torque harmonic value due to the presence of the phenomena just explained.
The torque drop occurs when a pole has to "hook" the following tooth: the "magnetic jump" from a tooth to an another one is the passage from a curve to the next one (by referring to the figure above). Therefore, the number of torque drops will be equal to the poles-per-periodicity

multiplied by the number of "magnetic jumps" (i.e. the number of slots-per-pole) that each pole must carry out.

Definitively:

Prop 2. *Let's consider a generic FS SynRel machine with Q_s stator slots, p pole-pairs and a periodicity of t. Then, it will certainly show a torque harmonic order, ν, defined as:*

$$\nu = N_X \cdot N_Y = \frac{Q_s}{\not{p}} \cdot \frac{2\not{p}}{t} = \frac{2Q_s}{t} \tag{3.2}$$

The correctness of these generalization has been verified on different motor configurations. In particular, the following machines[1] has been taken into account:

Q_s	[$-$]	9	12	12	15	18	21	24
$2p$	[$-$]	8	8	10	10	16	16	16
t	[$-$]	1	4	2	5	2	1	8
$N_Y = 2p/t$	[$-$]	8	2	5	2	8	16	2
T_{Ripple}	[%]	16.29	59.02	23.73	63.48	22.37	12.40	97.36
$\nu = 2Q_s/t$	[$-$]	18	6	12	6	18	42	6
Presence of T_ν?	[y/n]	YES	YES	YES	YES	YES	YES	YES

Table 3.1: Validation of the generalization

3.3 Fields contribution to torque development

The study doesn't stop only to the analysis of the field maps and, in general, on graphical qualitative evaluations: the machine has been studied also through an harmonic analysis of the magnetic forces which characterize the motor.
Spargo et al. [6] presented a seminumerical approach that, from data which are directly recoverable from a common FE software, allows to associate to each spacial harmonic of flux density at the air-gap, the relative torque contribution produced by that harmonic.

From the FE analysis at the desired operating points, θ_m, it's possible to extract the flux density air-gap field, defined by an arc in the center of the air gap. As the air gap is small, the assumption is made that the variation in the radial dimension is negligible. The achieved air-gap (radial and tangential) flux densities, B_n and B_t, are not continuous functions: they are discretized in a number of points specified by the user (2048 points have been taken into account).

Defined $\xi = nT$, the descrete angular coordinate along the air-gap, the flux density, $B(\xi, \theta_m)$, can be decomposed using a discrete Fourier series:

$$B_\upsilon(\theta_m) = \frac{1}{N} \cdot \sum_{n=0}^{N-1} B(\xi, \theta_m) \cdot e^{-i\upsilon n \frac{2\pi}{N}} \tag{3.3}$$

where: υ is a generic harmonic order, N is the sampling rate ($N = 2048$), T is the sampling interval ($T = \frac{2\pi}{N}$) and i the imaginary unit.

---

[1]These motors has been all simulated. A part of them directly into this thesis. The others have been analysed by *Marzarotto* in [5]

The Maxwell stress tensor, expressed in cylindrical coordinates and neglecting any z-axis component field, defines a resultant shear rotor stress, written as:

$$\sigma(\xi, \theta_m) = \frac{B_n(\xi, \theta_m) \cdot B_t(\xi, \theta_m)}{\mu_0} \tag{3.4}$$

By considering that torque is derived simply by a double integration of $\sigma(\xi, \theta_m)$ over ξ and z-axis, and remembering the radial and tangential fields can be harmonically decomposed and reassembled as a sum of cosinusoidal functions (according to the inverse discrete Fourier transform), the harmonic torque components, T_v, at a specific position of the rotor, θ_m, can be written as:

$$T_v(\theta_m) = \frac{4\pi l_{stk} r^2}{\mu_0} \cdot |B_{n,v}(\theta_m)| \cdot |B_{t,v}(\theta_m)| \cdot cos(\alpha_v) \tag{3.5}$$

where: l_{stk} is the stack length of the rotor, r is the radius of the machine (at the air-gap) and α_v is the phase angle between the $v - th$ harmonic of the radial and tangential fields.

Repeating the computation for each θ_m, Fig. 3.5 is drawn:
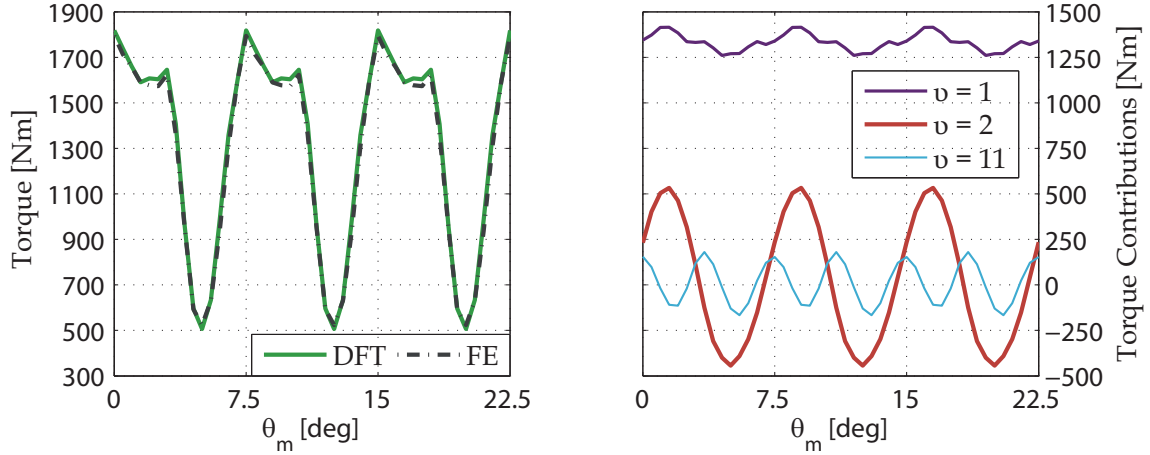

Figure 3.5: Harmonic Analysis of simmetrical PMARel 24/16

The graph on the left is a comparison between the torque behaviour of the machine, computed both through the FE software and the seminumerical approach just presented.
The second graph (on the right) is the output of the algorithm. The medium violet line (on the top) is the torque contribution due to the synchronous flux density field. Obviously, the main characteristic of this field is the presence of a constant torque, also if a low ripple is however visible. With a thick red line the main contribution to the torque ripple is highlighted: it is due to the presence of a second harmonic of flux density, which produces a $6 - th$ harmonic of torque. Finally, with a thin and cyan line a second important ripple contribution is due to the presence of a $11 - th$ field harmonic, which produces a $12 - th$ torque harmonic.

This approach is a valid tool which will be used during this thesis to verify if some design strategies are able to reduce specifically the second and/or eleventh order field contributions. In addition, results just obtained will be useful to reconstruct the motor analytical model, reported in Chap. 8.

Chapter 4

Slot Deformation and Tooth Cut

Sect. 3.1 highlighted how the reference PMASynRel motor exhibits a problem in some particular rotor positions. This fact has been explained graphically and, by referring -in particular- to Fig. 3.2, an abnormal behaviour of flux lines is noted for one of the two magnetic circuits over a two-pole pitch. Flux lines, in fact, do not follow an advantageous way for the torque development (advantageous in an anti-clockwise rotation direction), and it implies a drop in the torque behaviour. A first idea, then, is to act on the stator geometry through little variations, with the aim to force flux lines to change their trajectory.

This chapter is composed of a first and rapid summary on the Reluctance principle. Then, two ideas are presented: they are called, respectively, **Slot Deformation** and **Tooth Cut**.

4.1 Skills: Reluctance Torque

The first problem which arises is to understand what does "right" or "wrong" way means. In other words: it is written that flux lines, at particular rotor positions, follow wrong trajectories. What does it means? Why these ways are wrong? What should be the correct paths?
An answer to these questions, actually, has already given in Sect. 3.1. Here, a more analytical and exhaustive explanation is reported.

Let's consider a simple two-pole electro-mechanical converter with saliencies both on rotor and stator. θ is the angle between the rotor axis and the stator one: it identifies the misalignment degree between the rotor tooth and the stator pole. A current, i, flows through the stator winding.

The winding is characterized by a coefficient of self-induction, $l(\theta)$: assuming the magnetic circuit is linear, and considering only the fundamental component of the field distribution, produced by the winding at the gap, it is:

$$l(\theta) = L_1 + L_2 \cdot cos(2\theta) \tag{4.1}$$

where L_1 and L_2 are well-defined coefficients. Therefore:

1- inductance reaches its maximum value (the minimum value of reluctance, $\Re_H$) when the two axes are aligned, that is when $\theta = 0 \ ^{deg}$. It corresponds to "straight" flux lines, as reported in Fig. 4.1(a);

2- inductance decreases (reluctance increases) with the increment of the misalignment between the two axes, that is when $\theta \neq 0 \ ^{deg}$. It corresponds to "crooked" flux lines, as reported in Fig. 4.1(b).

(a) Machine at $\theta = 0$ ^{deg} (b) Machine at $\theta = 10$ ^{deg}
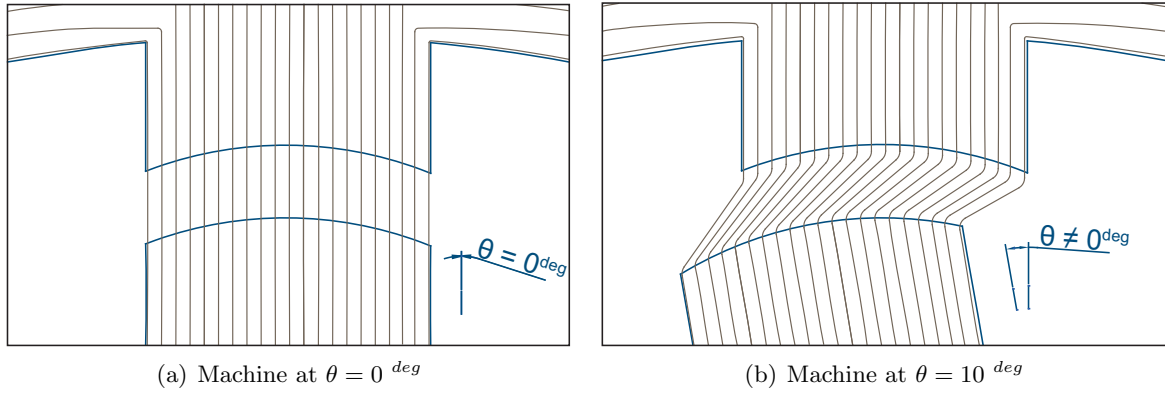
Figure 4.1: Flux lines of a reluctance magnetic circuit

The **reluctance torque** can be defined as:

$$T(\theta, i) = \left| \frac{\partial W_{ec}(\theta, i)}{\partial \theta} \right|_{i=const} \tag{4.2}$$

where $\partial W_{ec}(\theta, i)$ is the converted energy from electrical to mechanical type. Under linearity conditions, it is:

$$W_{ec}(\theta, i) = \frac{1}{2} \cdot l(\theta) i^2 \tag{4.3}$$

Therefore:

$$T(\theta, i) = \frac{1}{2} \cdot \frac{\partial l(\theta)}{\partial \theta} i^2 = -L_2 i^2 sin(2\theta) \tag{4.4}$$

T is called "Reluctance Torque" because it is linked to the presence of different values of reluctance, $\Re_H$, with the change of rotor position, θ: this torque, hence, will arise with the aim to get the rotor to its natural low-reluctance position, $\theta = 0$ ^{deg}.

4.2 Slot Deformation

The first idea is called **Slot Deformation** and consists on:

- a local change of stator slots shape, where the developed torque exhibits the opposite direction of the average torque, that is where flux lines have an opposite direction with respect to the machine's rotation wise, $\theta < 0$. The aim is to look for decreasing the torque local contribution, by relaxing the "crooked" lines and -therefore- by getting them straighter.

- a local change of stator slots shape, where flux lines already have the same direction with respect to rotation wise (developed torque with the same sign of average torque). Here, an additional increment of pole-tooth misalignment is implemented and an increase of the reluctance of the magnetic circuit (and of the developed torque, too) is expected.

In Tab. 4.1 the implemented deformations are reported. They consist on vertical and/or horizontal translations of the lower slot corners. Every cell indicates the new corner coordinates (the unit of measurement is: *millimeters*), with respect to the original position:

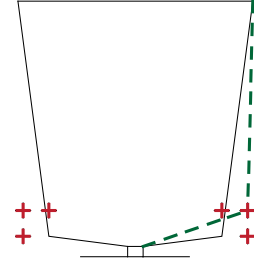|	South-Western Corner			
	0;0	0;5	-5;0	-5;5
South-Eastern Corner — 0;0	—	(0;0)(0;5)	(0;0)(-5;0)	(0;0)(-5;5)
0;5	(0;5)(0;0)	(0;5)(0;5)	(0;5)(-5;0)	(0;5)(-5;5)
5;0	(5;0)(0;0)	(5;0)(0;5)	(5;0)(-5;0)	(5;0)(-5;5)
5;5	(5;5)(0;0)	(5;5)(0;5)	(5;5)(-5;0)	(5;5)(-5;5)

Figure 4.2:

Table 4.1: Implemented deformations

Example 4.2.1. In a 2D Cartesian plane, for instance, a slot is defined by four corners, **A**, **B**, **C**, **D**, with coordinates:

$$A\ (-17; 250) \qquad B\ (-23; 300) \qquad C\ (23; 300) \qquad D\ (17; 250)$$

Let's consider the combination: (0;5)(-10;2). The first parenthesis refers to the South-Eastern corner (point **D**), while the second one refers to point **A** (South-Western corner).
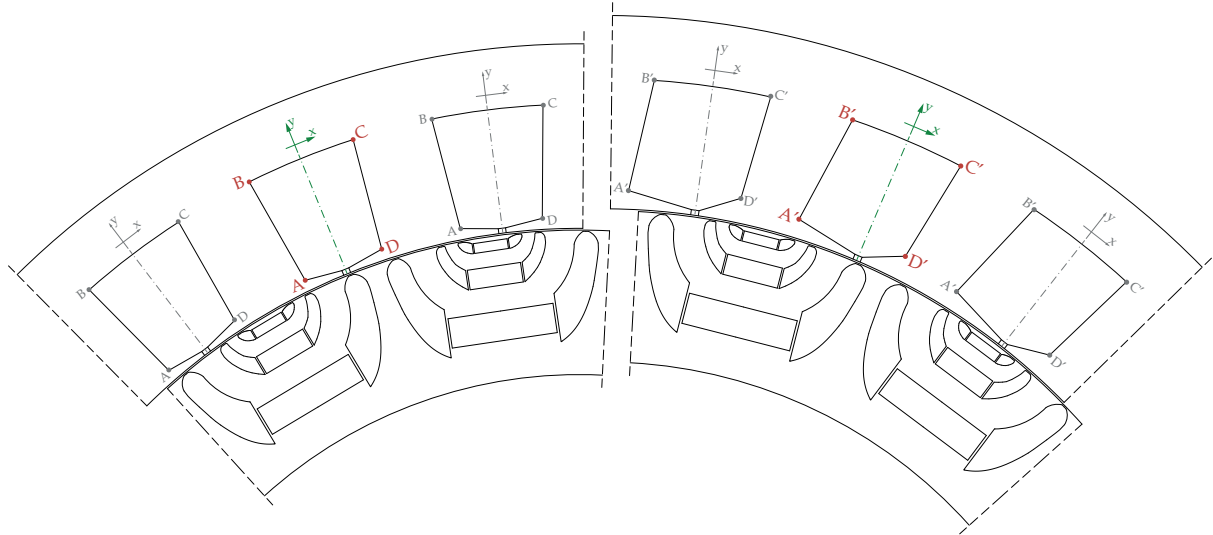
If now Slot Deformation is applied, four new corners are obtained: the outer ones maintain the same previous position, **B' ≡ B** and **C' ≡ C**, while the inner ones are made up by summing their previous coordinates with the values expressed by the combination:

$$A'\ (-17 - 10; 250 + 2) \qquad B'\ (-23; 300) \qquad C'\ (23; 300) \qquad D'\ (17; 250 + 5)$$
$$A'\ (-27; 252) \qquad\qquad B'\ (-23; 300) \qquad C'\ (23; 300) \qquad D'\ (17; 255)$$

4.3 Slot Deformation - Results

Following, some simulations results are presented. Generally, the idea of Slot Deformation leads to no improvements of machine performance. On the contrary, the average torque decreases almost always, while ripple remains high.

Nevertheless, anyway, some configurations show a positive, even if poor, result. These are: $(0;5)(0;0)$, $(0;0)(-5;0)$ and $(0;5)(-5;0)$.

NOTE 1. In order not to make heavier this reading, only these first three combinations are shown, while the others are reported in Appendix A.

NOTE 2. For these simulations, only the first $\theta_m = 180$ $^{el\ deg} = 22.5$ ^{deg} are simulated.

4.3.1 Sequence (0;5)(0;0)

First sequence analysed is the $(0;5)(0;0)$ one. In Fig. 4.3 torque behaviour of distorted machine (the dashed blue line) is compared with that one of the reference motor (the continuous orange line), while in Fig. 4.4 the same torque trend is split into three components, each of which associated to the specific $\upsilon - th$ spatial harmonic of flux density at the air-gap. Finally, in Fig. 4.5 the harmonic analysis of torque behaviour is made in order to understand what are the harmonics which characterize the first graph.
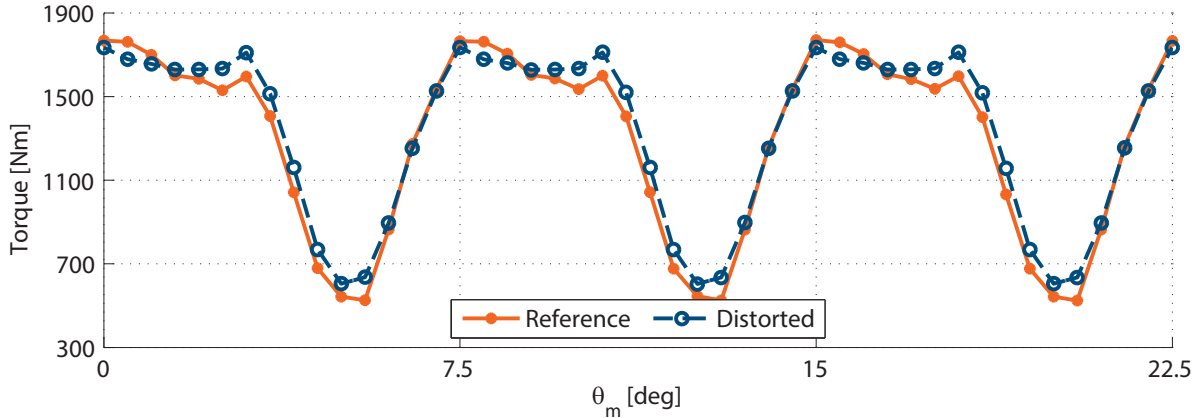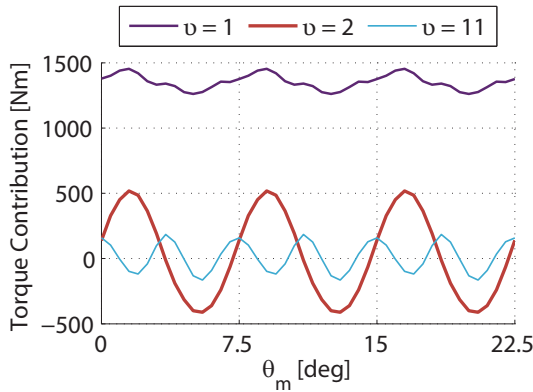

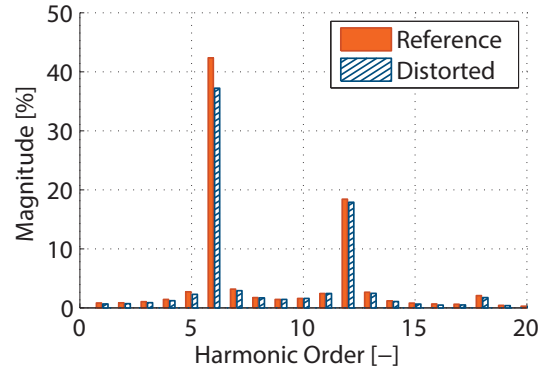Figure 4.3: (0;5)(0;0) torque ripple

Figure 4.4: Torque contributions

Figure 4.5: (0;5)(0;0) torque harmonics

34

As it can be seen above, with this Slot Deformation, a minimal change in the analysed quantities is obtained:

$$T_{avg} = 1345Nm \qquad\qquad T_{ripple} = 84.14\%$$

Referring to Fig. 4.3, the torque behaviour is more flattened in the higher portion and the torque drop, also if still present, is slightly less deep. This change can be observed from the torque harmonic content of Fig. 4.5, too: this sequence acts particularly on the $6-th$ harmonic, which decreases from 42.4% to 37.2% of the average torque value. This reduction is also noted in the others harmonic orders, but in a more limited way.

Finally, there are no particular observations on Fig. 4.4: torque ripple, as in the reference motor, is still due to the presence of a $2-th$ spacial harmonic of flux density at the air-gap, which seems not to be influenced by this action.

4.3.2   Sequence (0;0)(-5;0)

The same graphs have been derived also for the second sequence: (0;0)(-5;0), where only the south-western corner has been shifted.
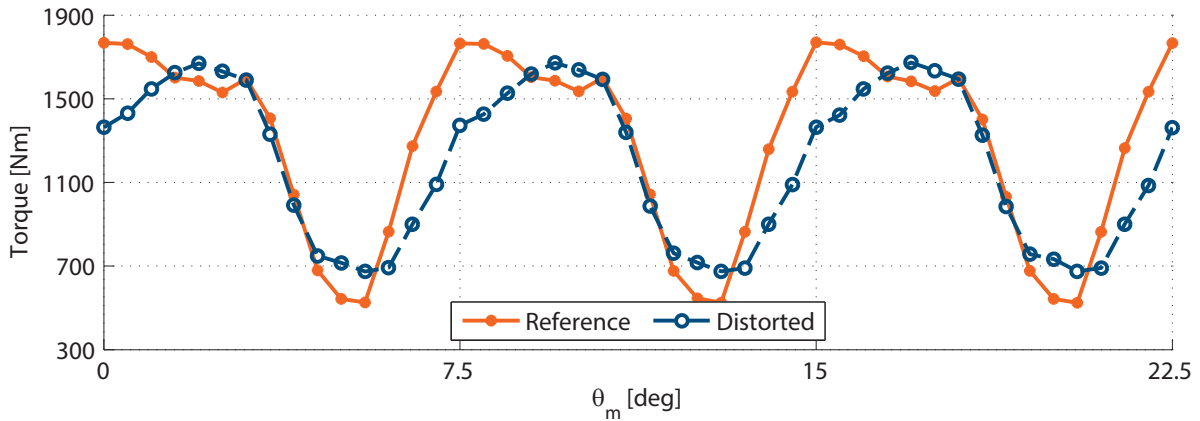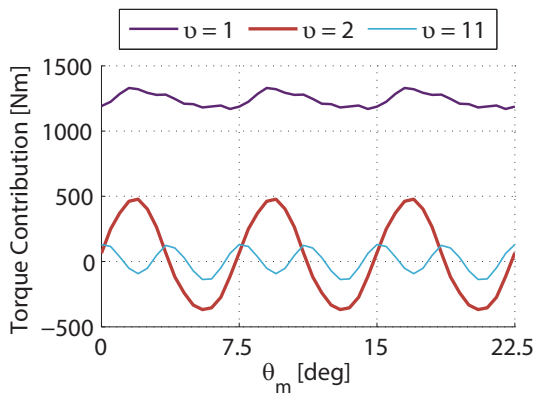

Figure 4.6: (0;0)(-5;0) torque ripple
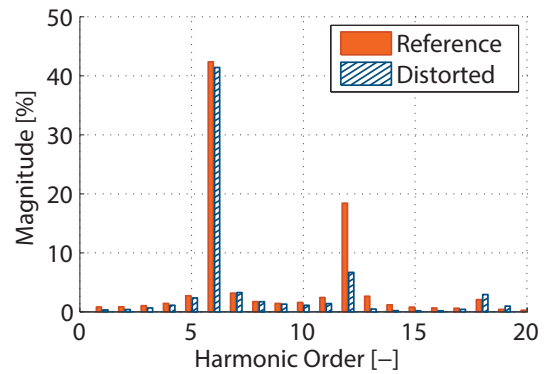

Figure 4.7: Torque contributions

Figure 4.8: (0;0)(-5;0) torque harmonics

In Fig. 4.6 it is possible to note how this particular distortion influences the shape of the torque behaviour and, in particular, how torque ripple assumes a more sinusoidal geometry with respect to the reference motor. It leads to think that, in this case, is not reduced as much the $6 - th$ harmonic of torque, but rather an another higher one. This thinking is verified immediately, if Fig. 4.8 is observed: with the deformation of SW corner the affected harmonic is, now, the $12 - th$ (from 18.42% to 6.68% of the average value), and no more the $6 - th$. Definitive values are:

$$T_{avg} = 1204Nm \qquad\qquad T_{ripple} = 83.03\%$$

4.3.3   Sequence (0;5)(-5;0)

As someone could expect, union of the two previous solutions leads to an halfway effect, both in terms of average torque and ripple. With sequence (0;5)(-5,0), in fact, both the $6 - th$ and the $12 - th$ torque harmonics decrease simultaneously: from 42.4% to 37.2% for the first one, from 18.42% to 7.64% for the second one.
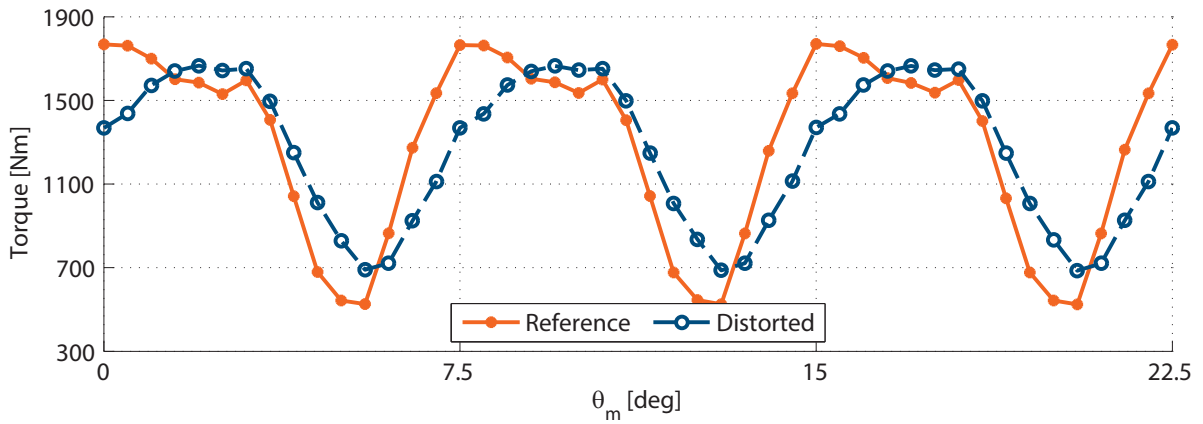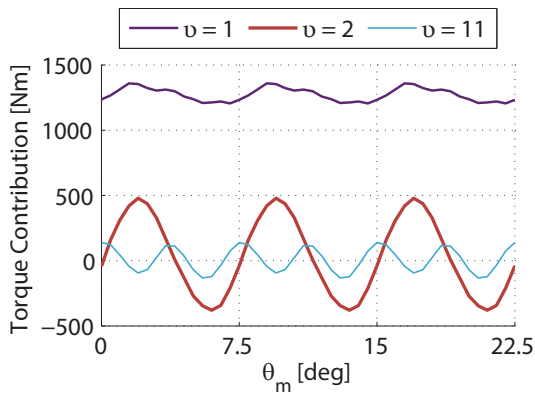

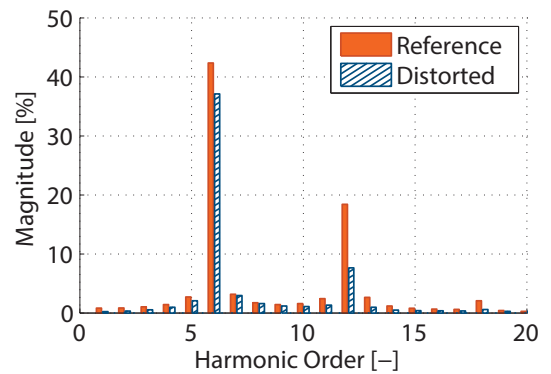Figure 4.9: (0;5)(-5;0) torque ripple

Figure 4.10: Torque contributions

Figure 4.11: (0;5)(-5;0) torque harmonics

Conclusion, in this case, is

$$T_{avg} = 1269Nm \qquad\qquad T_{ripple} = 77.31\%$$

4.3.4 Comparison and comments

In Tab. 4.2 the obtained results are reported, for all the executed simulations, both those ones illustrated above and those ones in the appendix:

		*ref.							
SE Corner		(0;0)	(0;5)	(5;0)	(5;5)	(0;0)	(0;0)	(0;0)	(0;5)
SW Corner		(0;0)	(0;0)	(0;0)	(0;0)	(0;5)	(-5;0)	(-5;5)	(0;5)
Minimum	Nm	523	604	416	495	594	674	455	663
Maximum	Nm	1795	1735	1810	1714	2049	1674	1747	1997
Average Torque	Nm	1306	1345	1208	1251	1287	1204	1191	1293
	%	100	102.99	92.50	95.79	98.55	92.19	91.20	99.01
Ripple	%	97.36	84.14	115.42	97.40	113.04	83.03	108.45	103.26

SE Corner		(0;5)	(0;5)	(5;0)	(5;0)	(5;0)	(5;5)	(5;5)	(5;5)
SW Corner		(-5;0)	(-5;5)	(0;5)	(-5;0)	(-5;5)	(0;5)	(-5;0)	(-5;5)
Minimum	Nm	686	572	559	472	392	555	585	382
Maximum	Nm	1666	1689	2043	1578	1699	1999	1564	1624
Average Torque	Nm	1269	1219	1207	1066	1308	1202	1101	1042
	%	97.17	93.34	92.42	81.62	100.15	92.04	84.30	79.79
Ripple	%	77.31	91.61	122.98	103.82	125.94	120.11	88.89	119.27

Table 4.2: Slot Deformation - Comparison of results

Now two observations are worth of noting:

1. The first one refers to a big limit of Slot Deformation, in particular when the distortion is not equal between the two inner corners (SE and SW). When it occurs, in fact, the machine is no longer symmetrical and -thus- the obtained results can be considered valid only for the particular rotation wise hypothesized in simulations.
   In order to rotate the rotor in clock-wise direction (the contrary of what has been supposed until now), it is necessary to invert the phases sequence. But it would imply a different magnetic situation and, probably, the result presented above would not be obtained;

2. The second comment consists on the attempt of understanding what happens into the machine with Slot Deformation and why the improvements are so limited.
   What is sure is that, through Slot Deformation, the way flux lines follow, changes. The problem, now, is to understand why it occurs. Only two possible explanations are given:

   - Either Slot Deformation extends the slot area over the previous flux lines trajectory. Therefore, flux is forced to change its path because there is no more iron, as before. In other words: where before there was iron, now there is the slot;

   - or, Slot Deformation could cause the saturation of some zones and a de-saturation of other ones. In this way, the flux lines deviation is not due to physical barriers, but rather it is present because saturation leads flux lines to prefer other trajectories, respect the original ones.

This latter hypothesis is particularly easy to verify and, as it will be seen, it is exactly what happens. To evaluate if stator saturation is, actually, the reason of the obtained result, all the viewed motors have been re-simulated, by changing the material, from Terni to a simple linear iron: an hypothetical material, with a linear B-H curve and relative permeabilities, $\mu_x = 10000$ and $\mu_y = 10000$, has been used.

Fig. 4.12 reports the comparisons between reference motor and the machines with distorted teeth, illustrated above. The comparison has been carried out over a rotation of $\theta_m = 7.5$ ^{deg} and with a current angle of $\alpha_{ie} = 46$ $^{el\ deg}$, that is equal to the reference motor's $\alpha_{ie,opt}$.

(a) Sequence (0;5)(0;0)
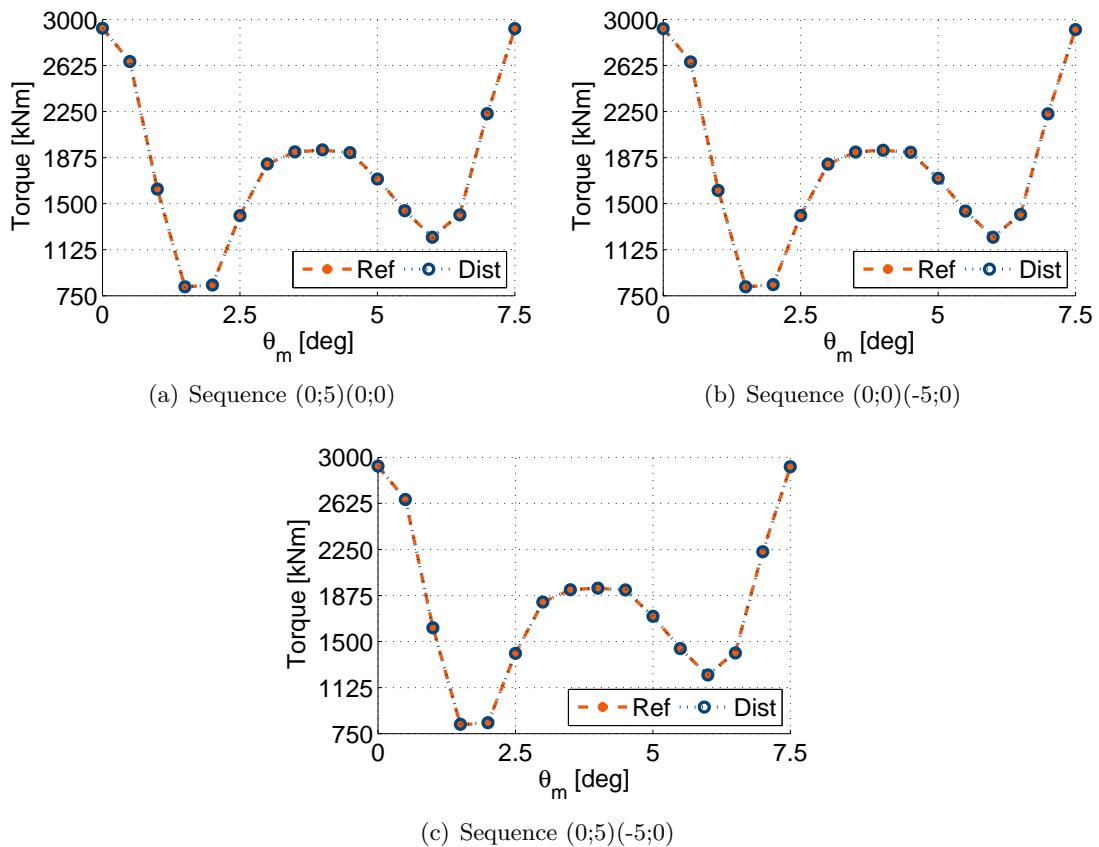
(b) Sequence (0;0)(-5;0)

(c) Sequence (0;5)(-5;0)

Figure 4.12: Slot Deformations with linear iron

As clear as in all the figures, when stator works in linearity conditions, distorted motors show the same torque trend of the reference motor's one. This proves that Slot Deformation acts on stator iron saturation: some areas, by saturating themselves more than others, thanks to the slot warp, become a sort of "magnetic obstacle" for the flux density field, whose fluxlines will tend to follow different trajectories, as a consequence. In the previous illustrated cases, these new trajectories operate on the machine reluctance and increase -thus- the reluctance torque component.

Slot Deformation, however, doesn't influence the main cause of torque ripple, which is (as it will be seen in Chap. 8) the particular and abnormal interaction between stator and rotor, due to some spacial harmonics of flux density.

4.4 Tooth Cut

Second idea is called Tooth cut. It is conceptually similar to Slot Deformation, because it always tries to create obstacles to flux lines in order to drift their path. In this case, however, the obstacle is obtained by shaping the tooth, and no more the slots.
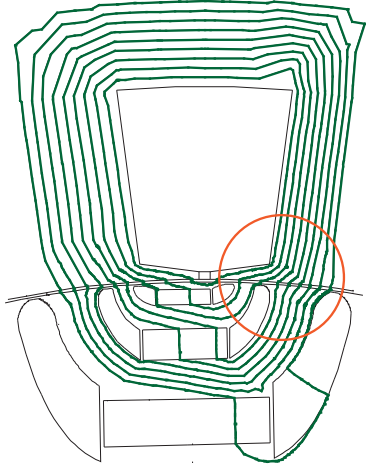
Let's consider again Fig. 3.3(b). For simplicity it is brought back also left here.

As already said, the problem consists on the presence of same sections (orange-circled area) of the magnetic circuit where flux lines have a direction $\in [0; 90]^{deg}$, respect to an horizontal right-oriented reference.

The idea, therefore, is to cut the stator tooth in these area, so that flux lines can see in front of them a longer air-gap. The hope is that the magnetic circuit's reluctance increases and that the field prefers an alternative way where its flux lines have a direction $\in [90; 180]^{deg}$, rather than $\in [0; 90]^{deg}$.

The development of this theory is done through six tests, where the cuts are characterized by two variables. Firstly, a *Cut Height*, h_{cut}, is fixed and simulations are carried out with the change of the second variable, called *Cut Length*, γ_{cut}. Then, the viceversa is done.
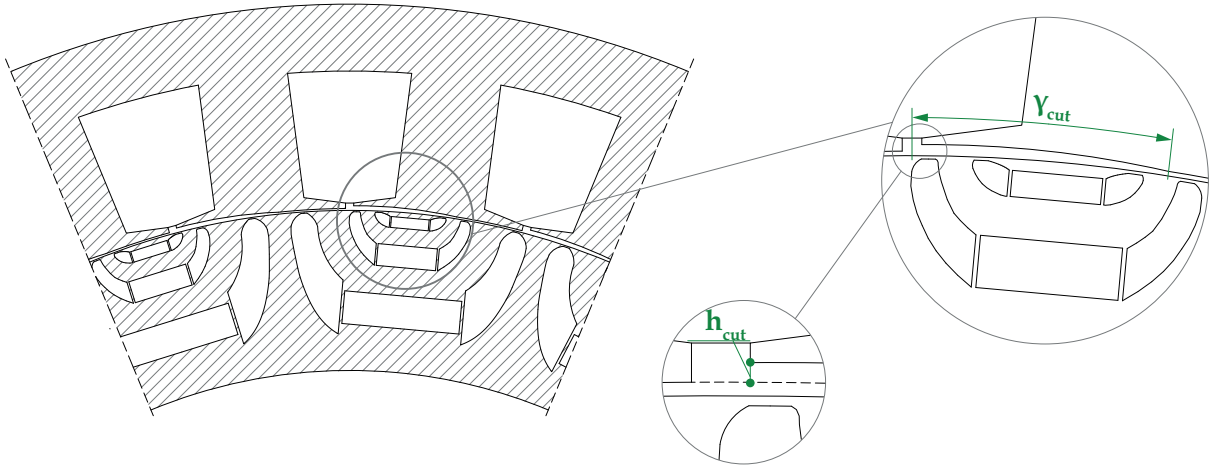In Fig. 4.13, the two variables are highlighted, while in Tab. 4.3 a summary of the tests is reported:

Figure 4.13: Tooth Cut - Variables

|		Test #1	Test #2	Test #3	Test #4	Test #5	Test #6
h_{cut}	$[mm]$	1	1.5	1	1.5	1	1.5
γ_{cut}	$[deg]$	4	4	7.5	7.5	10	10

Table 4.3: Tooth Cut - Implemented tests
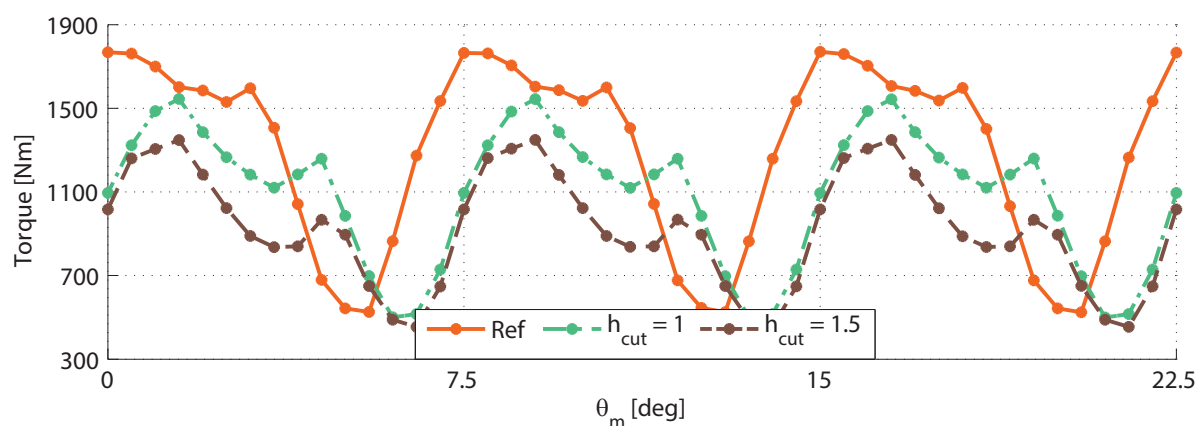
4.5 Tooth Cut - Results

Following: the torque behaviour are reported in Fig. 4.14, with respect to the reference motor's torque ripple, while, the harmonic content of these torques is highlighted in Fig. 4.15. All the graphs have been grouped by *Cut Length* variable, γ_{cut}, for a better display:
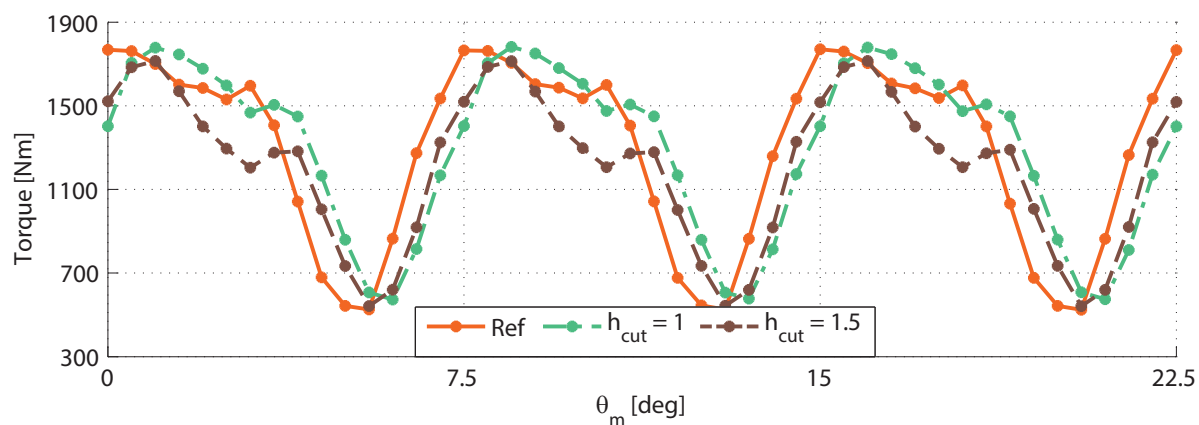
(a) Tests #1 and #2 ($\gamma_{cut} = 4$ ^{deg}) torque ripple
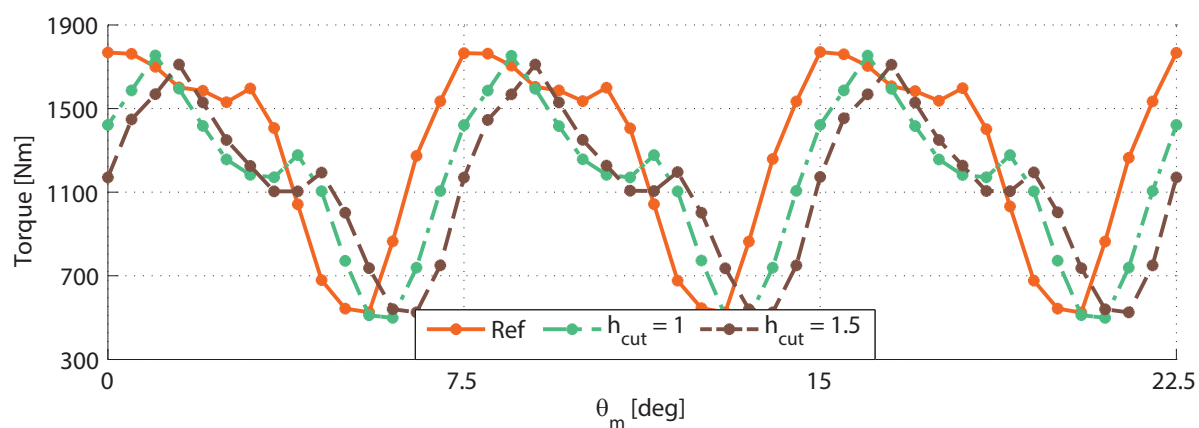
(b) Tests #3 and #4 ($\gamma_{cut} = 7.5$ ^{deg}) torque ripple

(c) Tests #5 and #6 ($\gamma_{cut} = 10$ ^{deg}) torque ripple

Figure 4.14: Tooth Cut - Torque ripple

(a) Tests #1 and #2 ($\gamma_{cut} = 4\ ^{deg}$)

(b) Tests #3 and #4 ($\gamma_{cut} = 7.5\ ^{deg}$)
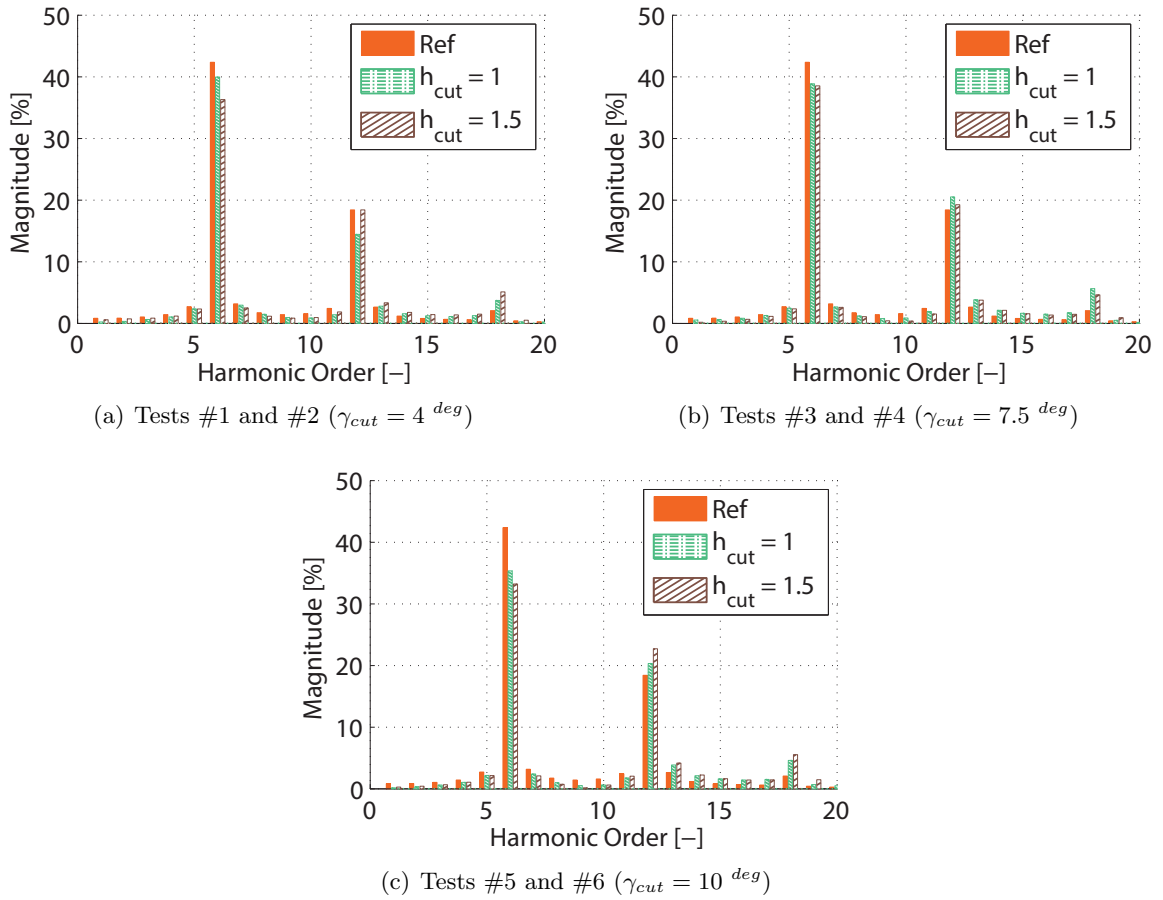

(c) Tests #5 and #6 ($\gamma_{cut} = 10\ ^{deg}$)

Figure 4.15: Tooth Cut - Torque harmonics

4.5.1 Comparison and comments

Since no improvements of performances have been obtained from these technique, no other words want to be further spent to comment the graphs, and simply the numerical results are here reported in Tab. 4.4:

		*ref.	Test #1	Test #2	Test #3	Test #4	Test #5	Test #6
h_{cut}	$[mm]$	0	1	1.5	1	1.5	1	1.5
γ_{cut}	$[deg]$	0	4	4	7.5	7.5	10	10
Minimum	Nm	526	573	543	499	525	500	455
Maximum	Nm	1768	1782	1715	1754	1711	1544	1349
Avg Torque	Nm	1306	1304	1213	1165	1132	1085	922
	$\%$	100	99.85	92.88	89.20	86.68	83.08	70.60
Ripple	$\%$	97.37	92.66	96.69	107.82	104.79	96.31	96.90

Table 4.4: Tooth Cut - Comparison of results

41

More encouraging results have been obtained by *Marzarotto* [5] on other configurations of Slots/Poles. From him simulations, it is possible to observe that:

- - The Tooth Cut technique acts as better on ripple reduction as lower is the machine periodicity. As a matter of fact, in [5] a configuration 3-Slots 2-Pole (similar to 24/16 reference motor) with periodicity 4 is implemented: in these case, too, Tooth Cut shows very limited results, both in absolute terms and with respect to the other machines analysed by the author.

- - From the average torque point of view, it always decreases (more or less) respect to the non-cut stator. And it is true for all the configurations of Slots/Poles.

- - By watching what happens in terms of torque harmonics, finally, it is possible to observe that Tooth Cut particularly conditions the so-called *Slot Harmonics*, that are the torque harmonics of order:

$$n = k \cdot Q_s \pm p$$

  where: k is an index $\in \mathbb{N}_0^+$, Q_s is the slot number and p is an half of pole number.

4.6 Conclusions

In the chapter two strategies are implemented in order to reduce the torque ripple of reference motor: they are called **Slot Deformation** and **Tooth Cut**.
Both the techniques arise from the observation of field maps and from the idea that, in correspondence of those rotor positions where a torque drop occurs, flux lines show some sections with a wrong slope. The direction flux lines undertake ($\in [0 : 90]$ ^{deg}), get the motor to rotate in the wrong direction (clock-wisely) in the attempt to find a lower reluctance position. For this reason, both Slot Deformation and Tooth Cut have the purpose of creating a sort of physical or magnetic "barriers", which are able to deviate the field natural path and to guarantee the latter can orient itself toward a direction $\in [90 : 180]$ ^{deg}.

Results do not show sensible improvements of machine performance: the best reduction of ripple is reached with Slot Deformation. However, not only this decrease is rather limited, but also it is due to magnetic saturation fenomena into some areas of the stator. It means that these result are valid only for the hypothesized power supply (current) conditions. In addition, the applications to whom this motor could be intended are limited, because the asymmetry of stator slots prevents the motor to rotate in both the direction, with the same performances.

Relatively to Tooth Cut, finally, neither this solution leads to good results. The reason can be explained by the work of *Marzarotto* [5], where Tooth cut has been implemented into a comparison between several configurations. The strategy works well on motors with low periodicity and acts mainly on the so-called *Slot Harmonics*. By not being, in the reference motor, sensible contributions of these kind of harmonics, it is clear how Tooth Cut is not able to solve the torque ripple problem of this particular machine.

Chapter 5

Stator Shifting

Up to now, only techniques which have the aim to force flux lines to follow different paths, respect to the natural reference motor ones, have been taken into account. Results were rather unsatisfying and, therefore, a completely new approach is considered hereafter. Still considering stator, the position of whole groups of slots will be here modified. These latter will be rotated of different angles, with respect to a fixed and stationary reference axis. The idea is called **Stator Shifting**: following, thinking and results are reported.

5.1 The idea of Stator Shifting

A large adopted technique in electrical machine design is the rotor skewing: it consists on a twisting, which can be continuous (if possible) or discrete (for instance in PM motors), of the rotor. Skewing will be presented later, in Chap. 7, but it is the basis of Stator Shifting. As a matter of fact, by thinking to skewing, a question arose:

Is it possible to create a sort of Stator Skewing?

Obviously the answer is no: stator, in fact, can't be skewed, because it addresses the coils of the windings. However, a similar result could be obtained if, rather twisting the stator, this latter is split in m parts, and each of these ones is shifted from its starting position. In other words, the idea is to rotate groups of stator slots, respect to a fixed reference, of an angle:

$$k \cdot \Delta\theta_{sh} = k \cdot \frac{\Delta\theta_{sh,TOT}}{s} \qquad\qquad where: \frac{m}{s} \in \mathbb{N}^+ \qquad (5.1)$$

where: k is an integer index, $\Delta\theta_{sh}$ is the shifting step, $\Delta\theta_{sh,TOT}$ is the total shifting angle and s is the number of steps.

Since machine has got a so-high periodicity, t, the aim of Stator Shifting is to mix two opposite magnetic situations, and to reach an intermediate one, consequently. By referring on what has been said in Sect. 3.1, then, Stator Shifting must act so that:

- when a two-pole pitch is in position Ⓖ, the others pitches could be in different positions and produce lower torque contributions;

- when a two-pole pitch is in position Ⓑ, the others pitches could be in different positions and produce higher torque contributions.

The problem, now, is to understand:

- which total shifting angle, $\Delta\theta_{sh,TOT}$, must be chosen;

- how to set the relative shifting angle, $k \cdot \Delta\theta_{sh}$, to each part of the cut stator.

A first idea is the following: since machine has a periodicity 8 (i.e. the magnetic situation repeats itself 8 times in the same way), stator could be cut into $m = 8$ parts. Furthermore, as it has been seen previously, the main contribution on torque ripple is due to the $6-th$ harmonic of torque. These component repeats itself every $60^{\ el\ deg} = 7.5^{\ deg}$, and so this will be the chosen value of $\Delta\theta_{sh,TOT}$ for all the following simulations.

On the other hand, the choice of shifting sequences for the different parts is not univocal. Generally, the choice was made by considering only that sequences which permit the teeth to have widths as homogeneous as possible, in order to avoid a machine with too tight teeth.

In Tab. 5.1, the solutions developed are reported:

Parts	a	b	c	d	e	f	g	h
Two steps (s = 2)	1	0	1	0	1	0	1	0
Four steps (s = 4)	2	1	0	3	2	1	0	3
Four steps (s = 4)	2	0	1	3	2	0	1	3
Eight steps (s = 8)	1	2	4	6	8	7	5	3
Eight steps (s = 8)	1	3	5	7	8	6	4	2

Table 5.1: Stator shifting - Developed sequences ($m = 8$)

Tab. must be read in this way: the parts are labelled a, b, c, d, e, f, g, h; each of them represents a group of three neighbouring slots. The numbers into the table indicates the times the relative part must be shifted (i.e. they are the values of coefficient k, for the different parts). The rotation wise doesn't influence the torque behaviour, as it is not important in correspondence of which tooth the cut is started.

Example 5.1.1. Lets suppose the motor is divided into $m = 6$ parts. Since machine has $Q_s = 24$ stator slots, each part will be characterized by $Q_s/m = 24/6 = 4$ slots per part. Lets consider the generic sequence of $s = 6$ steps: $[1\ 3\ 5\ 6\ 4\ 2]$. It is:

$$a = 1 \qquad b = 3 \qquad c = 5 \qquad d = 6 \qquad e = 4 \qquad f = 2$$

The total shifting angle is $\Delta\theta_{sh,TOT} = 7.5^{\ deg}$ and, so, the shifting step is:

$$\Delta\theta_{sh} = \frac{\Delta\theta_{sh,TOT}}{s} = \frac{7.5^{\ deg}}{6} = 1.25^{\ deg}$$

The 6 parts of the stator will be, therefore, rotated of the angles:

$$k_a = 1 \qquad \Rightarrow \qquad k_a \cdot \Delta\theta_{sh} = 1 \cdot 1.25 = 1.25^{\ deg}$$
$$k_b = 3 \qquad \Rightarrow \qquad k_b \cdot \Delta\theta_{sh} = 3 \cdot 1.25 = 3.75^{\ deg}$$
$$k_c = 5 \qquad \Rightarrow \qquad k_c \cdot \Delta\theta_{sh} = 5 \cdot 1.25 = 6.25^{\ deg}$$
$$k_d = 6 \qquad \Rightarrow \qquad k_d \cdot \Delta\theta_{sh} = 6 \cdot 1.25 = 7.50^{\ deg}$$

$$k_e = 4 \qquad\Rightarrow\qquad k_e \cdot \Delta\theta_{sh} = 4 \cdot 1.25 = 5.00 \,^{deg}$$
$$k_f = 2 \qquad\Rightarrow\qquad k_f \cdot \Delta\theta_{sh} = 2 \cdot 1.25 = 2.50 \,^{deg}$$

In Fig. 5.1 a sketch of the original motor and of the Shifting operation is illustrated. In this case an anticlockwise rotation is set and the Part #1 includes the slots: 1, 2, 3 and 4.
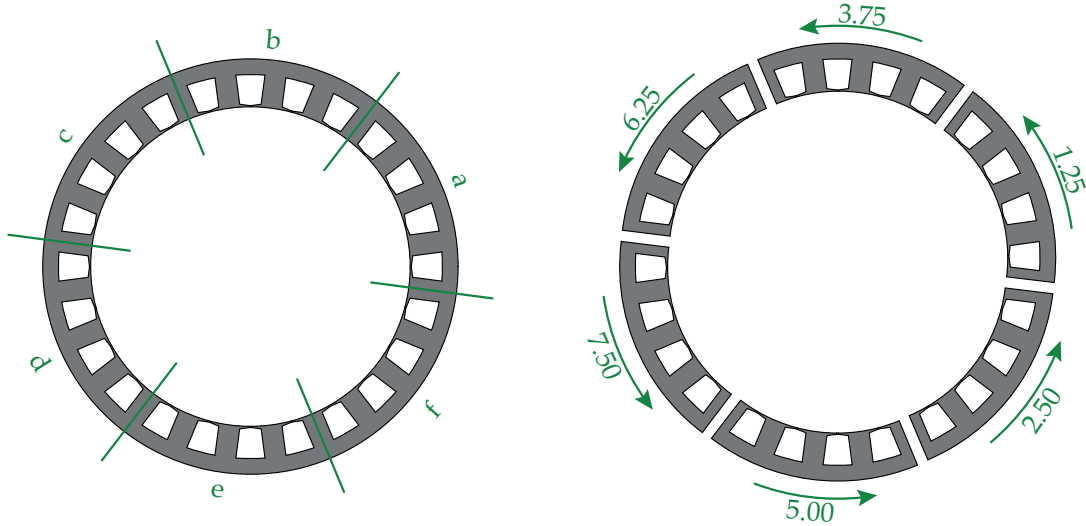

Figure 5.1: Stator Shifting example

5.2 Results

Results of Stator Shifting are here presented. As done in the previous chapter, they show: the Maxwell torque behaviour, the split of these torque into three components, each linked to a specific spacial harmonic of flux density at the air-gap, and -finally- the harmonic content of ripple. Results are grouped by the number of steps which characterize themselves.

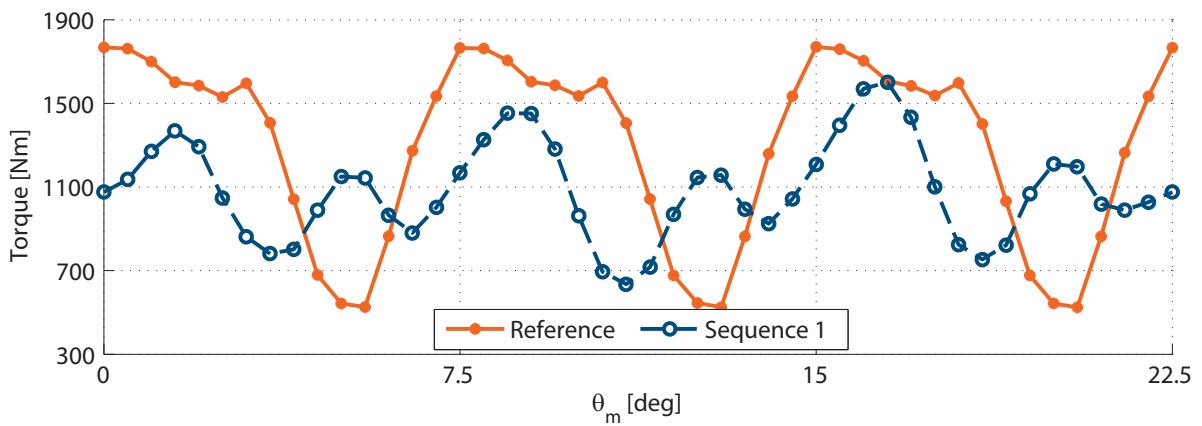### 5.2.1 8 Parts and 2 Steps

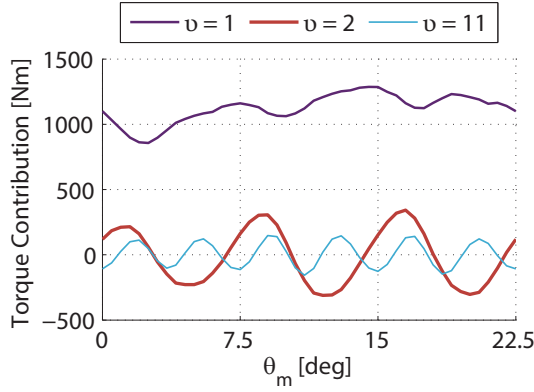
Figure 5.2: 8x2 torque ripple
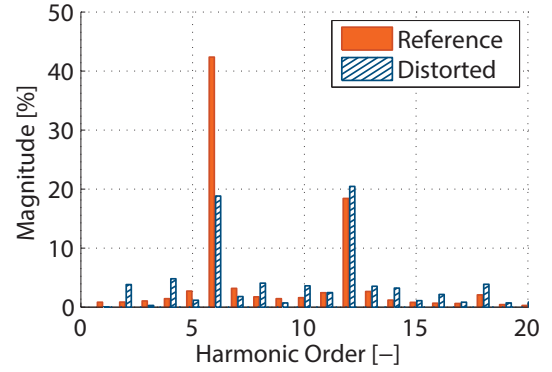
Figure 5.3: Torque contributions

Figure 5.4: 8x2 torque harmonics

First results are encouraging: Stator Shifting 8x2, in fact, modifies deeply the torque behaviour (Fig. 5.2). In particular, by referring to Fig. 5.3:

- the torque component associated to the first spacial harmonic of flux density decreases;

- the torque component linked to the second spacial harmonic decreases, too: in the reference motor it showed a peak beyond the value $\hat{T}_2 = 500Nm$. Here it doesn't reach $\hat{T}_2 = 400Nm$.

All these considerations confirm the results:

$$T_{avg} = 1087Nm \qquad\qquad T_{ripple} = 88.87\%$$

Relatively to the harmonic content of ripple, Fig. 5.4 shows an important reduction of the $6-th$ harmonic of torque (from 42.40% to 18.82%), while its multiples ($12-th$ and $18-th$) remains unchanged or, however, increase a few.

In addition, it is possible to note an increase of several minor harmonics, ζ, which seem to follow a law like the following:

$$\zeta = 3 \cdot k \pm 1 \qquad\qquad where: k = 1, 3, 5, 7 \qquad\qquad (5.2)$$

5.2.2 8 Parts and 4 Steps

The following test is characterized by a rotation of 4 steps. Since different sequences have been taken into account for these configuration, graphs have to be read in the following way: in Fig 5.5 a comparison is shown between the reference motor torque behaviour and the two sequences ones. Fig. 5.6 shows the split of torque into the three components related to the spacial field harmonics seen above, $\upsilon = 1$, $\upsilon = 2$ and $\upsilon = 11$. For simplicity, only one sequence is considered in the figure (the second one).

Finally, in Fig. 5.7, the torque harmonic contents are reported for all the three curves of the first figure. The meaning of styles and colours is maintained between the first and the third figure.
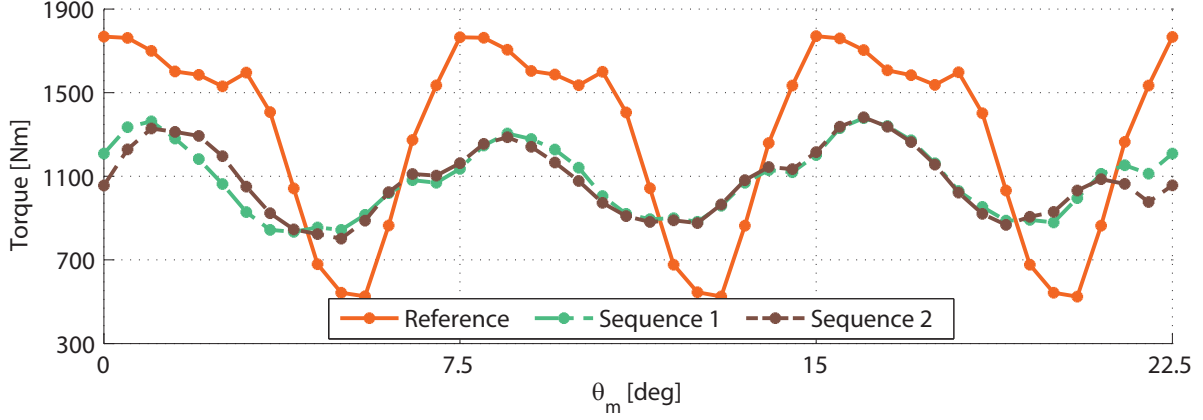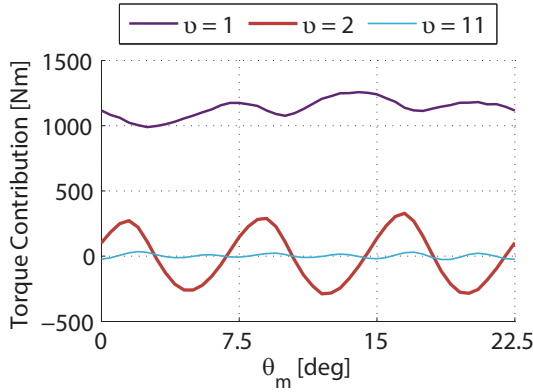
Figure 5.5: 8x4 torque ripple
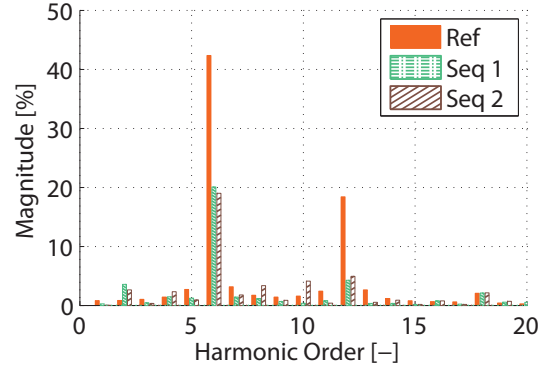

Figure 5.6: Torque contributions

Figure 5.7: 8x4 torque harmonics

The more significant result, in this case, is the reduction also of the $12 - th$ torque harmonic, as well as the $6 - th$, as Fig. 5.7 shows: from 42.40% to 20% and 19%, and from 18.42% to 4.28% and 4.94%, respectively. No changes are observed on the $18 - th$ harmonic, instead.

It is difficult to do considerations on the other harmonics, because different results have been obtained from the two sequences. The reason, probably, is the fact that the two simulated motors are characterized by different constrictions of the teeth.

To understand it, let's consider the implemented sequences: $\begin{cases} Seq.1 : [2\ 1\ 0\ 3\ 2\ 1\ 0\ 3] \\ Seq.2 : [2\ 0\ 1\ 3\ 2\ 0\ 1\ 3] \end{cases}$

The change of teeth width is proportional to the difference between two neighbouring coefficients. For instance, let's focus on $Seq.1$: the first coefficient is $a = 2$, while the second is $b = 1$. Then, the tooth between the first part (part $1 \rightarrow$ coefficient a) and the second one (part $2 \rightarrow$ coefficient b) will shrink or stretch itself proportionally to the angle:

$$(a - b) \cdot \Delta\theta_{sh} = (a - b) \cdot \frac{\Delta\theta_{sh,TOT}}{s} = (2 - 1) \cdot \frac{7.5}{4} = 1.875 \ ^{deg}$$

By applying this procedure to the whole sequences, it is:

47

Differences	$(a-b)$	$(b-c)$	$(c-d)$	$(d-e)$	$(e-f)$	$(f-g)$	$(g-h)$	$(h-a)$
Sequence 1	1	1	-3	1	1	1	-3	1
Sequence 2	2	-1	-2	1	2	-1	-2	1

As it can be observed, the constriction (or the lengthen) of teeth is different between the two sequences: in one case it is proportional to 1 or 3 times the angle $\Delta\theta_{sh}$, in the other one it is proportional to 1 or 2 time the same angle.

Hereafter, hence, only homogeneous sequences (i.e. sequences where the differences between coefficients are the same) must be compared.

5.2.3   8 Parts and 8 Steps

The last Shifting configuration is the 8x8 one. In this case two homogeneous sequences are taken into account: both the sequences, in fact, are characterized by the same teeth widths (whose reduction is proportional to 1 or 2 times the skewing step). Theoretically, similar results are expected, both in terms of torque trend and torque harmonic content.
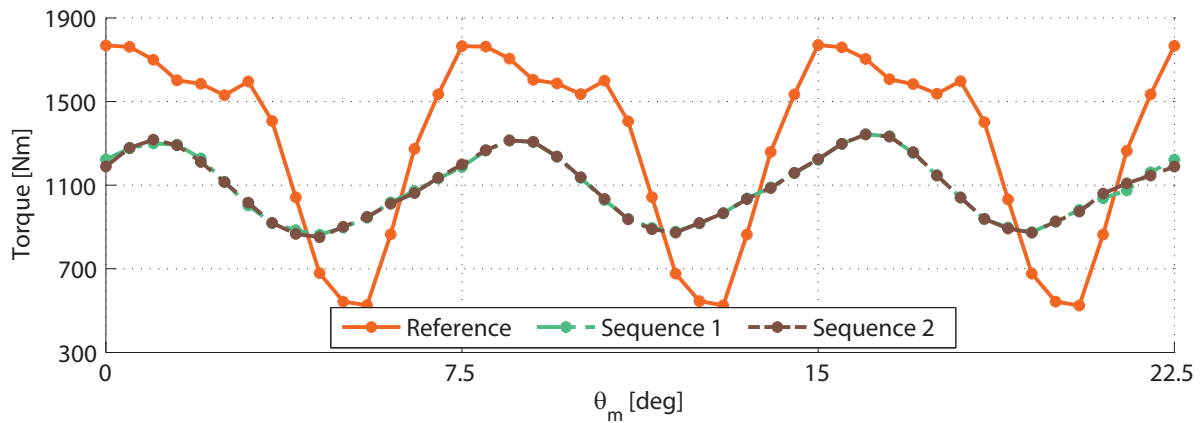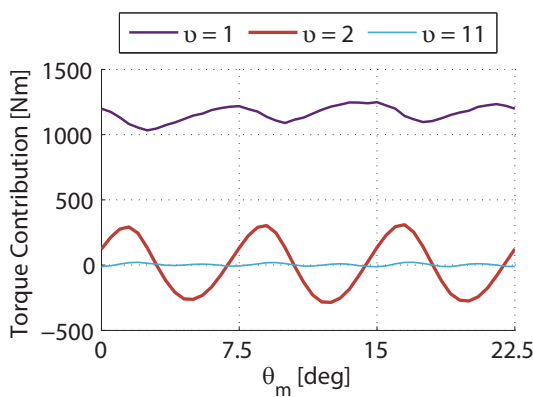

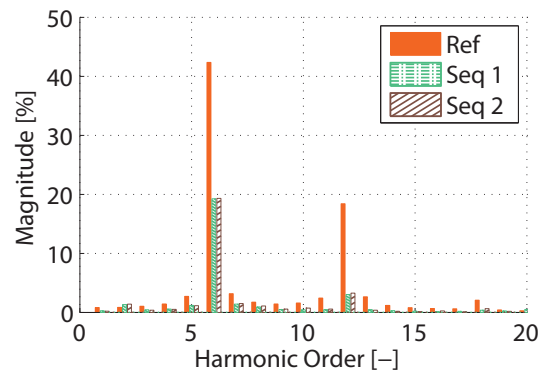Figure 5.8: 8x8 torque ripple

Figure 5.9: Torque contributions

Figure 5.10: 8x8 torque harmonics

Graphs confirm what has been supposed. In addition, the best results are here obtained, in terms of torque ripple reduction:

$$T_{avg} = 1093/1092 Nm \qquad\qquad T_{ripple} = 43.92/44.96\%$$

From the harmonic content point of view, this shifting configuration leads to a general reduction of all the harmonics components, both the mains $(6-th,\ 12-th$ and $18-th)$, and the minors.

5.2.4 Comparison and comments

Results obtained from the simulations are reported in Tab. 5.2:

		*ref.	First tests				
Parts	$[-]$	-	8	8	8	8	8
Steps	$[-]$	-	2	4	4	8	8
Sequence	$[-]$	-	-	1	2	1	2
Minimum	Nm	523	635	834	802	863	851
Maximum	Nm	1795	1601	1378	1382	1343	1342
Average Torque	Nm	1306	1087	1086	1078	1093	1092
	$\%$	100	83.23	83.15	82.54	83.69	83.61
Ripple	$\%$	97.36	88.87	50.09	53.80	43.92	44.96

Table 5.2: Stator shifting - Comparison of results

Table shows how, with the same number of parts, m, the machine ripple, T_{ripple}, always more decreases as the number of steps, s, increases.

In addition, all the simulations leads the average torque, T_{avg}, to decrease. However, differently from the ripple behaviour, there is no variations in T_{avg} as the step number, s, changes. There is a fixed reduction of $\Delta T_{avg} \approx -17\%$ with respect to the reference motor, and this value doesn't change between the tests.

5.3 Other tests

Until now only the number of steps, s, has been changed. The number of parts, m, instead, has been maintained fixed. The idea, now, is to understand if something can change when also the number of parts, m is varied. Since stator must be cut in regular parts with an integer number of slots, m must be a divisor of $Q_s = 24$. The possibilities taken into account are: $m = 6, 12, 24$, and for each of them, only the condition $m = s$ is developed. Therefore:

Parts	a	b	c	d	e	f
Six steps (s = 6)	1	2	4	6	5	3

Table 5.3: Stator shifting - Developed sequences ($m = 6$)

Parts	a	b	c	d	e	f	g	h	i	j	k	l
Twelve steps (s = 12)	1	2	4	6	8	10	12	11	9	7	5	3
Twelve steps (s = 12)	1	3	5	7	9	11	12	10	8	6	4	2

Table 5.4: Stator shifting - Developed sequences ($m = 12$)

| Parts | a | b | c | d | e | f | g | h | i | j | k | l |
	m	n	o	p	q	r	s	t	u	v	w	x
Twenty-four	1	3	5	7	9	11	13	15	17	19	21	23
steps (s = 24)	24	22	20	18	16	14	12	10	8	6	4	2
Twenty-four	1	2	4	6	8	10	12	14	16	18	20	22
steps (s = 24)	24	23	21	19	17	15	13	11	9	7	5	3

Table 5.5: Stator shifting - Developed sequences ($m = 24$)

5.3.1 6 Parts and 6 Steps

Results are here reported. The same graphs of the previous Sections, with the same conventions of colours and style, are reported.
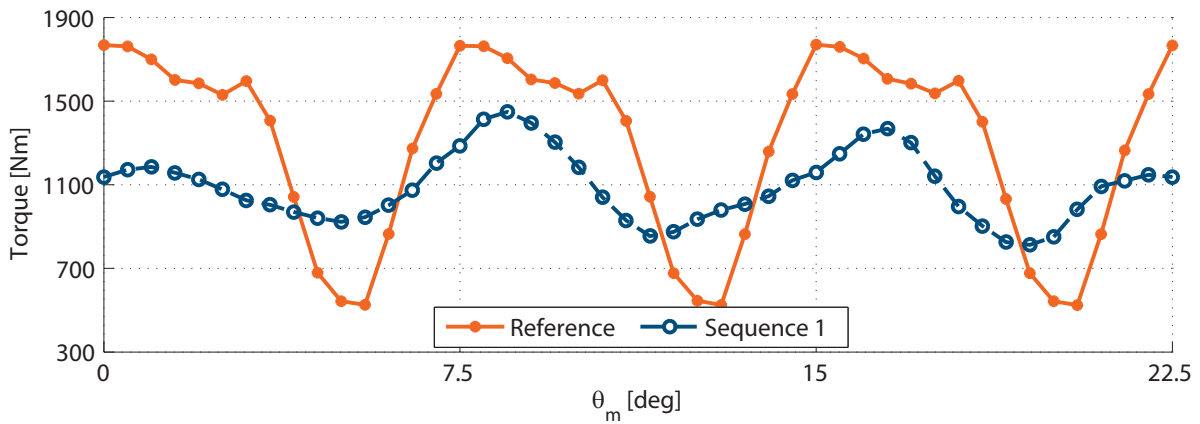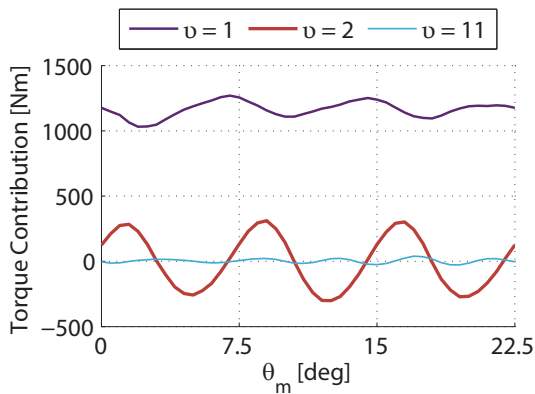

Figure 5.11: 6x6 torque ripple

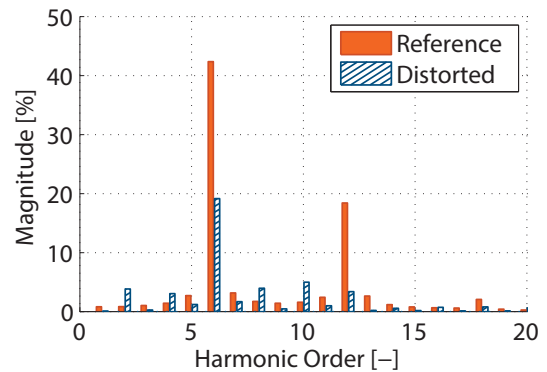Figure 5.12: Torque contributions

Figure 5.13: 6x6 torque harmonics

The main torque harmonics ($6-th$, $12-th$, $18-th$) are well reduced, but an important increase of the minor ones is evident. The performance, hence, are better respect to the reference motor, but not with respect to the previous 8x8 configuration. Similar considerations can be made also for the following results: the torque ripple reduction improves always more, but it is difficult to reach better results respect the best solution found in the previous Section.
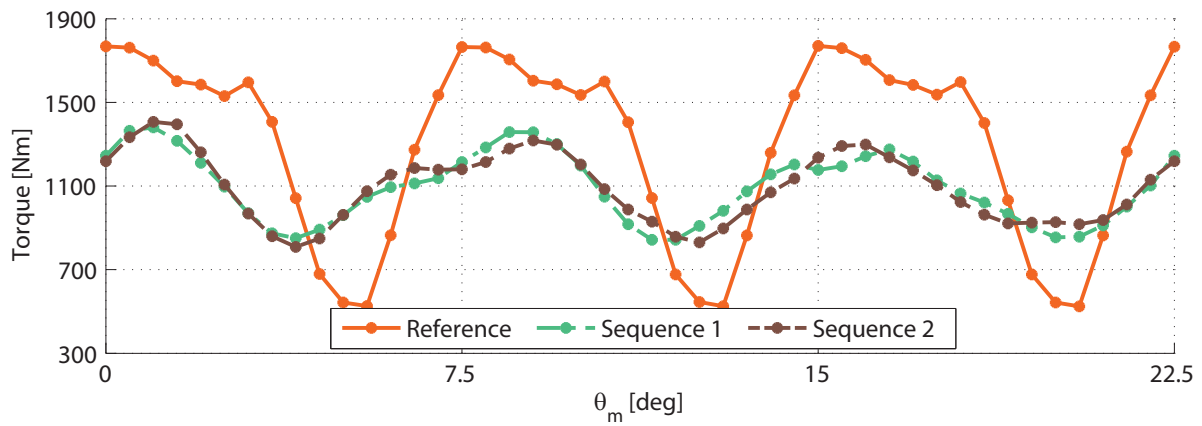
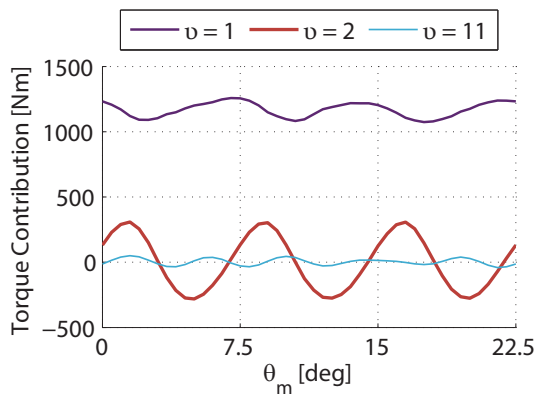## 5.3.2   12 Parts and 12 Steps

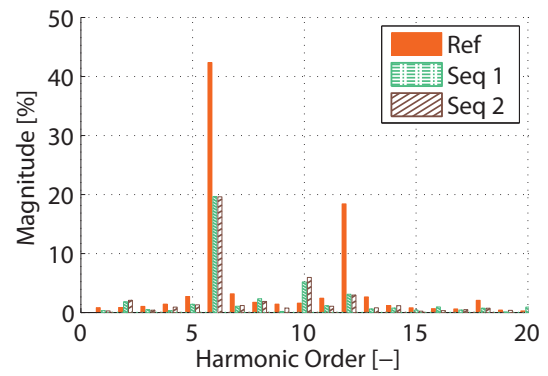Figure 5.14: 12x12 torque ripple

Figure 5.15: Torque contributions

Figure 5.16: 12x12 torque harmonics

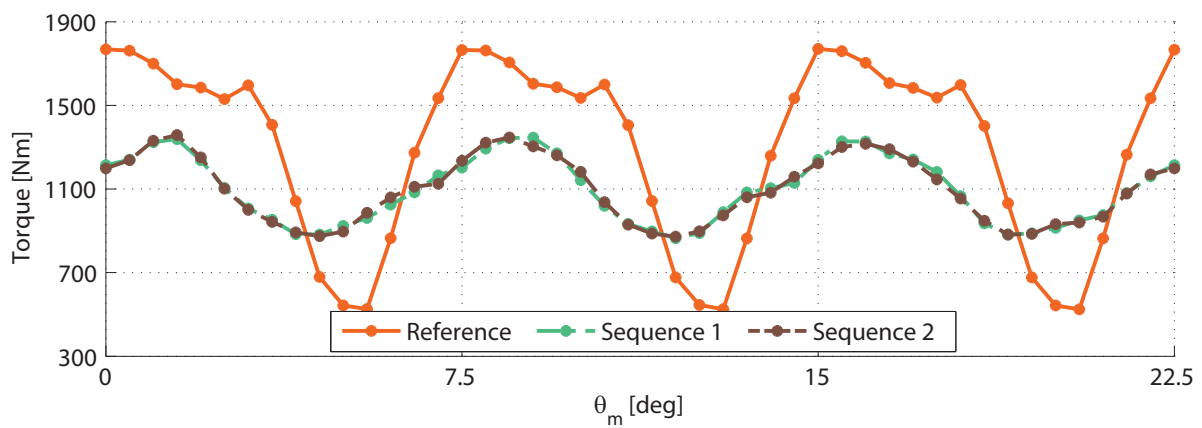## 5.3.3   24 Parts and 24 Steps
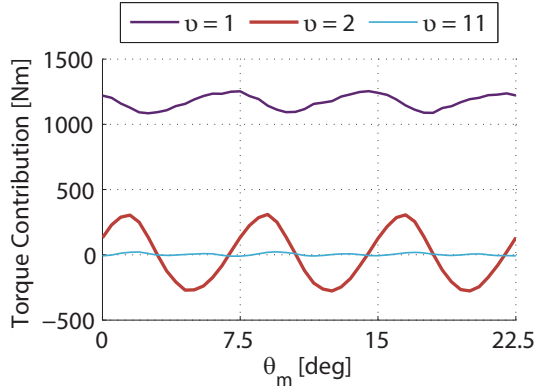

Figure 5.17: 24x24 torque ripple
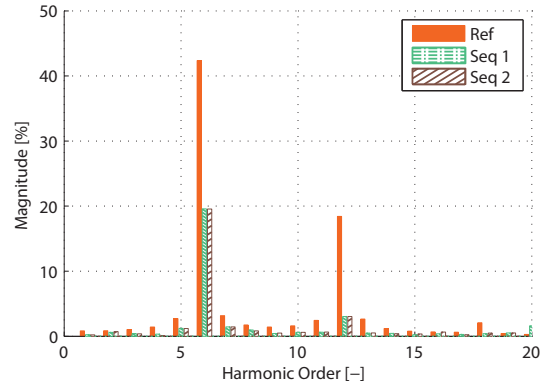
Figure 5.18: Torque contributions

Figure 5.19: 24x24 torque harmonics

5.3.4   Comparison

The tests just presented have a similar effect of the first simulations, executed with $m = 8$, and no additional improvements of performance are obtained: the average torque decrease is still fixed around a value $\Delta T_{avg} \approx -16\%$, while ripple does not decrease beyond the 44%. In Tab. 5.6, results are reported:

		*ref.	Other tests				
Parts	$[-]$	-	6	12	12	24	24
Steps	$[-]$	-	6	12	12	24	24
Sequence	$[-]$	-	-	1	2	1	2
Minimum	Nm	523	813	843	809	865	872
Maximum	Nm	1795	1449	1381	1407	1346	1358
Average Torque	Nm	1306	1091	1096	1095	1098	1097
	$\%$	100	83.54	83.92	83.84	84.07	84.00
Ripple	$\%$	97.36	58.30	49.09	54.61	43.81	44.30

Table 5.6: Stator shifting - Comparison of results

5.4   Conclusions

In this chapter, a new theory has been proposed: it is called **Stator Shifting** and can be considered as an evolution of the well-known *Rotor Skewing*. It consists on the change of position for groups of stator slots, which are rotated of some specific angles, with respect to a fixed and stationary reference axis.

The way stator is cut and the rotation wise are not important because similar results would be obtained. The main variables are: the total shifting angle, $\Delta\theta_{sh,TOT}$, and the number of steps, s. They are linked by the law:

$$\Delta\theta_{sh,TOT} = s \cdot \Delta\theta_{sh} \tag{5.3}$$

where $\Delta\theta_{sh}$ is called *Shifting Step*.

Two groups of simulations has been done: firstly, the number of parts in which the stator is cut has been fixed at $m = 8$. In this case, since s must be an integer divisor of m, the possible steps were: $s = 1, 2, 4, 8$, where $s = 1$, obviously, has no sense.
Secondly, the number of parts has been modified, and by considering only the case of $m = s$, three other configurations of Shifting has been implemented.

In Tab. 5.7 all the studied Stator Shifting configurations are summarized, with their results. The units of measure are:

$[-]$ for "Parts", "Steps", "Sequences" and "$T_{Avg,\%}$"

$[Nm]$ for the torques: "T_{min}", "T_{max}", "T_{Avg}" and "T_{Ripple}"

	*ref.	First tests					Other tests				
Parts	-	8	8	8	8	8	6	12	12	24	24
Steps	-	2	4	4	8	8	6	12	12	24	24
Seq.	-	-	1	2	1	2	-	1	2	1	2
T_{Min}	523	635	834	802	863	851	813	843	809	865	872
T_{Max}	1795	1601	1378	1382	1343	1342	1449	1381	1407	1346	1358
T_{Avg}	1306	1087	1086	1078	1093	1092	1091	1096	1095	1098	1097
$T_{Avg,\%}$	100	83.23	83.15	82.54	83.69	83.61	83.54	83.92	83.84	84.07	84.00
T_{Ripple}	97.36	88.87	50.09	53.80	43.92	44.96	58.30	49.09	54.61	43.81	44.30

Table 5.7: Stator shifting - Comparison of results

As it can be observed in table, the Stator Shifting technique leads to rather important results: also if the average torque decreases of a value $\Delta T_{avg} \approx -17\%$, the most evident information is the sensible reduction of ripple, which decreases beyond the 50% of its original value (reference motor).

Unfortunately, it is difficult to define a general rule which manages the behaviour of Shifting. For the moment, it is possible to note what follows:

- The average torque remains almost constant for all the implemented combinations. Since the only variable which has been maintained fixed for all the simulations is the Total Shifting Angle, $\Delta\theta_{sh,TOT} = 7.5$ ^{deg}, this could exactly be the variable which influences the average torque, T_{avg}. A future development of these technique could investigate and confirm (or deny) this idea.

- From the torque ripple point of view, it changes sensibly on the basis of which Shifting configuration is chosen, and -in particular- it tends to decrease with the increase of step number, s.
  But it is not always true: this behaviour is verified only when the values of s are divisors of the machine periodicity, t. When different values are chosen, the ability of Stator Shifting to decrease the ripple can anyway occurs (for instance it is the case of Shifting 24x24), but in any case, better results are not reached, with respect to that solutions with s divisor of t.

Chapter 6

Optimization of rotor barrier shape

In this chapter the best geometry for the rotor barriers has been studied. In order to do it, a multiobjective Differential Evolution optimization, with non-dominant sorting is implemented. Algorithm and results are reported.

6.1 The algorithm

The design of rotor barriers is a problem with an enormous number of variables. The best solution can't be reached analytically and, so, a numerical optimization is necessary. In addition, it should be remembered that there are two different goals to consider: the maximization of average torque and the reduction of its ripple. Therefore, for our purpose, a multiobjective optimization is the solution. In particular, *Alotto et al.* [4] developed an algorithm, based on a Differential Evolution optimization and with a non-dominant sorting of the individuals, for other motor's typologies. The same script has been inherited and adapted for the PMASynRel motor under analysis.

The operating principle of a generic evolutionary algorithm can be schematised as in Fig. 6.1:
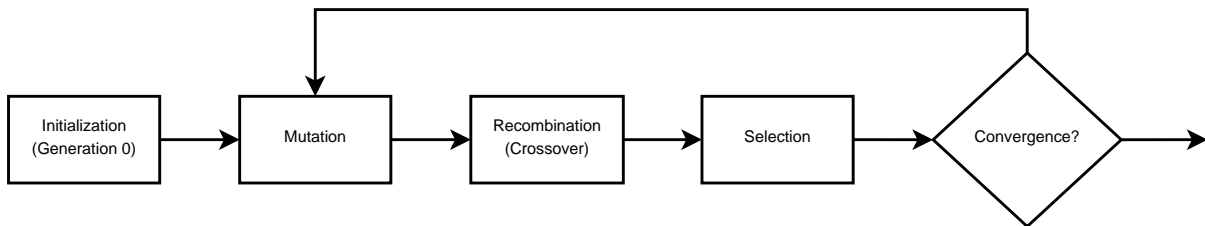

Figure 6.1: Typical evolutionary scheme

The problem starts with the creation of a random *Generation 0*, composed of $N = 10$ individuals (motors), which are characterized by the matrix $[x] = (x_1; x_2; x_3, ..., x_{14})$. The vectors, x_i, are the geometrical parameters of the rotor (see Fig. 6.2), that are: x_1 is called K_{air} and it is the ratio between the 3 magnets' radial length and the total radial lenght of the rotor; x_2, x_3 and x_4 are the barrier angles, $\theta_{b,i}$; the variables from x_5 to x_{13} are, respectively, the radii, $r_{m,i}$, the widths, $w_{m,i}$, and the heights, $h_{m,i}$, of the 3 magnets; x_{14} is the ribs height (that is the same for all the barriers), h_{ribs}.
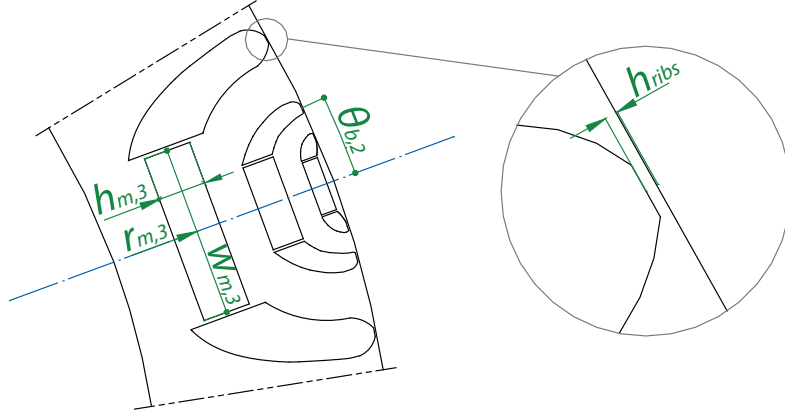
Figure 6.2: Variables which define the chromosome

Now, as it happens into the evolutionist stages, a first generation, G, will produce a second (daughter) generation, $G + 1$, and this is true for all the M generations which want to be considered. In order to engender a new generation, the parent's "*chromosomes*", that are the values of $[\boldsymbol{x}]$ matrix, must recombine themselves. In additions, throughout the mechanism of *crossover*, local mutations could occur: these ones are considered into the *mutation* mechanism. After a finite number of generations, the optimization will lead to an adaptation of the species: the individuals (motors) which are able to better adapt themselves to the environment (to the optimization's objectives), will survive; viceversa, individuals which are not able to adapt themselves as well as the previous ones will be discarded. This last process is called *selection*.

6.1.1   Mutation mechanism

Mutation is a part of the evolutionary algorithm. Due to the strong aggressiveness whereby a Differential Evolution tends to converge toward a minimum solution, it's necessary to force the evolution in the exploration of the whole $\mathbb{R}^{14}$ available space. Thus, also when the optimization will be relatively near to the optimum, it will be distanced from the convergence and it will be driven toward that domain's areas (not yet explored) where other minimum points could be present.

From the algorithm point of view, mutation occurs with the insertion of a "mutant" vector, defined as:

Definition (Mutant Vector). *Given a generation, G, for each vector, $\boldsymbol{x_{i,G}}$, a **mutant vector** is defined as the vector:*

$$\boldsymbol{v_{i,G+1}} = \boldsymbol{x_{i,best}} + F \cdot (\boldsymbol{x_{j,G}} - \boldsymbol{x_{k,G}}) \qquad with: \qquad \begin{array}{l} i, j, k = 1, 2, ..., 14 \\ i \neq j \neq k \end{array} \tag{6.1}$$

where: the subscript *best* specify that only the best $\boldsymbol{x_i}$ vector found into the generations up to the G-*th* one is considered, while F is a specific coefficient, called *mutation factor*.

In Fig. 6.3 a logical scheme of mutation mechanism is reported. For simplicity, the vector, $\boldsymbol{x_{i,G}}$, is the best one, too.
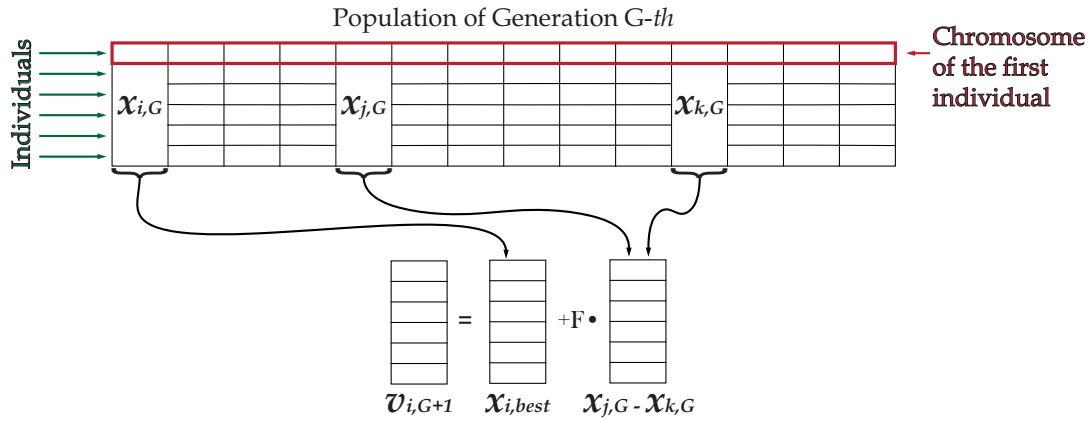
56

Figure 6.3: Mutation mechanism

6.1.2 Crossover mechanism

Crossover is the following step. It consists on a random re-combination of the G-*th* generation's chromosomes, so that a new G+1-*th* generation can be arise. Crossover occurs when a new $[\boldsymbol{x}]$ matrix is created, like this:

Definition (Trial Vector). *Given a generation, $G+1$, each $\boldsymbol{x_{i,G}}$ vector of the previous generation is substituted by a **trial vector**, $\boldsymbol{u_{i,G+1}}$, achieved from the random element's combination of $\boldsymbol{x_{i,G}}$ and its associated $\boldsymbol{v_{i,G+1}}$ vector.*

In Fig. 6.4 a logical scheme of crossover mechanism is reported:
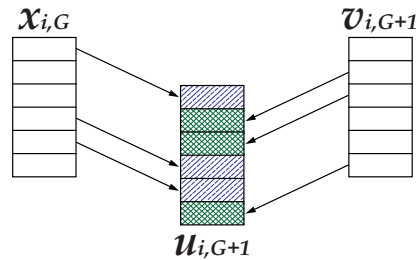

Figure 6.4: Crossover mechanism

Once the new $[\boldsymbol{x}]$ matrix is created, it will be used in order to define the new $N = 10$ "sons" motors. Then, they will be implemented in the FE software, and it will return to the algorithm, the two objective values (average torque and ripple).

6.1.3 Selection mechanism

The last algorithm step is *selection*. The question *selection* wants to reply is: "Is the solution just found, by using the trial vector, $\boldsymbol{u_{i,G+1}}$, better (or worse) with respect to the previous solutions?"

In order to reply, the concept of *non-dominance* is introduced:

Definition (Pareto Non-Dominance). *Defined the plane with axes (Average torque / Ripple), a point of this plane corresponds to an algorithm's solution. This point is defined* **non-dominated** *if no other points are better in terms of average torque and torque ripple, at the same time.*
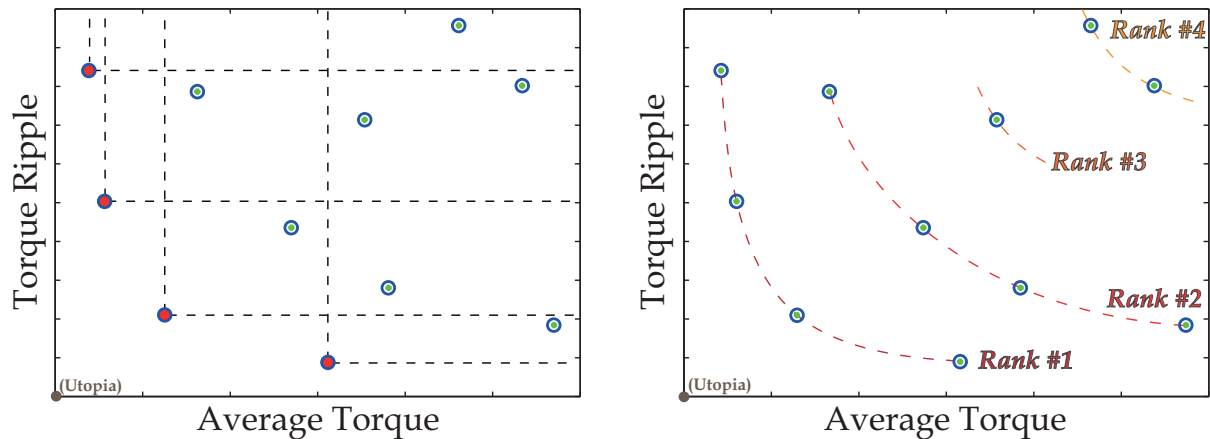

Figure 6.5: Pareto Non-Dominance criterion

Understood the concept of *non-dominance*, and remembering that Pareto-front is exactly the locus of points where the optimum solutions (i.e. all the non-dominated ones) are defined, the selection process for every generation can be summarized as follow:

1- Non-dominated points are calculated, as on the left side of Fig. 6.5. These points define the rank #1 Pareto front;

2- The solutions associated to Pareto front of rank #1 are reputedly removed and the criterion of non-dominance is applied to that points which will set up the Pareto front of rank #2. And so on, for rank #3, #4, etc. This leads to the graph on the right side of Fig. 6.5;

3- Once all the points of the plain are classified, they are ordered and saved into an archive: at the first positions the rank #1 solutions and then the following ranks up to the complete filling of the archive size. In the case of iso-rank solutions, the order is such that the more equispaced points are favourite: the reason of that is the attempt to avoid the Pareto front could be well set up in the more crowded zones, while it could be simply approximated in the more scattered areas.

Thus, a set of non-dominated solutions as more equispaced as possible are obtained. The union of these points defines the real Pareto front.

NOTE: It is important to remember that, from a statistical point of view, the solutions belonging to Pareto front must be considered equipollent: a specific motor can't be defined *better* than the other ones. The choice of a more suitable machine must be led on the basis of other criteria, which have nothing to do with the optimization algorithm. For instance: costs, losses, simplicity in manufacturing, etc...

6.2 The optimization

Ranges associated to the different variables, x_i, have been initially set rather wide, because there was no enough sensibility on the problem and on the consequences that a specific variable could have had on the objectives. They are reported here:

x_1 :	from	0.2	to	0.6
x_2 :	from	2^{deg}	to	3.5^{deg}
x_3 :	from	4^{deg}	to	6^{deg}
x_4 :	from	7^{deg}	to	10.5^{deg}
x_5 :	from	$220\ mm$	to	$245\ mm$
x_6 :	from	$8\ mm$	to	$16\ mm$
x_7 :	from	$2\ mm$	to	$6\ mm$
x_8 :	from	$210\ mm$	to	$215\ mm$
x_9 :	from	$12\ mm$	to	$25\ mm$
x_{10} :	from	$2\ mm$	to	$10\ mm$
x_{11} :	from	$205\ mm$	to	$210\ mm$
x_{12} :	from	$20\ mm$	to	$50\ mm$
x_{13} :	from	$2\ mm$	to	$20\ mm$
x_{14} :	from	$0.4\ mm$	to	$0.8\ mm$

Archive dimension	50	items
Population size	10	individuals
Generations	40	[-]

Results have not reached a full convergence, because not all the stored final solutions are points of Pareto front of rank #1. This doesn't involve heavy consequences: simply, the conclusion is that the final Pareto front of rank #1 will not be defined by 50 individuals, as the archive dimension, but only by 17 points. In Fig. 6.6 scattering of the simulated motors is reported and, in addition, the final Pareto front is highlighted by orange circles.
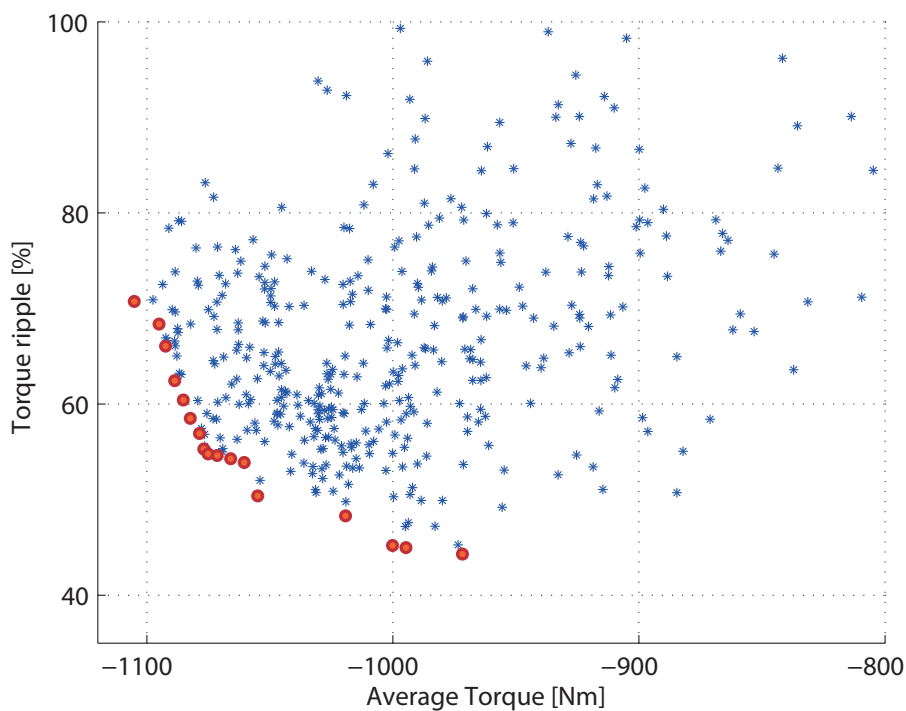

Figure 6.6: Pareto front for the first optimization

The first clear characteristic shown in the figure is the reduction of the torque ripple: apart from some scattered solutions on the top of graph, a strong confluence of points is present into the range of ripple $50\% \div 70\%$. From the average torque point of view, instead, the trend is negative, in the sense of a reduction of the torque: only a single motor overtakes $1100Nm$.

Now, the solutions of the front are all characterized by very limited magnets' dimensions: they are small, tight or short, while most of the space is occupied by the air barriers.
This leads to think that an another optimization is necessary, with the aim of reviewing variables limits: the idea is to force the optimizator to design machines with bigger magnets. Here after the new values are:

					x_1 :	from	0.2	to	0.6
					x_2 :	from	$2\ ^{deg}$	to	$3.5\ ^{deg}$
					x_3 :	from	$4\ ^{deg}$	to	$6\ ^{deg}$
					x_4 :	from	$7\ ^{deg}$	to	$10.5\ ^{deg}$
					x_5 :	from	$220\ mm$	to	$245\ mm$
Archive dimension	50	items			x_6 :	from	$8\ mm$	to	$16\ mm$
Population size	10	individuals			x_7 :	from	$4\ mm$	to	$8\ mm$
Generations	50	[-]			x_8 :	from	$209\ mm$	to	$215\ mm$
					x_9 :	from	$12\ mm$	to	$35\ mm$
					x_{10} :	from	$5\ mm$	to	$10\ mm$
					x_{11} :	from	$200\ mm$	to	$208\ mm$
					x_{12} :	from	$20\ mm$	to	$60\ mm$
					x_{13} :	from	$15\ mm$	to	$30\ mm$
					x_{14} :	from	$0.4\ mm$	to	$0.8\ mm$

NOTE: This forcing could shrink too much the channel height between two neighbouring barriers and -consequently- it could lead lamination to saturation in those areas. This is the reason why also the inner rotor diameter has been reduced, from $D_f = 380mm$ to $D_f = 350mm$.

In Fig. 6.7, scattering and final Pareto front connected to the second optimization are reported: the graph effectively shows the trend of new individuals to crowd the south-western corner of the plane, i.e. they are approaching to the utopia condition: the ripple range decreases from $50\% \div 70\%$ to $45\% \div 60\%$, while the average torque, which before was rather distributed (scattered), now is concentrated around the value of $1100Nm$.

Definitively, the optimization leads to a sensible reduction of the ripple, also if a small but not negligible reduction of average torque is present.

A limit of the graph of Fig. 6.7 is as follow: in the first optimization, the Pareto front points were rather spread (equi-spaced) and their union allowed us to draw a regular and clean spline. This leads to think that the drown spline was a good approximation of the real Pareto front. Viceversa, in the second optimization, non-dominant points of the $50th$ generation give the impression that algorithm does not reached an out-and-out convergence: their union, in fact, doesn't draw a regular front, but a rather chopped one. Probably, when the algorithm stopped (at generation 50), it was finding a new Pareto front, closer to the real one, as highlighted in Fig. 6.8.

This is the reason why results have been taken into account cautiously: although all the orange

circled solutions of Fig. 6.7 should be considered -strictly speaking- as equivalents, actually, the only solutions that will be considered are those ones highlighted in green, in Fig. 6.8:
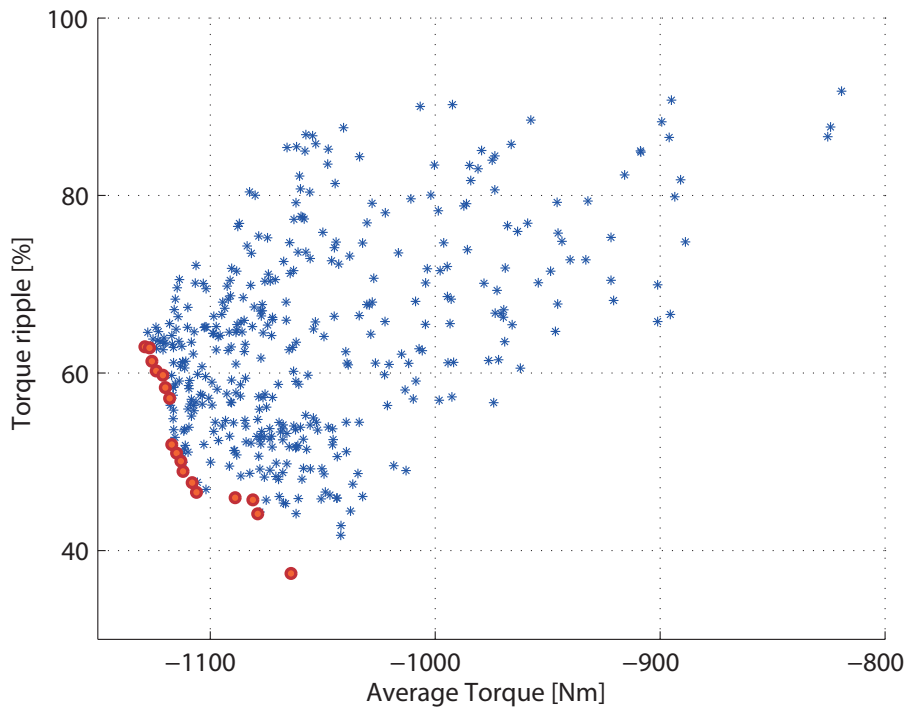

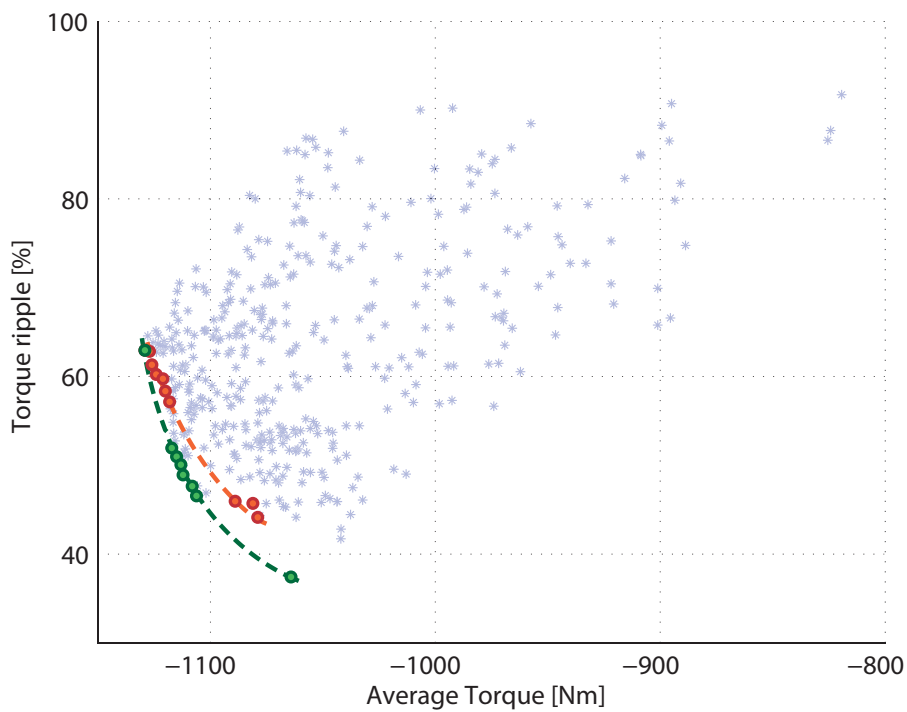Figure 6.7: Pareto front for the second optimization

Figure 6.8: Second optimization - Highlighted fronts

Relatively to these green points, the following observations can be done:

- The machine on the bottom right side, also if very interesting because of its low value of torque ripple, is characterized by a too low average torque. There are other solutions (stator shifting, skewing, etc...) which allow to further reduce the torque ripple of the optimized machine. All these solutions ask for a sacrifice in terms of average torque. Hence, there is no sense in the choice of a machine with an already low average torque, because -thus- no other strategies could be implemented without an excessive loss of torque;

- Shifting attention on the central solutions, obviously, the interest will be only for the machine with lowest ripple. As a matter of fact, the (very limited) average torque increase relative to the near points of the plane does not be justified because of the simultaneous increase of the torque ripple;

- The last solution, on the top of the front, shows a high average torque and could be an another possible solution.

Definitively, the second motor from the bottom is chosen as personal optimum solution. The characteristics of this motor are the following:

x_1	x_2	x_3	x_4	x_5	x_6	x_7	x_8
0,45	$0,05^{rad}$	$0,10^{rad}$	$0,15^{rad}$	$224\ mm$	$12\ mm$	$8\ mm$	$215\ mm$

x_9	x_{10}	x_{11}	x_{12}	x_{13}	x_{14}	**Torque**	**Ripple**
$33\ mm$	$8\ mm$	$205\ mm$	$57\ mm$	$23\ mm$	$0,4\ mm$	$1106\ Nm$	$46,46\ \%$

Now: the chosen motor, has been simulated (like all the others) at a specific and fixed value of $\alpha_{ie} = 46^{\ el\ deg}$, that is the value where the reference motor run at MTPA conditions. This, generally, is not true for the other motors. Therefore it's necessary to carry out a new simulation of the chosen motor with the change of α_{ie} angle. In Fig. 6.9(a) and in Fig. 6.9(b), a section of the motor and the average torque behaviour, at different values of α_{ie}, are reported:
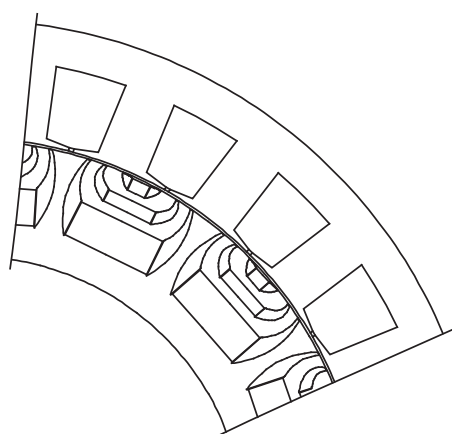
(a) Section of the choosen motor
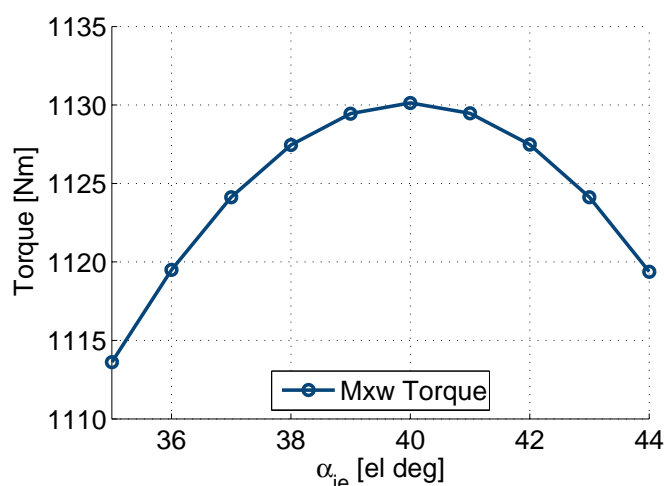
(b) Average Torque at different α_{ie}

Figure 6.9: Choosen optimized motor

As expected, the MTPA condition is no longer where it was fixed during the optimization algorithm ($\alpha_{ie} = 46$ $^{el\ deg}$), but it is $\alpha_{ie} = 40$ $^{el\ deg}$. In these conditions, the average torque and the ripple both increase: from $T_{avg} = 1106Nm$ to $T_{avg} = 1130Nm$ and from $T_{ripple} = 46.46\%$ to $T_{ripple} = 52.40\%$. Fig. 6.10 reports the torque ripple of the motor:
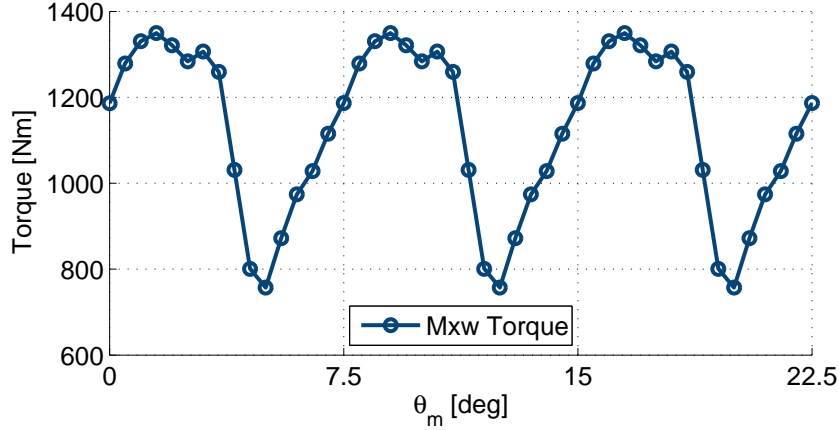

Figure 6.10: Torque ripple for the choosen optimized motor

6.2.1 Barrier refinement

The optimization script includes inside it a set of commands which automatically draw the rotor barriers that have to be generated. The barriers shape must follow as good as possible the trajectory flux lines would have in the case of barriers absence (i.e. their spontaneous path). Unfortunately, this principle applies well only to machines with a low number of poles (up to 4-6 poles). Beyond them, the natural trajectory of flux lines keeps them only on the surface of the rotor: they wouldn't go through the rotor deeply, where the barriers are present.
In order to quickly solve the problem, the automatic-drawing script of rotor barriers acts in two steps:

- Firstly, the code tries to draw a profile of the rotor barrier as similar as possible to the natural trajectory of free flux lines;

- When this shape is no longer possible and a deviation from the natural path is necessary, the code stops and the rotor barrier profile complete itself through a specific analytical trajectory which links the last drown point and the ribs position (fixed by the variables x_2, x_3 e x_4, that are the barrier angles).

The procedure just explained, unfortunately, leads to a very raw design of the barriers, especially around the ribs, where the geometry is rather sharp, as illustrated in Fig. 6.11(a). This profile is not easy to be industrially produced. Therefore, a manual refining procedure is done around the ribs, as in Fig. 6.11(b).

Refinement has besides the advantage of a performance increasing: average torque reaches the value of $T_{avg} = 1135Nm$, while ripple is $T_{ripple} = 51.70\%$. Fig. 6.12 reports the torque ripple of the final (smoothed) motor:
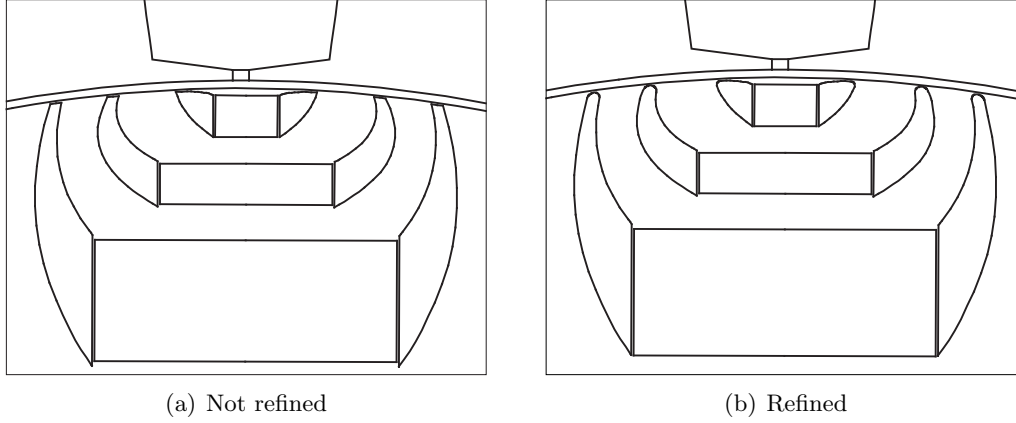
(a) Not refined
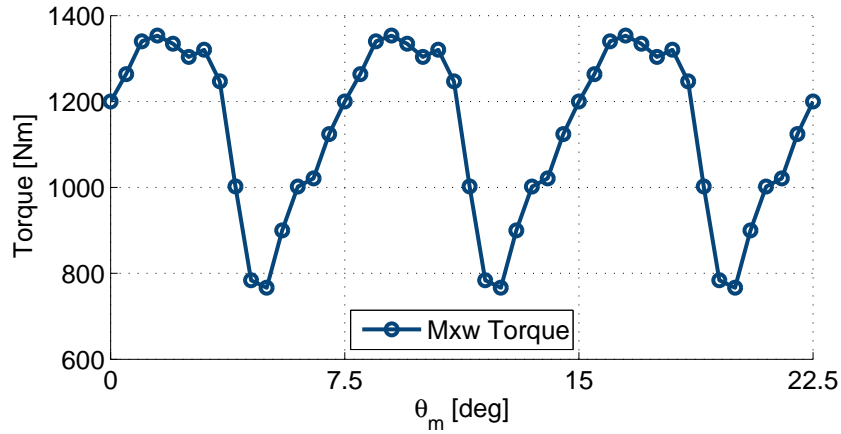
(b) Refined

Figure 6.11: Rotor barriers' profiles

Figure 6.12: Torque ripple for the chosen optimized and refined motor

6.3 Conclusions

Proposed optimization led remarkable achievements in terms of torque ripple reduction. However, the results have always been accompanied by a sensible reduction of the average torque. Two trials were done: a first, random (more or less), optimization and a second one, where some variables have been better calibrated, with respect to the first trial. Due to the better results of the second attempt, only the latter has been taken into account: from it, the (personally) optimum motor has been chosen.

On it, torque values are computed, at different situations ($\alpha_{ie} = 46$ $^{el\ deg}$, MTPA conditions and MTPA conditions with finished barriers), which are reported in Tab. 6.1:

		*ref.	Not Refined		Refined
α_{ie}	[el deg]	46	46	40	40
Minimum	Nm	523	781	757	766
Maximum	Nm	1795	1295	1349	1353
Average Torque	Nm	1306	1106	1130	1135
	%	100	84.69	86.52	86.91
Ripple	%	97.36	46.46	52.40	51.70

Table 6.1: Optimization - Comparison of results

Anyway, chosen motor **must not be considered** the best solution, for several reasons:

1- First of all, because a limit in the number of simulated individuals is set (in the first optimization 10 individuals and 40 generations, making a total of 400 individuals, while in the second optimization they increased up to 500). This limit does not allow the optimization to reach a complete convergence toward the optimum point, also if a good approximation to it is reached, in any case;

2- Secondly, the optimum α_{ie} is only assumed initially, and all the motors are simulated with this same value. It is theoretically wrong, because each motor has got a proper optimal value of such angle. Anyway, after all, an algorithm with the capability to discover also the real optimum α_{ie}, would lead to computational costs extremely high and unbearable;

3- Finally, it is important to remember what has been said previously: from a statistical point of view, the solutions belonging to Pareto front must be considered equipollent and a specific motor can't be defined *better* than the other ones.

Ending, the opportunity is taken to underline a strong limit of the adopted algorithm: as highlighted in Sect. 6.1, each simulated motor is characterized by 14 geometrical variables. It means that the optimization is forced to look for the best solutions in a geometrical $\mathbb{R}^{14}$ space. This fact implies an exponential increase in iterations number, which are necessary to convergence. This problem could be reduced by resorting to a preliminary optimization of the variables, called *Design of experiment*: it consists on a series of random simulations which have the purpose of understanding which variables influence the average torque, which others condition the ripple and -especially- which are those geometrical variables that have no particular weight on these two objectives. In doing so, it could be possible to reduce the number of variables to only those ones which are effectively useful to the scopes of a specific optimization algorithm, and -thus- it could be possible to reduce the computational cost and the simulation time of the optimization.

This chapter ends with the found results, obtained from the developed optimizations. In Tab. 6.2 the Pareto front solutions are reported, with all their specifications. The units of measure are: $[-]$ for $\boldsymbol{x_1}$; $[rad]$ for $\boldsymbol{x_2 \div x_4}$; $[mm]$ for $\boldsymbol{x_2 \div x_{14}}$; $[Nm]$ for **Torque**; $[\%]$ for **Ripple**.

x_1	x_2	x_3	x_4	x_5	x_6	x_7	x_8	x_9	x_{10}	x_{11}	x_{12}	x_{13}	x_{14}	Torque	Ripple
0,51	0,048	0,103	0,157	232,44	12,94	2,82	212,74	19,20	9,65	207,60	43,09	16,87	0,43	1105	70,69
0,54	0,047	0,104	0,156	222,36	11,73	5,19	211,41	20,01	8,40	207,02	41,23	17,99	0,41	1095	68,39
0,50	0,046	0,103	0,153	226,48	11,91	5,08	211,71	19,14	8,05	207,13	42,66	16,25	0,43	1093	65,95
0,50	0,047	0,103	0,155	224,08	12,77	5,74	212,61	18,94	9,70	207,13	43,40	16,25	0,44	1089	62,53
0,47	0,047	0,103	0,153	236,56	13,12	5,73	213,04	18,33	9,91	207,02	44,53	15,13	0,45	1085	60,34
0,47	0,046	0,103	0,151	232,51	12,41	5,26	212,33	18,26	8,35	207,17	44,26	14,65	0,45	1082	58,53
0,45	0,046	0,102	0,151	224,63	12,89	5,64	212,85	17,97	9,10	207,34	44,97	14,25	0,45	1079	57,09
0,49	0,045	0,103	0,148	221,90	10,94	5,39	213,46	18,79	8,35	206,46	42,71	15,05	0,43	1077	55,31
0,43	0,046	0,102	0,150	240,69	13,30	5,66	213,34	17,46	9,56	207,13	45,96	13,39	0,47	1075	54,77
0,52	0,037	0,102	0,146	224,63	10,99	4,76	212,50	17,19	7,42	205,70	40,28	17,03	0,42	1071	54,57
0,46	0,043	0,103	0,144	221,70	10,61	5,27	210,51	18,26	8,33	205,93	43,34	13,80	0,44	1065	54,24
0,40	0,045	0,097	0,147	238,33	15,18	5,14	212,46	19,01	7,43	206,97	45,98	15,14	0,53	1060	53,85
0,42	0,046	0,102	0,149	242,45	13,38	5,63	213,46	17,09	9,41	207,18	46,57	12,65	0,47	1055	50,30
0,36	0,042	0,093	0,145	243,98	13,71	5,32	212,12	16,92	5,05	206,54	45,72	14,94	0,65	1019	48,34
0,37	0,041	0,090	0,146	226,81	13,36	5,19	210,92	21,92	2,88	206,43	43,75	16,81	0,70	1001	45,24
0,42	0,043	0,087	0,144	242,45	14,33	5,21	212,98	21,92	2,88	207,25	40,19	14,25	0,59	995	44,96
0,42	0,042	0,081	0,142	242,45	14,74	5,03	212,77	16,92	2,76	207,28	37,46	14,94	0,64	971	44,24
							First optimization								
0,45	0,052	0,103	0,153	222,21	11,49	4,31	214,86	32,54	8,34	202,17	58,40	22,48	0,45	1129	62,90
0,45	0,049	0,102	0,147	224,79	12,38	6,74	213,70	32,39	8,04	202,65	56,92	21,42	0,41	1117	51,88
0,45	0,050	0,102	0,147	224,56	12,20	6,90	214,62	32,52	7,93	203,22	57,13	22,00	0,41	1115	50,92
0,45	0,051	0,102	0,147	223,28	12,26	7,13	214,48	32,72	7,95	204,26	57,55	23,29	0,41	1113	50,01
0,45	0,051	0,102	0,147	223,84	11,74	7,33	214,80	32,83	7,64	204,85	57,59	23,54	0,41	1112	48,84
0,45	0,050	0,102	0,147	224,09	11,98	7,84	214,45	32,66	7,79	204,18	57,29	22,83	0,41	1108	47,58
0,45	0,050	0,102	0,146	223,81	11,93	7,93	214,62	32,68	7,77	204,61	57,25	23,11	0,41	1106	46,46
0,46	0,038	0,100	0,139	222,22	12,34	7,81	213,06	32,10	7,65	202,74	55,43	22,34	0,56	1064	37,36
							Second optimization								

Table 6.2: Pareto fronts Individuals

66

Chapter 7

Skewing

In this chapter an advanced algorithm for rotor skewing has been developed. Theoretical background, the code and results are illustrated.

7.1 The idea of Skewing

The study of machine is divided in four different phases, as already seen in Sect. 2.1: design, rotor alignment, search of the optimum α_{ie} and under load machine evaluation.
In particular, the rotor alignment -in the used reference frame- has to ensure that the flux linkage space vector, generated by the stator currents, (for instance of A-phase) and PM flux linkage space vector are at a 90-degree angle to each other and, even more specifically, the first one must developed itself along the d axis, while the other one must be along the $-q$ axis. At this point, a question could be the following:

What happens if the motor is not simulated in rotor-alignment conditions?

Surely, the torque developed by the machine would decrease. But it is not enough: the torque behaviour would shift horizontally, as shown in Fig. 7.1, where a generic torque ripple has been taken into account:
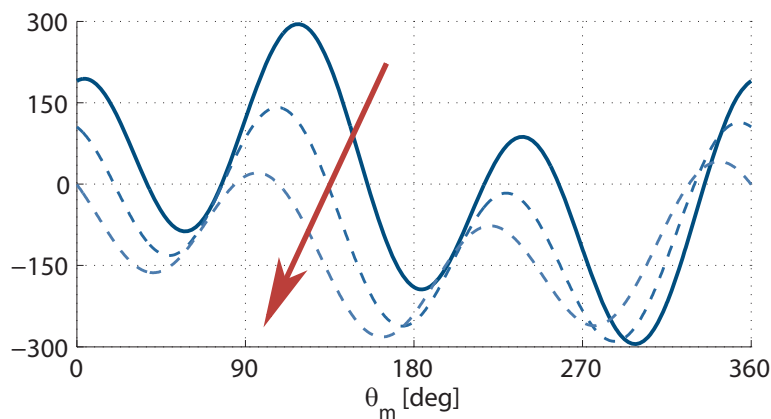
Figure 7.1: Torque ripple trend at different phase conditions

In other words: "to get the machine to work in misalignment conditions" means "to shift the ripple behaviour", besides to reduce the torque values.

7.2 The algoritm

Let's consider the torque ripple of a generic (already simulated) machine. For example, the optimized motor of Sect. 6.2.1. The developed torque is brought back here, in Fig. 7.2:
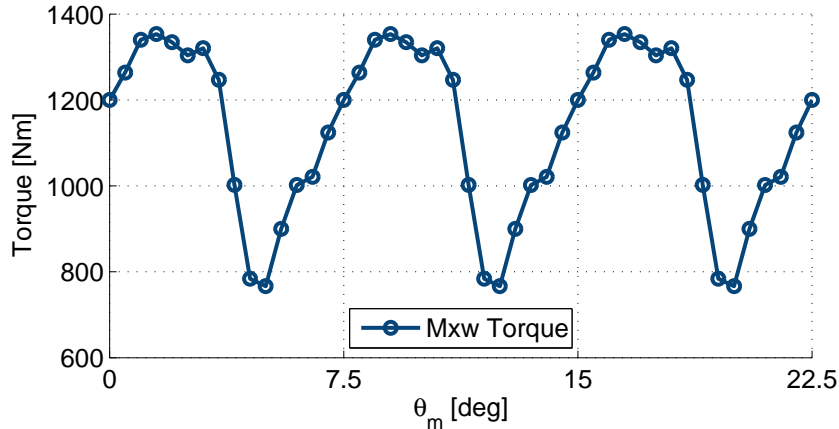

Figure 7.2: Torque ripple of reference 24-16 PMARel motor

A continuous skewing of the rotor (as it occurs with induction motors) is not possible here, because of the presence of PMs, which clearly can't be twisted. It's necessary, then, a discrete skewing. In the performed trials, the rotor has been initially cut into $m = 9$ portions, with steps of $\Delta\theta = 1^{deg}$, making a total of $\Delta\theta_{TOT} = 8^{deg}$ of skewing. In addition, the middle portion corresponds to the machine in aligned-rotor condition. In Fig. 7.3 an idea of skewed machine geometrical appearance is reported:
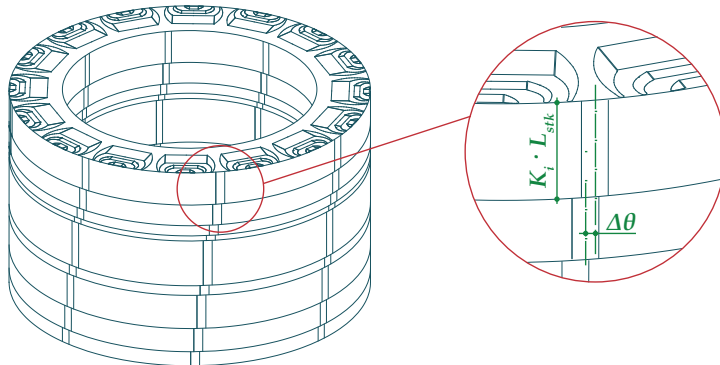
Figure 7.3: Skewing of the rotor

The first step of the algorithm is to simulate the machine with different rotor-alignment conditions. The output consists on a matrix, $OUT(\Delta\theta, \theta_m)$, where all the torque values developed by the machines are reported. This is the only computational cost requested to the calculator.

Once the $OUT(\Delta\theta, \theta_m)$ matrix is created, the aim is to look for all the possible linear combinations of the m torque-ripple behaviours and, between those combinations, to find the more convenient of them. Since the only variable that can be edited in the problem is the length of each rotor portion, $K_i \cdot L_{stk}$, the weighing coefficients correspond to these relative lengths. All the combinations of these coefficients have been created by imposing that:

- the relative length of rotor portion must be a multiple of 0,10. A specific portion, therefore, can be long: the 0%, 10%, 20%, and so on, of the total rotor length, L_{stk};

- the sum of all the coefficients must be equal to 1 (i.e. 100% o L_{stk}).

The overall torque developed in a specific position of the rotor, $T(\theta_m)$, thus, will be:

$$T(\theta_m) = \frac{1}{\sum_i K_i \cdot L_{stk}} \cdot \sum_{i=-4}^{+4} K_i \cdot L_{stk} \cdot T_i(\theta_m) \qquad (7.1)$$

where: $\sum_i K_i = 1$, that is: $\sum_i K_i \cdot L_{stk} = L_{stk}$.

Example 7.2.1. Lets consider the combination: $[0,0 \ \ 0,0 \ \ 0,0 \ \ 0,4 \ \ 0,3 \ \ 0,0 \ \ 0,1 \ \ 0,0 \ \ 0,2]$. The rotor consists of the following portions:

Rotor misaligned of -1^{deg}	$\longrightarrow$	Length: 40% of L_{stk}	$\longrightarrow$	$K_{i=-1} = 0,4$
Rotor perfectly aligned	$\longrightarrow$	Length: 30% of L_{stk}	$\longrightarrow$	$K_{i=0} = 0,3$
Rotor misaligned of $+2^{deg}$	$\longrightarrow$	Length: 10% of L_{stk}	$\longrightarrow$	$K_{i=+2} = 0,1$
Rotor misaligned of $+4^{deg}$	$\longrightarrow$	Length: 20% of L_{stk}	$\longrightarrow$	$K_{i=-1} = 0,2$

The torques developed by each portion of the rotor are shown as dashed lines in Fig. 7.4(a), while the blue and continuous line represents the sum of all the previous ones: it is the overall torque developed by the skewed machine. As clear as in Fig. 7.4(b), torque ripple considerably decreases with respect to the non-skewed machine, by moving itself from $T_{ripple} = 51.70\%$ down to $T'_{ripple} = 25.27\%$. From the average torque point of view, since the torque behaviour has been combined with other lower behaviours, the overall final torque, obviously, will be lower. As a matter of fact, it decreases from $T_{average} = 1135Nm$ down to $T'_{average} = 1008Nm$.
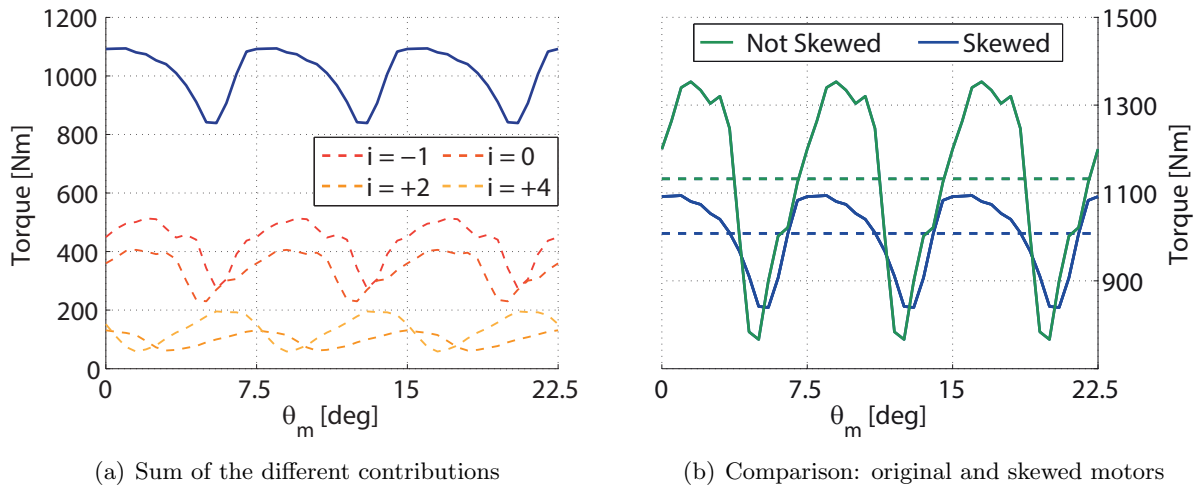

(a) Sum of the different contributions   (b) Comparison: original and skewed motors

Figure 7.4: Rotor skewing example

Skewing can be repeated for any combination of K_i values which respect the criteria described above. Now, all the possible coefficients combinations could be easily found through a permutation of the values. The *perm* function of Matlab® is used. Unfortunately, however, for dimensions of K_i vector greater than 7, the computational weight of *perm* function is too high and a huge quantity of RAM should be necessary.

This is the reason why a trivial, but efficient, algorithm has been implemented. It works like this:

1- A reasonable number, n', of wanted combinations is set;

2- The calculator creates an array of n' unique random combinations, each one characterized by $m = 9$ values of $\mathbb{N}_0^+$;

3- All the combinations whose sum is not equal to 10 are discarded;

4- All the remaining $n \leq n'$ combinations are divided by 10, in order to take their sum back to 1.

In the first executed trial (9 portions of $\Delta\theta = 1^{deg}$, each), $n = 3750$ different permutations has been taken into account.

7.3   Results

Once the analysis illustrated in Ex. 7.2.1 is repeated for all the n known combinations, all the results are reported into a scattering graph, as in Fig. 7.5. Also if this approach is not properly a statistical optimization, and so a Pareto Front can't be properly defined, anyway, the locus of points on the left-bottom side defines the optimal solutions.
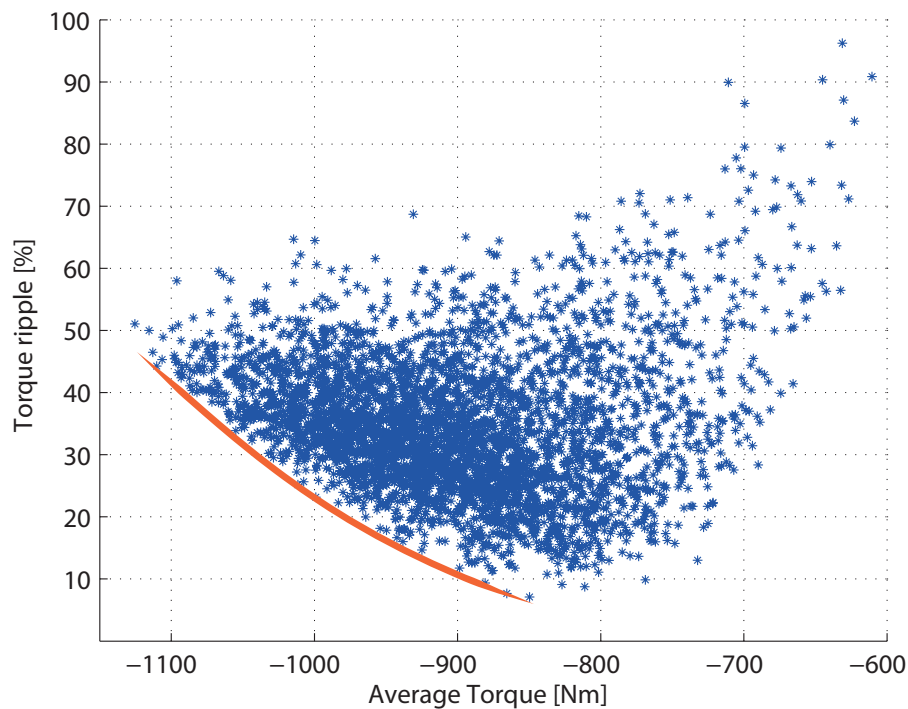
Figure 7.5: Scattering of Skewing

Thanks to rotor skewing, very important results can be reached, from the torque ripple point of view. With respect to the reference 24-16 PMASynRel motor, ripple goes down from $T_{ripple} \approx 100\%$ down to values lower than $T_{ripple} = 10\%$. This occurs, unfortunately, at the expense of the average torque, which -with respect to the reference motor- decreases down to the 65%.

An another comparison can be made with respect to the PMASynRel motor with distributed winding (Motor #1): the solution with minimum ripple ($T_{ripple} \approx 7\%$) had never been reached and it is characterized by a decrease of the average torque around 50%; viceversa, in order to obtain the same values of torque ripple ($T_{ripple} \approx 19\%$), the reduction of average torque is confined to 56%.

7.3.1 Other tests

Results are referred to a specific choice of $\Delta\theta$ (1^{deg}) and $\Delta\theta_{TOT}$ (8^{deg}, i.e. $m = 9$). It is interesting, now, to understand how results could modify themselves, by changing the two variables.

Firstly, the skewing angle, $\Delta\theta = 1^{deg}$, remains unchanged, while the number of portions, m, (and, so, the total angle $\Delta\theta_{TOT}$, too) is modified. In Tab. 7.1, a summary of the executed tests is reported:

		done				
Portions (m)	$[-]$	5	7	9	11	13
Skew Angle ($\Delta\theta$)	$[deg]$	1	1	1	1	1
Total Skew Angle ($\Delta\theta_{TOT}$)	$[deg]$	4	6	8	10	12
Combinations (n)	$[-]$	996	4000	3750	4000	4000

Table 7.1: Other tests - Solutions with different number of portions and the same skew angle

NOTE. The K_i vector of dimension 5 shows all the possible combinations ($n = 996$), while, in the other cases, the number of permutations is too high and, thus, it has been limited to $n = 4000$.

In Fig. 7.6, the graphs relative to the solutions of Tab. 7.1 are reported, while a comparison is carried out in Fig. 7.7.
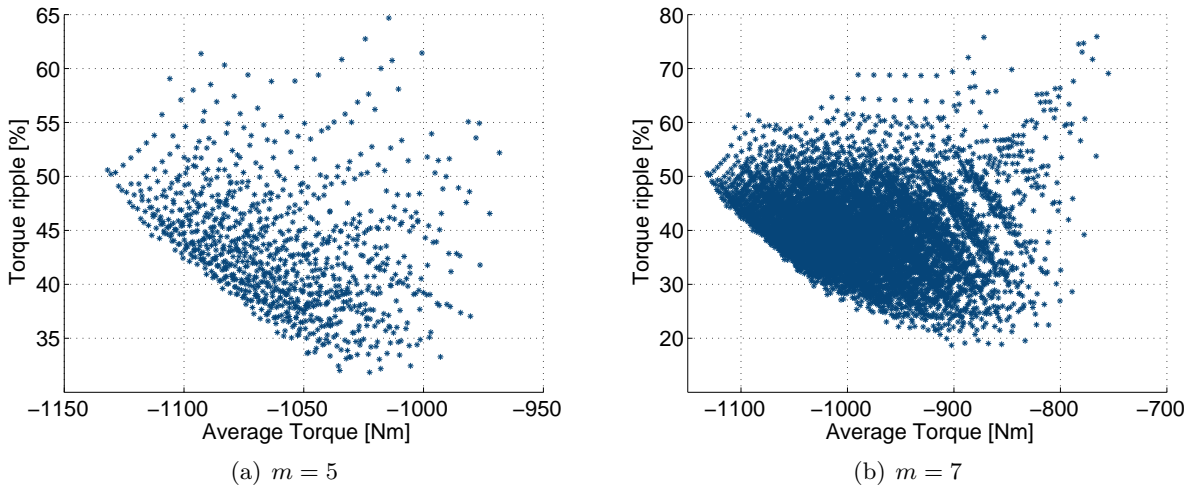

(a) $m = 5$ (b) $m = 7$

Figure 7.6: Tests with different Total Skew Angles, $\Delta\theta_{TOT}$, and the same Skew Angle, $\Delta\theta$.
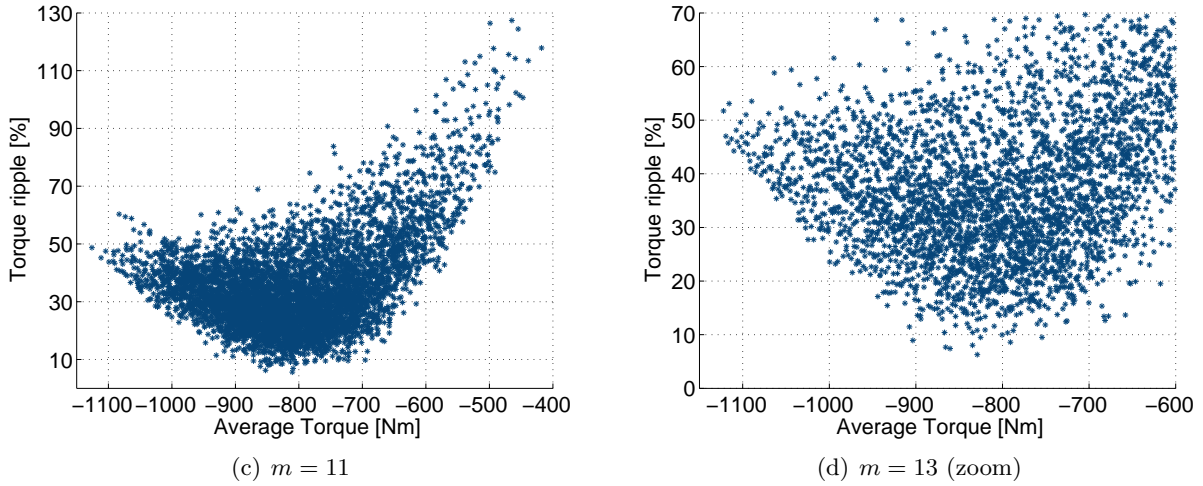
Figure 7.6: Tests with different Total Skew Angles, $\Delta\theta_{TOT}$, and the same Skew Angle, $\Delta\theta$.
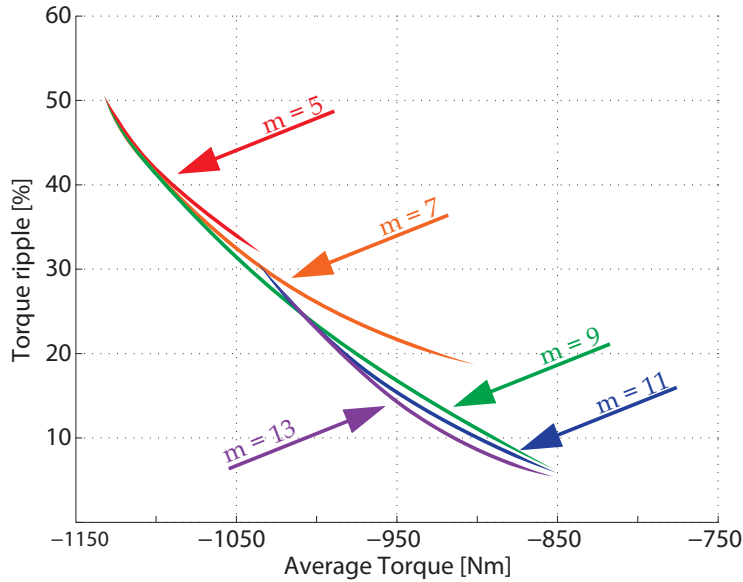

Figure 7.7: Comparison between the different m solutions

From Fig. 7.7 is clear how the implemented skewing, for rotor partitions up to $m = 9$ portions, shows considerable advantages in terms of torque ripple reduction. Viceversa, when m further increases, the trend tends to slow and only a small increase of performances is observed. Hence, it is possible to conclude that skewing is limited into the choice of the number of rotor portions, m. Beyond, the increase of performances is probably no longer significant in order to justify the increase of construction difficulties.

The purpose of the second step is to understand if, having fixed a specific Total Skewing Angle, $\Delta\theta_{TOT}$, the machine performance can increase, by refining or making rough the phase shift angle between two neighbouring portions, $\Delta\theta$.

In Tab. 7.2, improved tests are reported, while in Fig. 7.8 the corresponding results are present.

		done			done		
Total Skew Angle ($\Delta\theta_{TOT}$)	[deg]	6	6	6	8	8	8
Skew Angle ($\Delta\theta$)	[deg]	0.5	1	2	0.5	1	2
Portions (m)	[$-$]	13	7	4	17	9	5
Combinations (n)	[$-$]	996	4000	3750	4000	4000	4000

Table 7.2: Other tests - Solutions with different skew angles

(a) $\Delta\theta_{TOT} = 6^{deg}$ - $\Delta\theta = 0.5^{deg}$

(b) $\Delta\theta_{TOT} = 6^{deg}$ - $\Delta\theta = 2^{deg}$

(c) $\Delta\theta_{TOT} = 8^{deg}$ - $\Delta\theta = 0.5^{deg}$
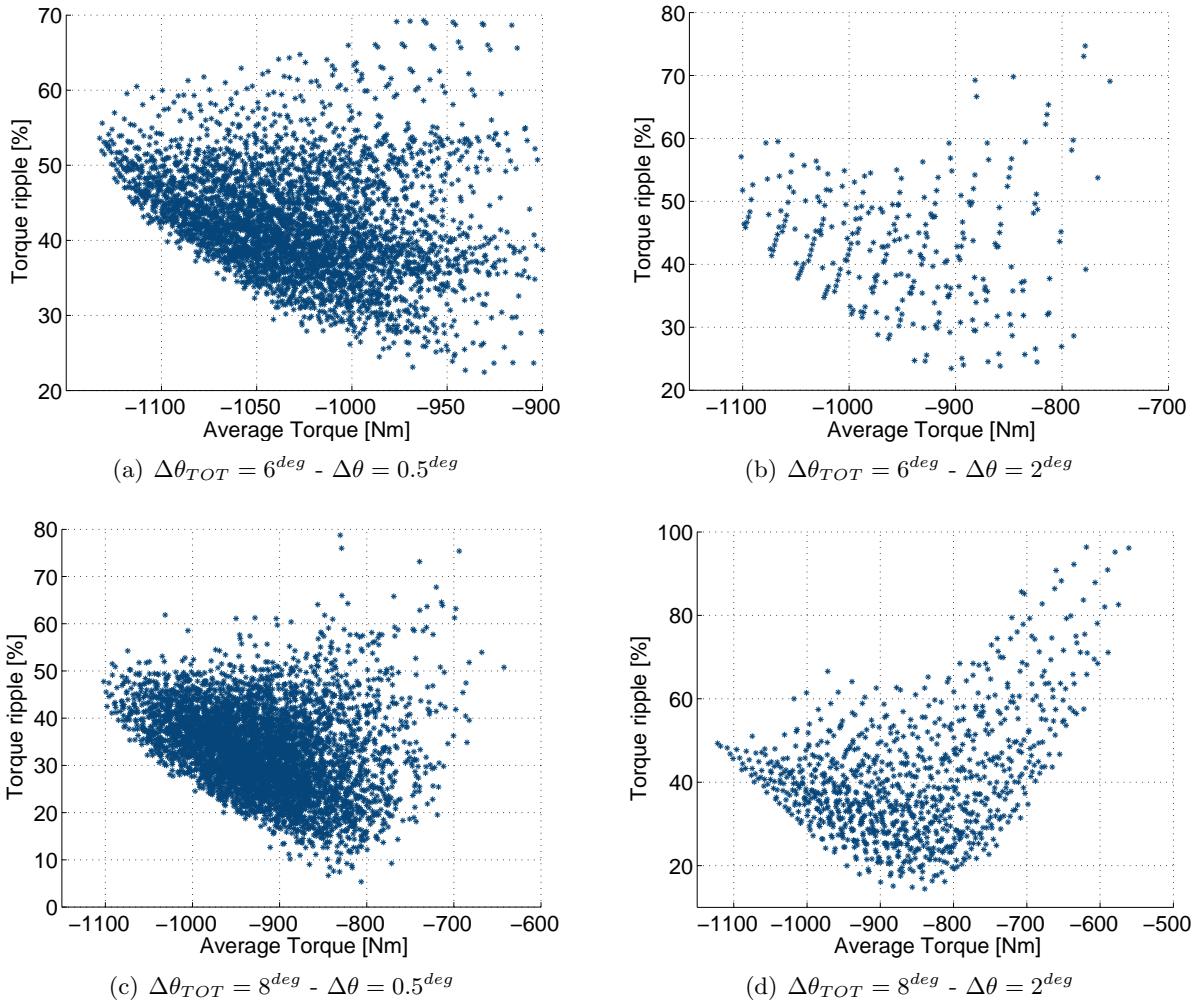
(d) $\Delta\theta_{TOT} = 8^{deg}$ - $\Delta\theta = 2^{deg}$

Figure 7.8: Other tests - Solutions with different skew angles

Finally, Fig. 7.9 shows the comparison between the results, in the case of $\Delta\theta_{TOT} = 6^{deg}$ and $\Delta\theta_{TOT} = 8^{deg}$, separately. Here it is possible to note how the transition from raw angles of $\Delta\theta = 2^{deg}$ to angles $\Delta\theta = 1^{deg}$ involves a significant increase of performance. Viceversa, the attempt of further refining the Skew Angle, up to $\Delta\theta = 0.5^{deg}$, has not been successful, because the increase of performance is zero or, anyway, very low.

(a) $\Delta\theta_{TOT} = 6^{deg}$ (b) $\Delta\theta_{TOT} = 8^{deg}$
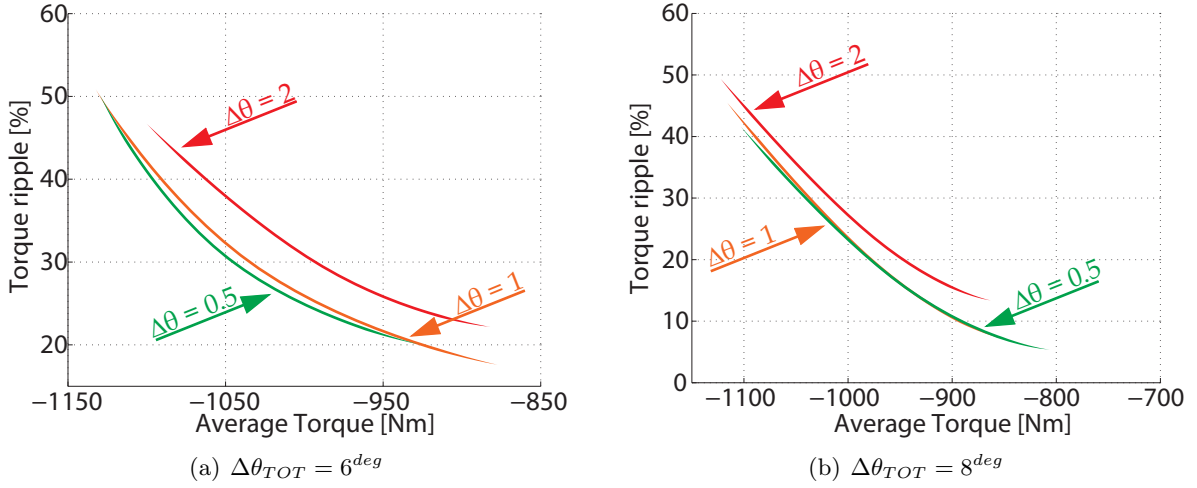
Figure 7.9: Comparison between solution with different $\Delta\theta$

7.4   Remark on the correctness of α_{ie}

The various rotor positions considered by the algorithm have to be firstly simulated through a FE software. All the simulations have been carried out with the same current angle, $\alpha_{ie} = \alpha_{ie,opt}|_0 = 46^{\ el\ deg}$. But this is not generally the correct angle for the generic skewed machine, proposed by the algorithm. This is a limit of the code but, after all, it might not be differently because it is not possible to simulate all the skewed machines, as the current angle, α_{ie}, changes. Fortunately, the computational mistake does not carry weight on the final results, because the difference between the optimal angle and the simulated one is, anyway, low.

Let's consider a permutations of the algorithm. For instance, in the first analysis ($\Delta\theta_{TOT} = 8^{\ deg}$, $\Delta\theta = 1^{\ deg}$, $m = 9$), there is the combination: $[0,0\ \ 0,2\ \ 0,3\ \ 0,1\ \ 0,0\ \ 0,0\ \ 0,1\ \ 0,0\ \ 0,3]$. The optimum current angle related to the generic portion $i - th$ will be:

$$\alpha_{ie,opt}|_i = \alpha_{ie,opt}|_0 - p \cdot i \cdot \Delta\theta = 46^{\ el\ deg} - 8 \cdot i \cdot 1^{\ deg} = \left(46 - 8 \cdot i\right)^{\ el\ deg}$$

where: $\alpha_{ie,opt}|_0 = 46^{\ el\ deg}$ is the current angle used for all the simulations, $p = 8$ are the machine pole-pairs and i is the index which identifies the specific rotor portion.

The true optimal current angles linked to the various portions, then, will be:

i	-4	-3	-2	-1	0	+1	+2	+3	+4
K_i	0,0	0,2	0,3	0,1	0,0	0,0	0,1	0,0	0,3
$\alpha_{ie,opt}|_i$	78	70	62	54	46	38	30	22	14

The optimal current angle for the whole skewed machine is computed as the average of all these angles, weighed by their relative coefficients, K_i:

$$\alpha_{ie,opt} = \frac{1}{\sum_{i=-4}^{+4} K_i} \cdot \sum_{i=-4}^{+4} K_i \cdot \alpha_{ie,opt}|_i$$

74

Hence:

$$\alpha_{ie,opt} = \cancel{0 \cdot 78} + 0,2 \cdot 70 + 0,3 \cdot 62 + 0,1 \cdot 54 + \cancel{0 \cdot 46} + \cancel{0 \cdot 38} + 0,1 \cdot 30 + \cancel{0 \cdot 22} + 0,3 \cdot 14$$
$$= 45 \ ^{el \ deg}$$

As it can be seen, the real $\alpha_{ie,opt}$ is anyway very close to the fixed value and similar results are obtained for any other combination.

In addition, it is highlighted how this error not only is very small, but also in the safety side. In fact, when the current angle is not the optimal one, the average torque decreases. Simultaneously, the peak-to-peak value of torque does not change and, thus, the torque ripple increases. Therefore, results obtained with non-optimal angles will show worse values respect to those ones obtained in the real skewed motor, with the true $\alpha_{ie,opt}$.

7.5 Conclusions

In this chapter a self-made algorithm for rotor skewing is implemented. It has got the peculiarity that the different portions of rotor are not taken, a priori, all with the same length. Conversely, each its portion is linked to a weighing coefficient, K_i, which specifies the relative length of the portion, $K_i \cdot L_{stk}$, with respect to the total length, L_{stk}. The various torque ripples, each associated to a specific condition of misalignment, are then linearly combined with their weighing coefficients. The number of coefficient combinations is high (around 4000 different permutations) in order to explore the space of possibilities, as better as possible.
The obtained results show important improvements in terms of torque ripple decrease, that reaches -finally- very low and acceptable values. Unfortunately, this pulling down of the ripple causes a simultaneous decrease of the average torque.

Since the starting analysis has been carried out with a Total Skew Angle and steps which were defined only on the basis of author's awareness, the chapter has been completed with a study on how the results could change with other values of these two variables.
Firstly, a fixed Skew Angle, $\Delta\theta = 1^{deg}$, has been imposed. Then it has been changed, while the Total Skew Angles, $\Delta\theta_{TOT}$, has been fixed.

In both cases, this is the conclusion: with respect to the first experiment ($\Delta\theta_{TOT} = 8^{deg}$ through 9 misaligned portions, with $\Delta\theta = 1^{deg}$), rawer skewings reduce the performances, while more refined ones do not improve them.
The first experiment, therefore, can be considered a good tradeoff between ripple reduction and industrial simplicity (and so industrial costs). The problem of low average torque, anyway, still remains.

As done in Chap. 6.3, this chapter ends with a summary of the best found results. Only the first skewings of Fig. 7.5 are considered. In addition, amongst all the possible solutions, only points which define the "Pareto front" are reported.

| Combinations | | | | | | | | | Torque | Ripple | True $\alpha_{ie,opt}$ |
			[−]						[Nm]	[%]	[el deg]
0,0	0,0	0,0	0,0	0,7	0,3	0,0	0,0	0,0	1125	51,04	44
0,0	0,0	0,0	0,2	0,4	0,4	0,0	0,0	0,0	1113	46,50	44
0,0	0,0	0,0	0,4	0,4	0,2	0,0	0,0	0,0	1110	44,26	48
0,0	0,0	0,0	0,3	0,2	0,4	0,1	0,0	0,0	1095	43,21	44
0,0	0,0	0,1	0,4	0,3	0,2	0,0	0,0	0,0	1093	42,38	49
0,0	0,0	0,0	0,3	0,4	0,2	0,0	0,1	0,0	1087	41,07	44
0,0	0,0	0,2	0,2	0,4	0,2	0,0	0,0	0,0	1085	40,32	49
0,0	0,0	0,2	0,2	0,3	0,3	0,0	0,0	0,0	1082	40,04	48
0,0	0,0	0,1	0,3	0,2	0,2	0,2	0,0	0,0	1072	38,51	45
0,0	0,0	0,0	0,2	0,5	0,1	0,0	0,2	0,0	1067	38,40	42
0,0	0,0	0,0	0,2	0,2	0,5	0,0	0,0	0,1	1064	38,10	40
0,0	0,0	0,0	0,3	0,4	0,1	0,1	0,0	0,1	1059	35,58	43
0,0	0,0	0,1	0,3	0,4	0,1	0,0	0,0	0,1	1055	33,88	46
0,0	0,0	0,3	0,2	0,3	0,1	0,0	0,1	0,0	1044	32,31	49
0,0	0,0	0,1	0,3	0,3	0,0	0,2	0,0	0,1	1032	30,22	44
0,0	0,0	0,3	0,2	0,4	0,0	0,0	0,0	0,1	1029	29,51	49
0,0	0,0	0,3	0,2	0,2	0,2	0,0	0,0	0,1	1022	28,94	48
0,0	0,0	0,0	0,4	0,3	0,0	0,1	0,0	0,2	1012	25,18	41
0,0	0,0	0,1	0,3	0,3	0,0	0,1	0,0	0,2	999	23,17	42
0,0	0,0	0,2	0,2	0,2	0,1	0,1	0,0	0,2	983	22,27	42
0,0	0,0	0,1	0,2	0,2	0,2	0,0	0,0	0,3	964	19,97	38
0,0	0,0	0,2	0,3	0,1	0,0	0,1	0,1	0,2	954	18,16	41
0,0	0,0	0,1	0,3	0,1	0,1	0,1	0,0	0,3	950	17,85	38
0,0	0,0	0,2	0,3	0,0	0,2	0,0	0,0	0,3	942	16,66	40
0,0	0,0	0,1	0,3	0,2	0,0	0,0	0,1	0,3	938	16,00	38
0,0	0,1	0,1	0,2	0,1	0,2	0,0	0,0	0,3	925	14,68	40
0,0	0,1	0,3	0,1	0,1	0,1	0,0	0,0	0,3	899	11,77	44
0,0	0,1	0,1	0,3	0,1	0,0	0,0	0,0	0,4	881	9,35	40
0,0	0,2	0,2	0,2	0,0	0,0	0,0	0,2	0,2	866	7,67	44
0,0	0,2	0,3	0,1	0,0	0,0	0,1	0,0	0,3	850	7,11	45

Table 7.3: Rotor Skewing - Better (Pareto Front) points for $\Delta\theta_{TOT} = 8^{deg}$, $\Delta\theta = 1^{deg}$, $m = 9$

Chapter 8

Deep Analysis on 24/16 PMASynRel motor

8.1 Flux density field behaviour

A deeper analysis of the 24/16 PMASynRel motor is carried out in this chapter. Results obtained from the seminumerical approach, developed by *Spargo et al.* [6] and explained in Sect. 3.3, are the starting point of these analysis.

A particular question rose during all the simulations. It is: "How is it possible to obtain a sixth harmonic of torque ripple from a second spatial harmonic of flux density?". To answer the question, the results and the meaning of *Spargo* theory have been taken into account. In the algorithm, torque is defined as:

$$T(\theta_m) = \frac{r^2}{\mu_0} \cdot \int_0^{l_{stk}} \int_0^{2\pi} B_n(\xi, \theta_m) \cdot B_t(\xi, \theta_m) \cdot d\xi \tag{8.1}$$

where: r is the radius at the air-gap, μ_0 is the vacuum magnetic permeability, while $B_n(\xi, \theta_m)$ and $B_t(\xi, \theta_m)$ are the radial and tangential components of the flux density distribution at the gap, along the spatial variable, ξ, and for the specific rotor position θ_m.

From the simulated motor, the $B_n(\xi, \theta_m)$ and $B_t(\xi, \theta_m)$ values are knows along all the coordinate ξ and for all the rotor positions, from $\theta_m = 0$ ^{deg} to $\theta_m = 45$ ^{deg}. The product $B_{n,2}(\xi, \theta_m) \cdot B_{t,2}(\xi, \theta_m)$, as the two variables change, has been reconstructed, consequently.
The behaviour of this product is characterized by the sum of:

- a sinusoidal wave, with a wavelength $\lambda = \dfrac{360}{4} = 90$ $^{el\ deg}$ and an angular speed $\omega' = -\dfrac{\omega}{2}$;

- an another unknown wave, which produces a light amplitude modulation of the previous wave;

- an average value, which oscillates with an angular speed $\omega'' = 6\omega$.

In Fig. 8.1 the function $B_n(\xi, \theta_m) \cdot B_t(\xi, \theta_m)$ is reported, as the spatial coordinate, ξ, changes and for four different rotor positions (i.e. time instants), while in Fig. 8.2 the maxs and the mins of the same function are highlighted for all the simulated θ_m angles:
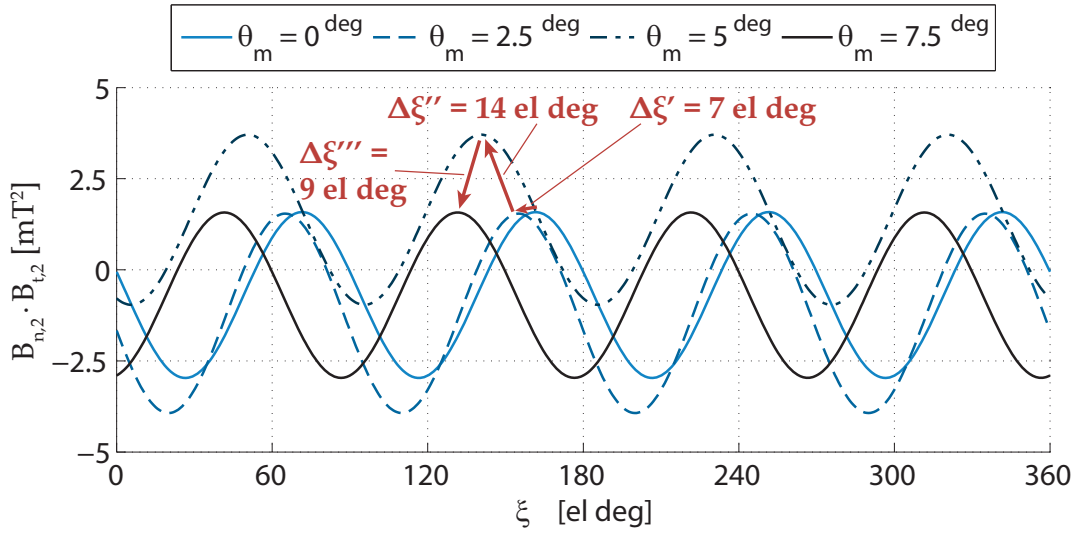
Figure 8.1: $B_n(\xi, \theta_m) \cdot B_t(\xi, \theta_m)$ product at different rotor positions
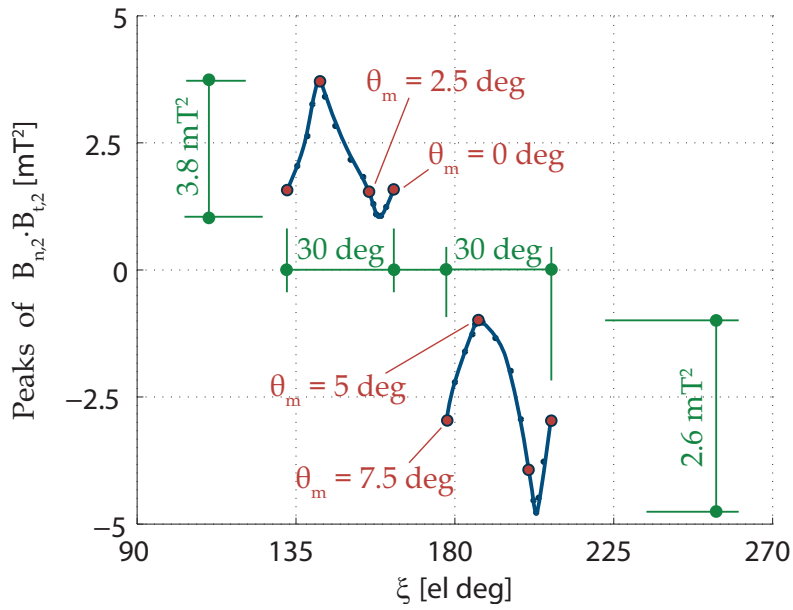
Figure 8.2: mins and maxs of the function (relative to one period)

8.2 Analytical model of the motor

What has just been seen is a set of theoretical considerations that refer to numerical results, obtained from the FEM analysis. The purpose, now, is to develop an analytical model of the motor and to justify, thus, the behaviours seen in the figures above.

The motor model is developed starting from those ones of *Liwschitz-Garik et Whipple*, presented in [7], and of *Bianchi et al.*, presented in [8].

In a stationary reference frame, torque can be defined as:

$$T = \frac{D^2 L}{4} \cdot \int_0^{2\pi} K_s(\xi) \cdot B(\xi) \cdot d\xi \tag{8.2}$$

where: D and L are the diameter at the air-gap and the stack length, respectively, $K_s(\xi)$ is the electric loading distribution at the inner diameter of the stator, while $B(\xi)$ is the air-gap flux density distribution.

By its definition, the electric loading is the sum of its harmonics, ν:

$$K_s(\xi) = \sum_{\nu} \hat{K}_\nu \cdot sin(\omega t - \nu \xi) \tag{8.3}$$

Generally, for distributed windings, it is:

$$\nu = 6 \cdot k \pm 1 \tag{8.4}$$

It is no more true, instead, for fractional slots machines, where the harmonic content is more irregular [3].

The scalar magnetic potential is derived by the electric loading, as:

$$\begin{aligned} U_s(\xi) &= \frac{D}{2} \cdot \int K_s(\xi) \cdot d\xi = \frac{D}{2} \cdot \sum_{\nu} \int \hat{K}_\nu \cdot sin(\omega t - \nu \xi) \cdot d\xi \\ &= \frac{D}{2} \cdot \sum_{\nu} \left(\frac{\hat{K}_\nu}{\nu} \cdot cos(\omega t - \nu \xi) \right) \end{aligned} \tag{8.5}$$

The magnetic potential, $U_s(\xi)$, then, interacts with the machine reluctance, $G(\xi)$, or -similarly- with the permeance function, $P(\xi)$. Permeance is strictly linked to the rotor geometry: it is a function which moves synchronously (i.e. $\omega' = \omega$) with the rotor and shows a double number of periods (i.e. $\lambda = \pi$ $^{el\ rad}$). Therefore, it can be written as:

$$P(\xi) = \sum_{\zeta} \hat{P}_\zeta \cdot cos[2\zeta \cdot (\omega t - \xi)] \tag{8.6}$$

The relationship which links flux density, magnetic potential and permeance is [1] [2]

$$\begin{aligned} B(\xi) &= \frac{U_s(\xi)}{G(\xi)} = U_s(\xi) \cdot P(\xi) \\ &= \left[\frac{D}{2} \cdot \sum_{\nu'} \frac{\hat{K}_{\nu'}}{\nu'} \cdot cos(\omega t - \nu' \xi) \right] \cdot \left[\sum_{\zeta} \hat{P}_\zeta \cdot cos[2\zeta \cdot (\omega t - \xi)] \right] \\ &= \frac{D}{2} \cdot \sum_{\nu'} \sum_{\zeta} \frac{\hat{K}_{\nu'}}{\nu'} \cdot \hat{P}_\zeta \cdot \underbrace{\left[cos(\omega t - \nu' \xi) \cdot cos[2\zeta \cdot (\omega t - \xi)] \right]}_{\textcircled{A}} \end{aligned} \tag{8.7}$$

---

[1]If the machine is characterized only by a constant gap, without barriers, the permeance function becomes simply: $P(\xi) = \frac{\mu_0 \cdot A}{g}$, where: A is a cross section area.

[2]In order to distinguish the harmonic orders of the electric loading into the torque expression and of the electric loading into the flux density formula, an apex is added in the latter.

where:

$$
\begin{aligned}
ⓐ &= cos(\omega t - \nu'\xi) \cdot cos[2\zeta \cdot (\omega t - \xi)] \\
&= cos(\omega t - \nu'\xi + 2\zeta\omega t - 2\zeta\xi) + cos(\omega t - \nu'\xi - 2\zeta\omega t + 2\zeta\xi) \\
&= cos\left[\omega t \cdot (1 + 2\zeta) - \xi \cdot (\nu' + 2\zeta)\right] + cos\left[\omega t \cdot (1 - 2\zeta) + \xi \cdot (-\nu' + 2\zeta)\right]
\end{aligned} \tag{8.8}
$$

Hence, (8.2) becomes:

$$
\begin{aligned}
T &= \frac{D^2 L}{4} \cdot \int_0^{2\pi} K_s(\xi) \cdot B(\xi) \cdot d\xi \\
&= \frac{D^3 L}{8} \cdot \int_0^{2\pi} \sum_\nu \hat{K}_\nu \cdot sin(\omega t - \nu\xi) \cdot \sum_{\nu'} \frac{\hat{K}_{\nu'}}{\nu'} \cdot cos(\omega t - \nu'\xi) \cdot \sum_\zeta \hat{P}_\zeta \cdot cos[2\zeta \cdot (\omega t - \xi)] \\
&= \frac{D^3 L}{8} \cdot \int_0^{2\pi} \sum_\nu \sum_{\nu'} \sum_\zeta \hat{K}_\nu \cdot \frac{\hat{K}_{\nu'}}{\nu'} \cdot \hat{P}_\zeta \cdot \underbrace{\left(sin(\omega t - \nu\xi) \cdot cos(\omega t - \nu'\xi) \cdot cos[2\zeta \cdot (\omega t - \xi)]\right)}_{ⓑ}
\end{aligned} \tag{8.9}
$$

where:

$$
\begin{aligned}
ⓑ &= sin(\omega t - \nu\xi) \cdot cos(\omega t - \nu'\xi) \cdot cos[2\zeta \cdot (\omega t - \xi)] \\
&= \frac{1}{2} \cdot \left[sin(\omega t - \nu\xi + \omega t - \nu'\xi) + sin(\omega t - \nu\xi - \omega t + \nu'\xi)\right] \cdot cos[2\zeta \cdot (\omega t - \xi)] \\
&= \frac{1}{2} \cdot \left[sin\left(2\omega t - \xi \cdot (\nu' + \nu)\right) + sin\left(\xi \cdot (\nu' - \nu)\right)\right] \cdot cos[2\zeta \cdot (\omega t - \xi)] \\
&= \frac{1}{2} \cdot \left[sin\left(2\omega t - \xi \cdot (\nu' + \nu)\right) \cdot cos[2\zeta(\omega t - \xi)]\right] + \frac{1}{2} \cdot \left[sin\left(\xi \cdot (\nu' - \nu)\right) \cdot cos[2\zeta(\omega t - \xi)]\right] \\
&= \frac{1}{4} \cdot \left[sin\left(2\omega t \cdot (1 + \zeta) - \xi \cdot (\nu' + \nu + 1)\right) + sin\left(2\omega t \cdot (1 - \zeta) - \xi \cdot (\nu' + \nu - 1)\right)\right] + \\
&\quad + \frac{1}{4} \cdot \left[sin\left(2\zeta\omega t + \xi \cdot (\nu' - \nu - 1)\right) + sin\left(-2\zeta\omega t + \xi \cdot (\nu' - \nu + 1)\right)\right]
\end{aligned} \tag{8.10}
$$

Thus:

$$
ⓑ = \frac{1}{4} \cdot \overbrace{sin\left(2\omega t \cdot (1 + \zeta) - \xi \cdot (\nu' + \nu + 1)\right)}^{ⓑ_1} + \frac{1}{4} \cdot \overbrace{sin\left(2\omega t \cdot (1 - \zeta) - \xi \cdot (\nu' + \nu - 1)\right)}^{ⓑ_2} +
$$
$$
+ \frac{1}{4} \cdot \underbrace{sin\left(2\zeta\omega t + \xi \cdot (\nu' - \nu - 1)\right)}_{ⓑ_3} + \frac{1}{4} \cdot \underbrace{sin\left(-2\zeta\omega t + \xi \cdot (\nu' - \nu + 1)\right)}_{ⓑ_4} \tag{8.11}
$$

A plausible harmonic interaction which can justify a sixth harmonic of torque ripple is those one between a second spatial harmonic of electric loading, $K_{s,-2}(\xi)$, the second harmonic of

magnetic potential, $U_{s,-2}$, and a second harmonic of permeance function, $P_2(\xi)$. Remembering that the second order field is counter-rotating respect to the fundamental one, it is:

$$\begin{cases} K_{s,-2}(\xi) = \hat{K}_{-2} \cdot sin(\omega t + 2\xi) \\ U_{s,-2}(\xi) = \dfrac{D}{2} \cdot \dfrac{\hat{K}_{-2}}{-2} \cdot cos(\omega t + 2\xi) \\ P_2(\xi) = \hat{P}_2 \cdot cos[4 \cdot (\omega t - \xi)] \end{cases} \tag{8.12}$$

Therefore:

$$\begin{aligned} B_\beta(\xi) &= \overbrace{\dfrac{D}{2} \cdot \dfrac{\hat{K}_{-2}}{-2} \cdot \hat{P}_\zeta}^{\hat{B}_\beta} \cdot \left[cos(\omega t + 2\xi) \cdot cos[4 \cdot (\omega t - \xi)] \right] \\ &= \underbrace{\hat{B}_{-2} \cdot cos(5\omega t - 2\xi)}_{B_{-2}(\xi)} + \hat{B}_6 \cdot cos(-3\omega t + 6\xi) \end{aligned} \tag{8.13}$$

where: $\hat{B}_{-2} = \hat{B}_6 = \dfrac{1}{2} \cdot \hat{B}_\beta$.

The second addend is not important because it does not produce a second harmonic flux density field (it defines a spatial harmonic of sixth order). Viceversa, the first addend is exactly the harmonic field we are looking for. Hereafter, then, only this first term is considered.
This one, by interacting again with the second harmonic of electric loading, produces a torque:

$$\begin{aligned} T_\tau &= \dfrac{D^2 L}{4} \cdot \int_0^{2\pi} K_{s,-2}(\xi) \cdot B_{-2}(\xi) \cdot d\xi \\ &= \dfrac{D^2 L}{4} \cdot \int_0^{2\pi} \hat{K}_{-2} \cdot \hat{B}_{-2} \cdot \left(sin(\omega t + 2\xi) \cdot cos(5\omega t - 2\xi) \right) \cdot d\xi \\ &= C \cdot \int_0^{2\pi} sin(\omega t + 2\xi) \cdot cos(5\omega t - 2\xi) \cdot d\xi \\ &= \left(\dfrac{C}{2} \cdot \int_0^{2\pi} sin(6\omega t) \cdot d\xi \right) + \left(\dfrac{C}{2} \cdot \cancel{\int_0^{2\pi} sin(-4\omega t + 4\xi) \cdot d\xi} \right) \\ &= \dfrac{C}{2} \cdot sin(6\omega t) \cdot \int_0^{2\pi} d\xi = \dfrac{C}{\cancel{2}} \cdot sin(6\omega t) \cdot \cancel{2}\pi = \pi \cdot C \cdot sin(6\omega t) \end{aligned} \tag{8.14}$$

In (8.14) two waves are identified:

- $sin(-4\omega t + 4\xi)$. It is a sinusoid of wavelength $\lambda = \pi/2$ $^{el\ rad}$, which moves synchronously (i.e with an angular speed $\omega' = \omega$). This field does not produce any torque contribution. Anyway it is worth of noticing because is is exactly the wave, cited above and recognizable in Fig. 8.1, which produces the amplitude modulation of the product $B_{n,2}(\xi) \cdot B_{t,2}(\xi)$;

- $sin(6\omega t)$. It is the average oscillating value of Fig. 8.1. Because it is not a function of variable ξ, its integral is different from zero. This implies that this particular term produces a torque ripple of sixth harmonic.

Definitively, the analytical model justifies the presence of a sixth harmonic torque ripple in the machine. It is due to the interaction between the second spatial harmonic of electric loading (ν and $\nu' = -2$) and a second harmonic of permeance function ($\zeta = 2$). This interaction, as well as explaining the ripple, allows to recognize also the field $sin(-4\omega + 4\xi)$, which was found,

thanks to the *Spargo* method, in Fig. 8.1.

In the same figure, however, a third field was visible. It is due to a second interaction, between the second spatial harmonic of electric loading (ν and $\nu' = -2$) and the harmonic zero of permeance ($\zeta = 0$):

$$
\begin{aligned}
T_\tau &= \frac{D^2 L}{4} \cdot \int_0^{2\pi} K_{s,-2}(\xi) \cdot B_\beta(\xi) \cdot d\xi = \frac{D^2 L}{4} \cdot \int_0^{2\pi} K_{s,-2}(\xi) \cdot U_{s,-2}(\xi) \cdot P_0(\xi) \cdot d\xi \\
&= \frac{D^2 L}{4} \cdot \int_0^{2\pi} \hat{K}_{-2} \cdot sin(\omega t + 2\xi) \cdot \frac{D}{2} \cdot \frac{\hat{K}_{-2}}{-2} \cdot cos(\omega t + 2\xi) \cdot \cancel{cos(0)} \cdot d\xi \\
&= C' \cdot int_0^{2\pi} sin(\omega t + 2\xi) \cdot cos(\omega t + 2\xi) \cdot d\xi \\
&= \frac{C'}{2} \cdot \int_0^{2\pi} sin(2\omega t + 4\xi) + \cancel{sin(0)} \cdot d\xi = \frac{C'}{2} \cdot \int_0^{2\pi} sin(2\omega t + 4\xi) \cdot d\xi = 0
\end{aligned} \tag{8.15}
$$

The contribution, in terms of torque, is null. But from the combination $\nu' = -2$, $\nu = -2$ e $\zeta = 0$, a wave which has equation: $sin(2\omega t + 4\xi)$, is obtained. This is exactly the third component of Fig. 8.1.

8.3 Verifications

The analytical model justifies the $6 - th$ torque ripple the motor shows, by supposing the presence of:

- a $2 - th$ spatial harmonic of electrical loading, $K_\nu(\xi)$;

- a $2 - th$ harmonic of permeance, $P_\zeta(\xi)$

The model, however, only identifies these harmonics, but does not verifies if they are actually present. It is necessary, then, to verify what is assumed by the model.

Firstly, the electric loading distribution is evaluated, by means of a FEM software. A linear 24/16 PMASynRel motor has been taken into account and, here, the rotor has been substituted by a full cylinder of ferromagnetic linear material. In this way, it is:

$$
B(\xi) = \mu_0 \cdot \frac{U_s(\xi) - U_r(\xi)}{g} \tag{8.16}
$$

where: $B(\xi)$ and $U_s(\xi) - U_r(\xi)$ are the already cited flux density and magnetic voltage drop at the gap, while g is the gap length.

By evaluating, therefore, the flux density at the gap, the magnetic voltage drop distribution, $U_s(\xi) - U_r(\xi)$, can be obtained and consequently the electric loading, $K_s(\xi)$, too, for (8.5). In Fig. 8.3(a) the $U_s(\xi) - U_r(\xi)$ distribution is reported along an electrical period[3]. It is highlighted with a continuous blue line, while the red dashed path represents the sum of first and second harmonic of the same distribution. In Fig. 8.3(b), the harmonic content of the first figure is reported:

---

[3]In figure, "MMF" is used instead of "magnetic voltage drop". This term, also if strictly speaking wrong, has been chosen to follow the international conventions.

(a) Air-Gap MMF distribution

(b) Air-Gap MMF Harmonic content
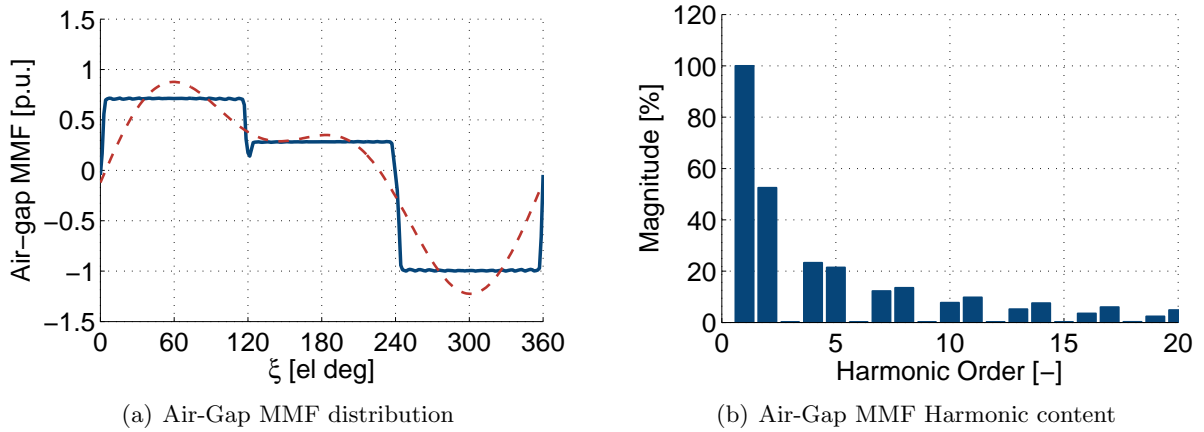
Figure 8.3: 24/16 PMASynRel Air-Gap MMF

The figures above show that there is a clear second harmonic of the magnetic voltage drop at the air-gap (and so of the electric loading, too). This fact verifies the analytical model, in part.

Concerning, then, the permeance harmonics, $P_\zeta(\xi)$, the verification can be summarized as follow:

- a single two-pole pitch of the rotor is taken into account;

- the stator inner diameter is substituted by a segmented line of 100 traits of length $\partial l = D/2 \cdot \partial \xi = 250 \cdot \dfrac{\pi}{4 \cdot 100} \approx 1.96mm$, each;

- the materials are fixed: linear iron instead of Terni, saturated iron for the ribs and air instead of the PMs;

- the following boundary conditions are set:
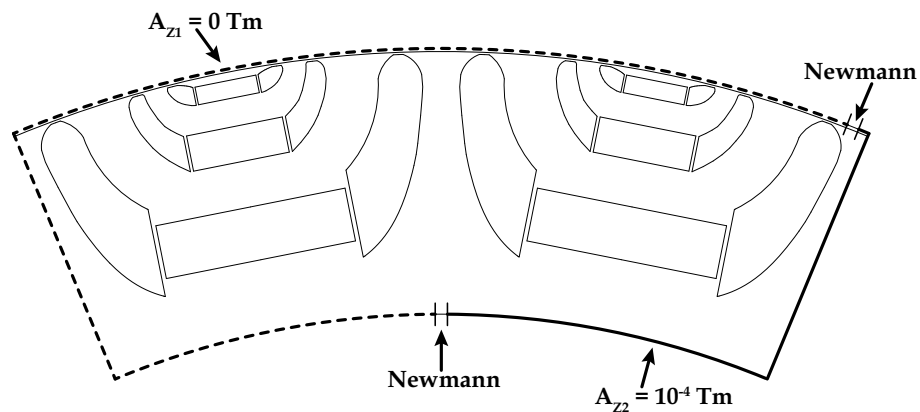
- The magnetic voltage drop is computed along an average path, γ, as highlighted in figure with a red dashed line:
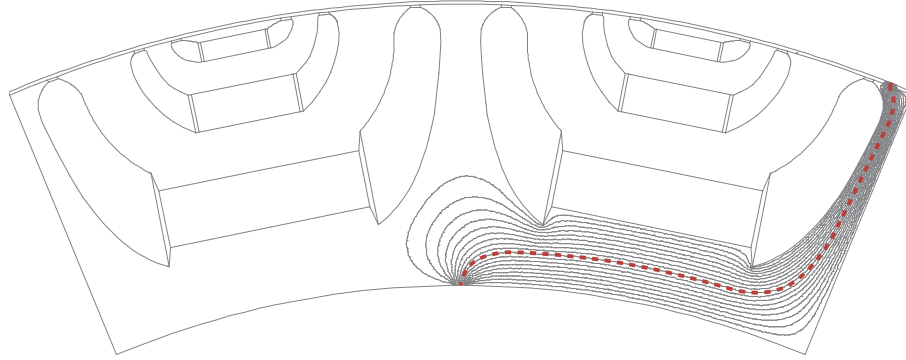
By fixing the Newmann condition to each of the upper traits, ∂l, the permeance function can be graphed. As a matter of facts:

$$\partial P(\xi) = \left. \frac{\partial \Phi}{U} \right|_{\partial l} = \left. \frac{(A_{Z2} - A_{Z1}) \cdot L_{stk}}{\int_\gamma H \cdot t \cdot dt} \right| \tag{8.17}$$

Fig. 8.4 shows the permeance function, $P(\xi)$, and its harmonic content. Also if rather low, the second harmonic assumed in the model is actually present. And this fact further corroborates the analytical model.

(a) Permeance function

(b) Harmonic content
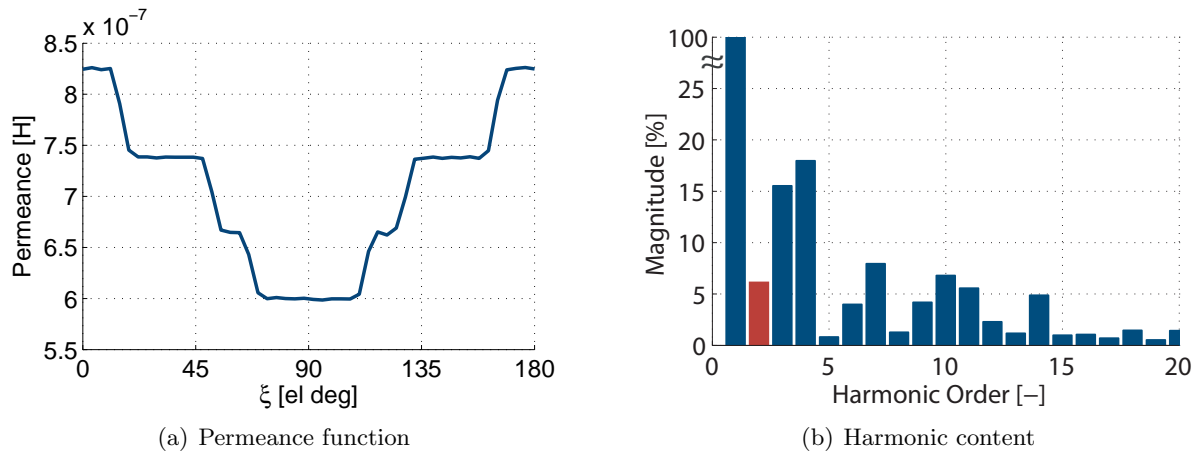
Figure 8.4: 24/16 PMASynRel Permeance function

8.4   Conclusions

In this chapter, a deep analysis of the 24/16 PMASynRel machine is carried out. Starting from the analyses of the previous chapters, a characteristic peculiarity of this motor has been noted: the main torque ripple contribution seems to be due to the presence of a second harmonic of flux density field at the air-gap. Therefore, the product $B_n(\xi) \cdot B_t(\xi)$ has been graphed, as both the spatial variable, ξ, and time change. The product, whose integral identifies the torque, is the sum of three different contributions.

An analytical model of the motor has been developed, consequently, in order to clarify these three contributions. These ones can be explained if two particular interactions between the fields is considered: the second spatial harmonics of electric loading and magnetic potential with the second harmonic of permeance function, firstly, and the same physical quantities but with the harmonic zero of the permeance, then. The first combination, in particular, justifies the $6 - th$ harmonic of torque.

The model, then, is verified. Through a FEM software, the mmf distribution (i.e. the voltage magnetic drop distribution at the gap) is computed. It is proportional to the electric loading, and the presence of a second harmonic of mmf confirms the presence of the same harmonic also of the latter. Secondly, the permeance function has been derived. Here, too, a second harmonic is present, also if its magnitude is rather limited.

The verification, hence, corroborates the assumptions of the analytical model. It is possible, then, to confirm that the main torque ripple contribution is due to the particular interaction:

$$T_{\tau=6} \propto \int_0^{2\pi} K_{\nu=-2}(\xi) \cdot B_{\beta=-2}(\xi) \cdot d\xi = \int_0^{2\pi} K_{\nu=-2}(\xi) \cdot K_{\nu'=-2}(\xi) \cdot P_{\zeta=2}(\xi) \cdot d\xi$$

Chapter 9

Conclusions

This thesis deals with a particular configuration of 24-Slot and 16-Pole Synchronous Reluctance Motor Assisted by Permanent Magnets (PMASynRel). The work is inserted into the research activity of University of Padua's Electrical Drives Laboratory and it is integral part of a research project commissioned by ABB Italia S.p.a. - Discrete Automation and Motion Division.

At first, a brief recall on Synchronous Reluctance machines is presented, in Chapter 1.
Starting from an already designed PMASynRel motor with distributed windings, some configurations of fractional slots motors with non-overlapped coils have been developed. In particular: a 18-Slot and 16-Pole, a 21-Slot and 16-Pole, a 24-Slot and 16-Pole. All the motors have been taken into account without changing the main geometrical data and with the same electric loading, for a better comparison.
Simulations highlighted how the 24/16 configuration is characterized by rather limited performance, in terms of torque ripple. This is the reason why only this latter configuration has been studied, further.

A first analysis of the motor has been carried out in order to understand the torque behaviour. By means of a Finite Element analysis, considerations have been done on the field maps which characterize the machine in some particular magnetic situations.
In addition, torque behaviour has been observed over each pole-pitch, as the rotor position changes. From it, finally, a general design rule has been proposed. It permits to know -a priori- the goodness of a specific configuration of slots and poles, in terms of torque ripple.

Some design approaches have been tested to reduce the torque ripple. They are split in two categories: the geometrical modifications of the stator, and that ones of the rotor. In the first group there are the so-called: **Slot Deformation**, **Tooth Cut** and **Stator Shifting**.
Slot Deformation and Tooth Cut consist on appropriate changes in slot and tooth shape. They have the purpose to force flux lines to follow alternate paths in the iron, especially at the particular negative magnetic conditions. Differently, Stator Shifting consists on a change of position of groups of slots, which are shifted, respect their starting position, of suitable angles.

On the other hand, two different approaches have been considered for the rotor. The barriers shape has been firstly optimized by means of a multi-objective Differential Evolution **Optimization** with Pareto non-dominant sorting of the individuals. Chosen a specific geometry (considered the best by the author), a parametric **Rotor Skewing**, based on a self-made algorithm developed during the work, has been implemented.
It is unusual because it not only skews the rotor: the length of each rotor portion becomes

a variable of the algorithm. By doing it, the best combination between the different relative lengths is looked for, in terms of torque ripple reduction.

Eventually, the motor has been deeply analysed. Starting from some observations on the previous simulations, the author tried to answer the question: "Why the motor is characterized by a so important presence of a 6-th harmonic of torque?".
An analytical model of the machine has been, therefore, developed and, from it, particular harmonics combinations have been supposed. A FEM analysis, then, has confirmed and corroborate the assumptions of the analytical model.

The following conclusions can be stated from this work:

On the first analysis of the motor:

- There are some rotor positions where flux lines exhibit an opposite direction with respect to machine rotation wise. The consequence is a drop in torque behaviour, because the local torque contribution due to these flux lines is negative;

- By following how torque behaves over the pole-pitches, as the rotor position changes, it is possible to observe resting times, where the pole can be considered unloaded, alternated by peaks times, where it actively contributes in torque development. The shift between these two phases produces the torque ripple;

- It is possible to develop a general design rule: *Let's consider a generic FS SynRel machine with p pole-pairs and periodicity, t. Then, the less the ratio $N_Y = 2p/t$ is, the greater is the torque ripple of the machine.*

On the design techniques which act on the stator:

- The design technique where the best results are obtained is Stator Shifting. Torque ripple decreases down to $T_{ripple} \approx 43\%$, but the average torque decreases, too: from $T_{avg} = 1306Nm$ to $T_{avg} \approx 1085Nm$ (i.e. a reduction of 17%);

- In Stator Shifting, while ripple always more decreases as the shifting refines itself, the average torque tends to decrease to fixed values.

On the design techniques which act on the rotor:

- Proposed Optimization leads to remarkable achievements in terms of torque ripple reduction. However, results are always accompanied by a sensible reduction of average torque; the result that can be considered "the best" by the author exhibits: $T_{avg} = 1135Nm$ and $T_{ripple} = 51.7\%$;

- Also the Rotor Skewing reaches good performance. The technique, applied to the just optimized motor, permits to decrease ripple down to $T_{ripple} \approx 7\%$, but with an high cost in terms of average torque, $T_{avg} = 850Nm$.

On the deep analysis of the motor:

- Torque ripple is mainly caused by the interaction of a second harmonic ($\nu = \nu' = -2$) of electric loading, $K_{s,-2}(\xi)$, and a second harmonic of the permeance function, $P_2(\xi)$.

In Fig. 9.1 all the main results are reported for a comparison:
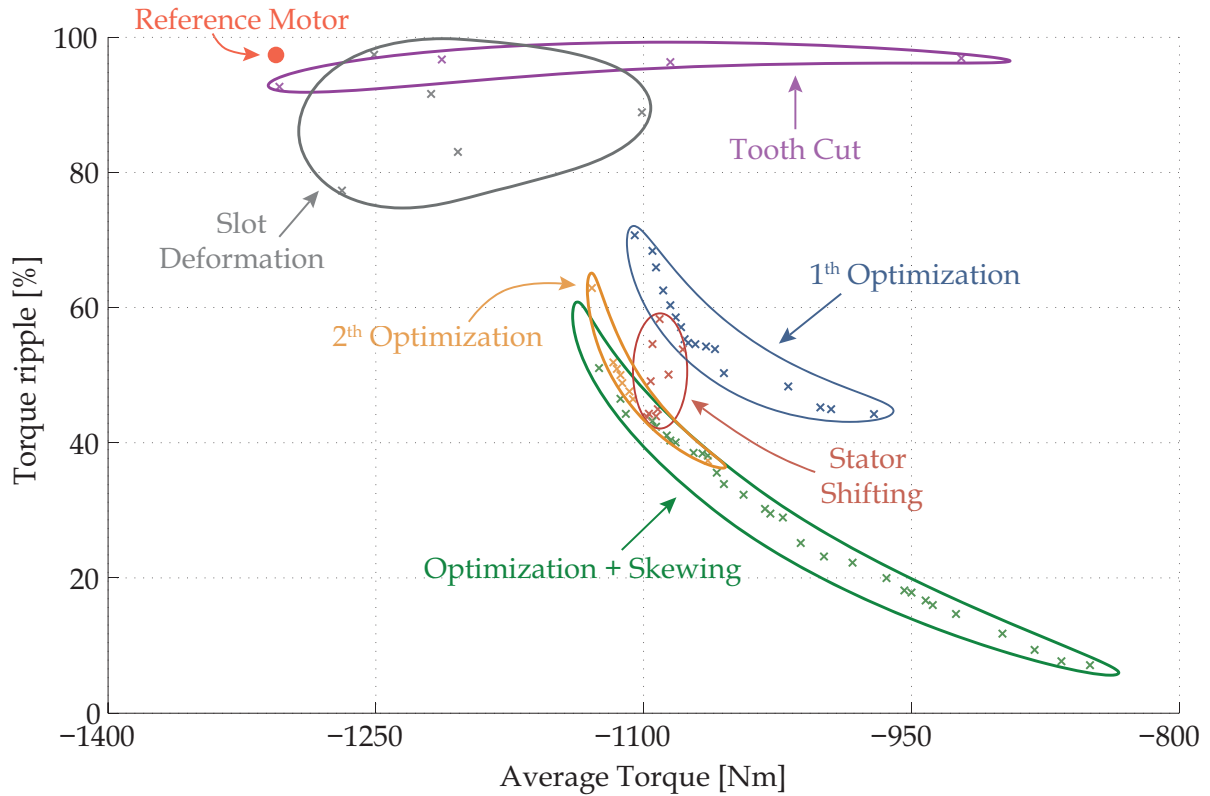
Figure 9.1: Comparison of the main results

9.1 Future developments

During this thesis, some limits have been observed. In addition, some results have reached to develop new ideas. Unfortunately, these ones have not been developed for the time limits of the work. Following, therefore, a list of the possible future developments are reported:

- **Design of experiment.** The optimization algorithm needs a huge number of input variables. This fact implies an exponential increase in the iterations number which are necessary to converge. This problem could be reduced by resorting to a preliminary optimization of the variables, called *Design of Experiment*;

- **Parametric Stator Shifting.** Stator Shifting has been studied only for a fixed value of the Total Shifting Angle, $\Delta\theta_{sh,TOT} = 7.5$ ^{deg}. A possibility could be the deep study of this technique, by understanding on what the different variables (also those ones not considered) influence.

Appendix A

Results: Slot Deformation

In this appendix, all the Slot Deformation simulations are reported. Tab. A.1 summarizes the results of these tests while, in the following pages, the torque behaviours and their harmonic contents are graphed.

		*ref.							
SE Corner		(0;0)	(0;5)	(5;0)	(5;5)	(0;0)	(0;0)	(0;0)	(0;5)
SW Corner		(0;0)	(0;0)	(0;0)	(0;0)	(0;5)	(-5;0)	(-5;5)	(0;5)
Minimum	Nm	523	604	416	495	594	674	455	663
Maximum	Nm	1795	1735	1810	1714	2049	1674	1747	1997
Average Torque	Nm	1306	1345	1208	1251	1287	1204	1191	1293
	%	100	102.99	92.50	95.79	98.55	92.19	91.20	99.01
Ripple	%	97.36	84.14	115.42	97.40	113.04	83.03	108.45	103.26

SE Corner		(0;5)	(0;5)	(5;0)	(5;0)	(5;0)	(5;5)	(5;5)	(5;5)
SW Corner		(-5;0)	(-5;5)	(0;5)	(-5;0)	(-5;5)	(0;5)	(-5;0)	(-5;5)
Minimum	Nm	686	572	559	472	392	555	585	382
Maximum	Nm	1666	1689	2043	1578	1699	1999	1564	1624
Average Torque	Nm	1269	1219	1207	1066	1308	1202	1101	1042
	%	97.17	93.34	92.42	81.62	100.15	92.04	84.30	79.79
Ripple	%	77.31	91.61	122.98	103.82	125.94	120.11	88.89	119.27

Table A.1: Slot Deformation - Comparison of results
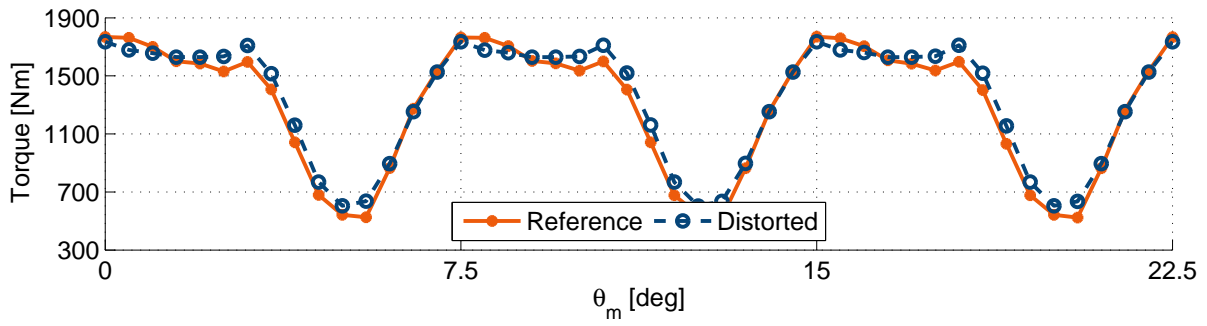
Figure A.1: (0;5)(0;0) torque ripple
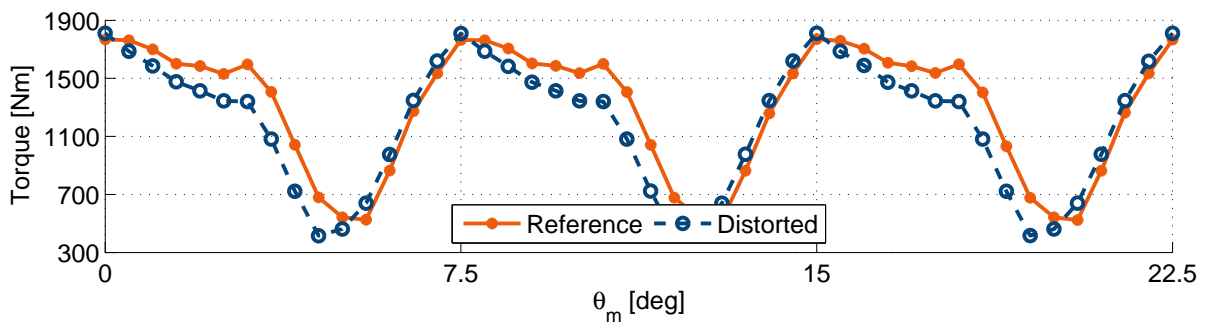
Figure A.2: (5;0)(0;0) torque ripple
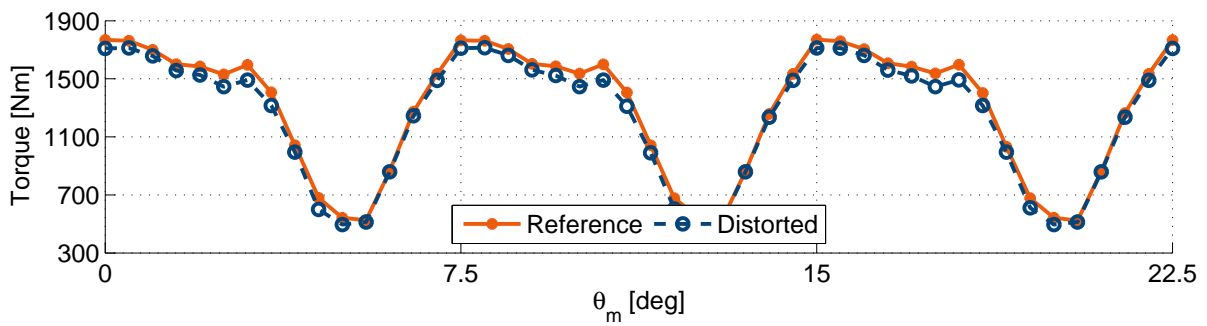
Figure A.3: (5;5)(0;0) torque ripple
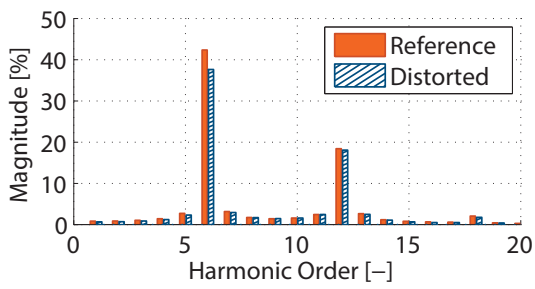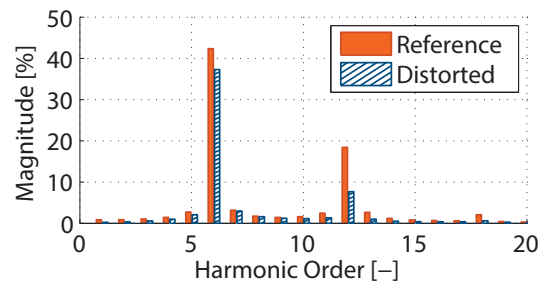

Figure A.4: (0;5)(0;0) harmonic content
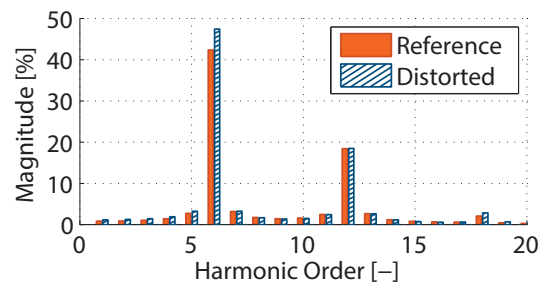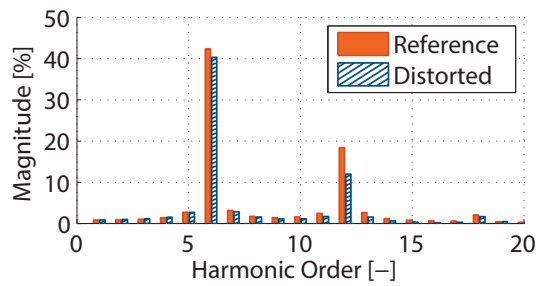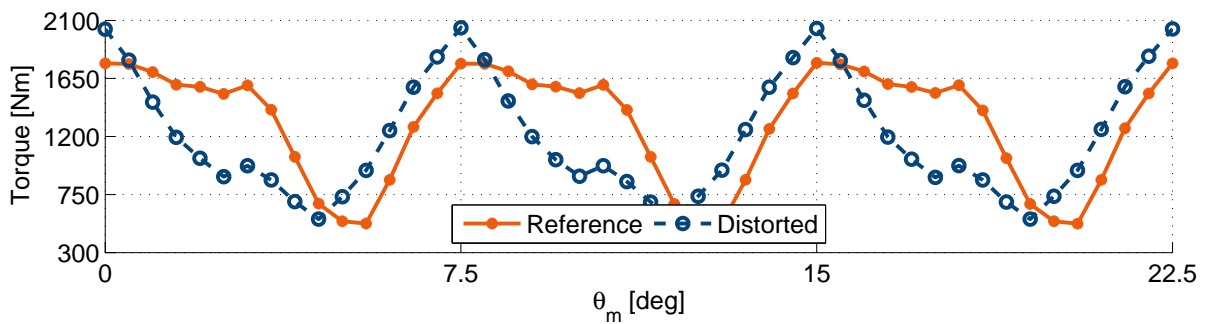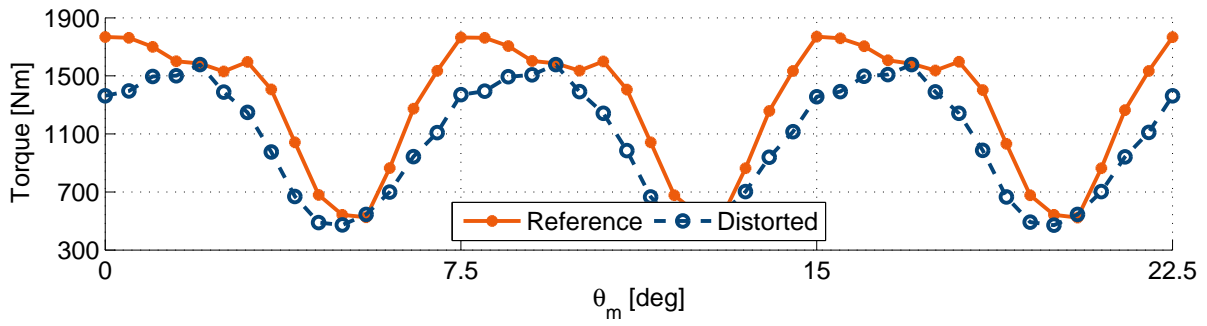

Figure A.5: (5;0)(0;0) harmonic content
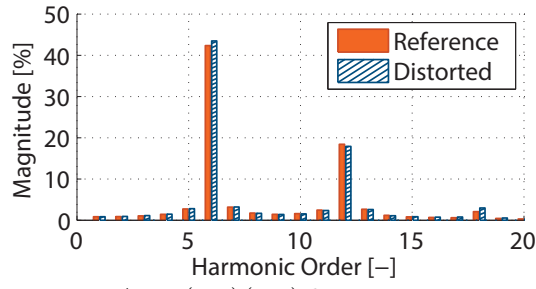
Figure A.6: (5;5)(0;0) harmonic content
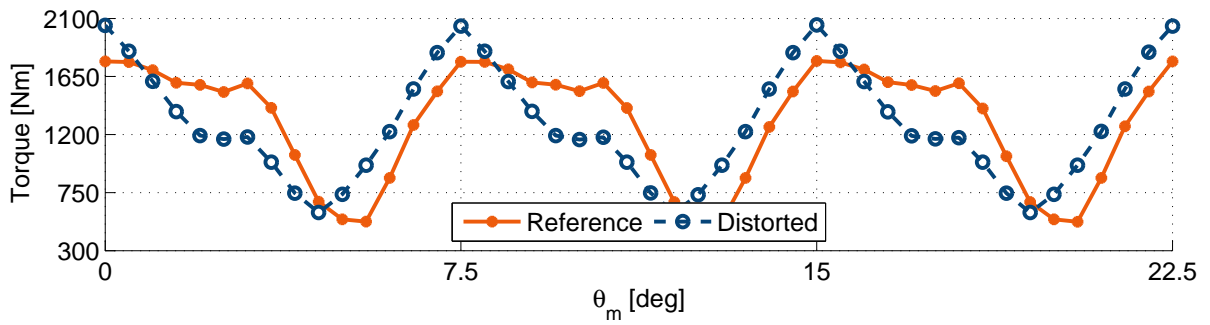
Figure A.7: (0;0)(0;5) torque ripple
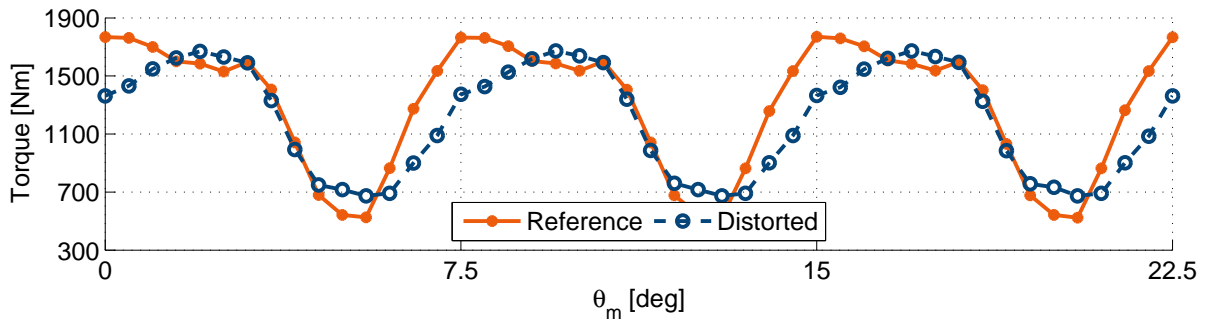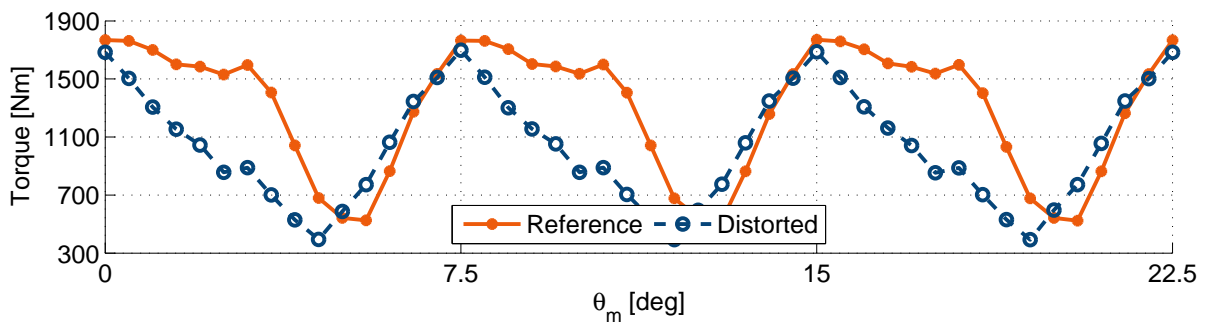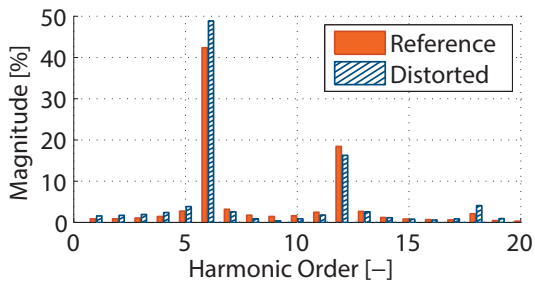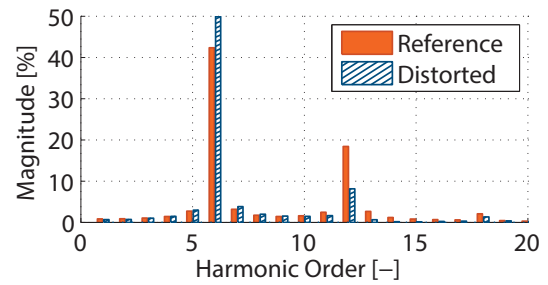

Figure A.8: (0;0)(-5;0) torque ripple
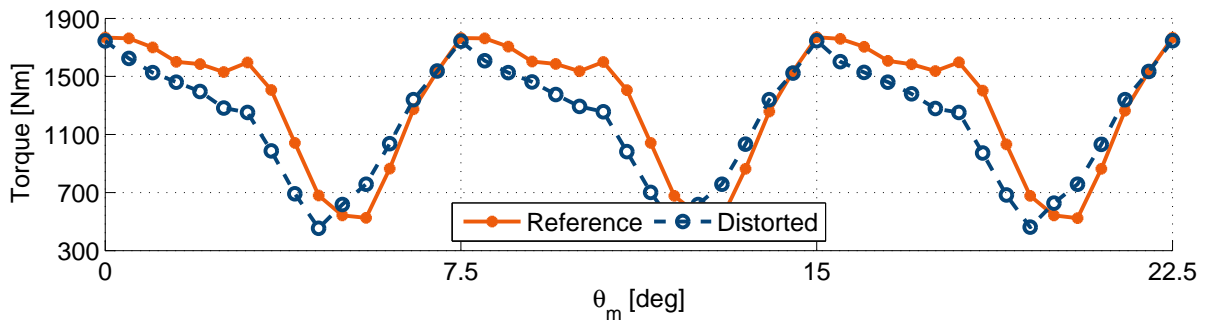
Figure A.9: (0;0)(-5;5) torque ripple
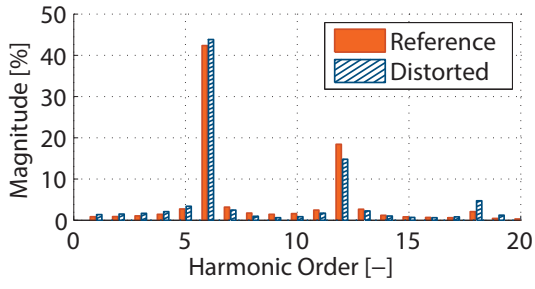
Figure A.10: (0;0)(0;5) harmonic content
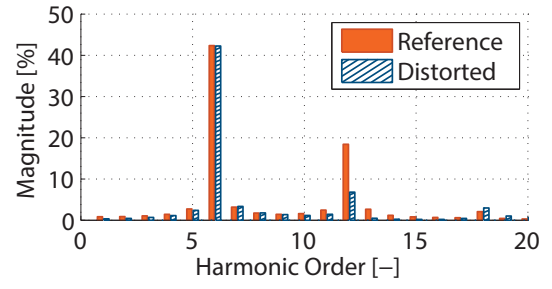
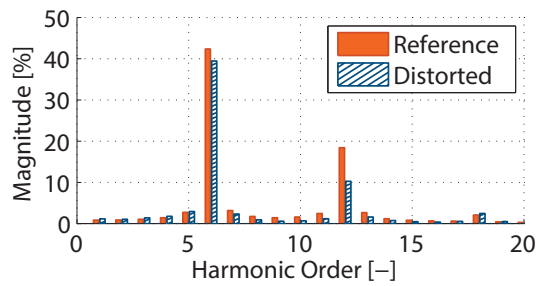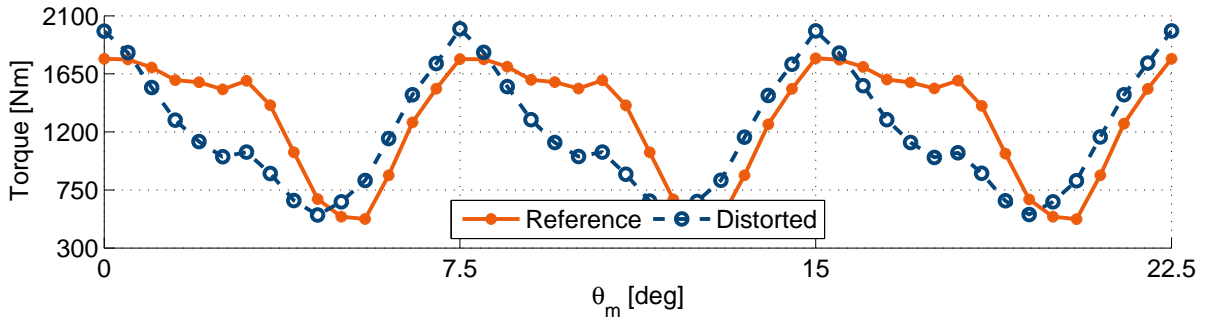Figure A.11: (0;0)(-5;0) harmonic content
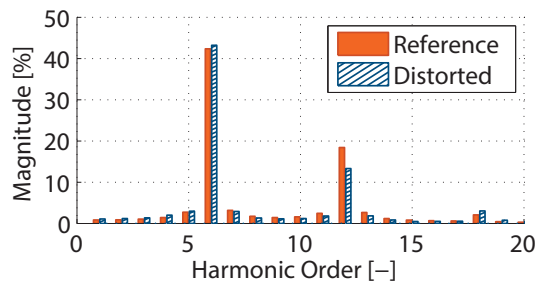
Figure A.12: (0;0)(-5;5) harmonic content
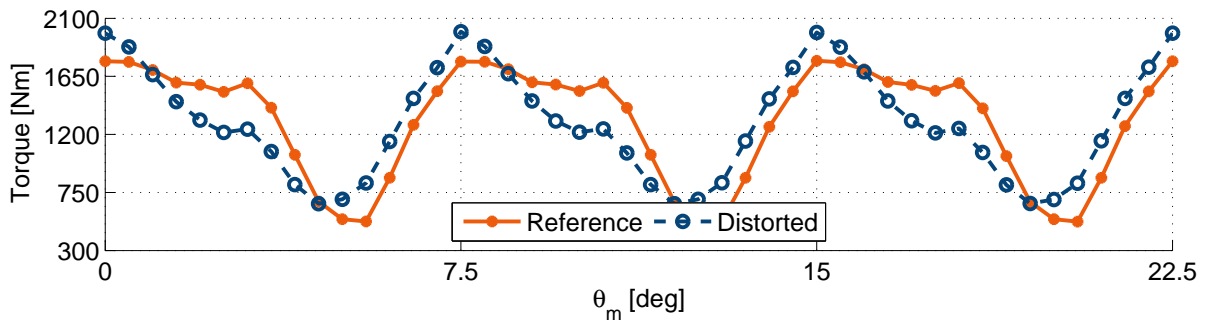
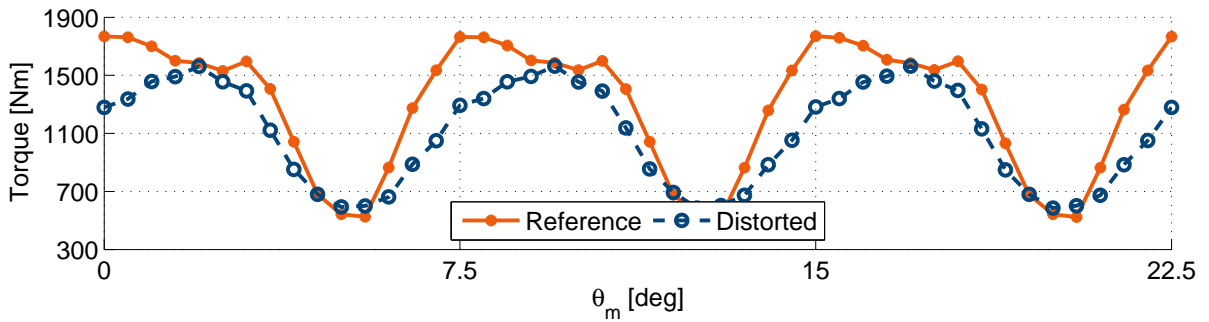Figure A.13: (0;5)(0;5) torque ripple
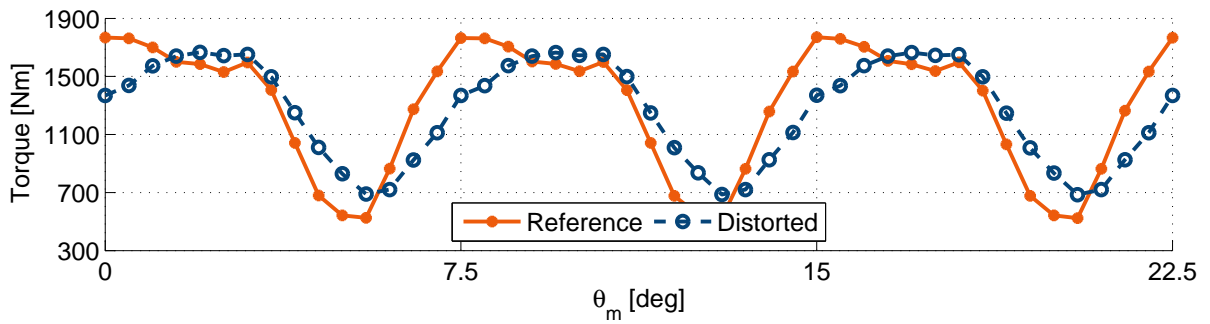
Figure A.14: (0;5)(-5;0) torque ripple
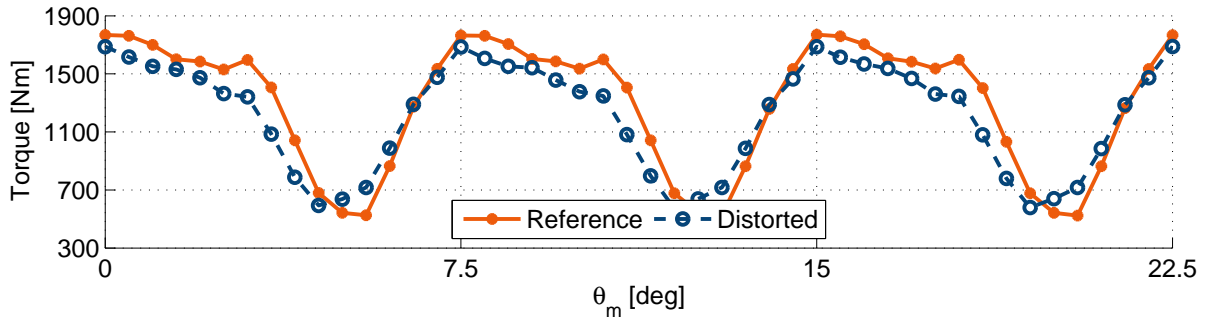
Figure A.15: (0;5)(-5;5) torque ripple
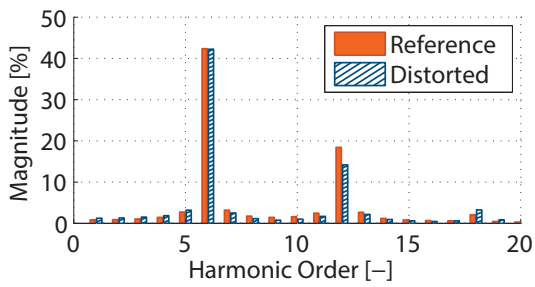
Figure A.16: (0;5)(0;5) harmonic content

Figure A.17: (0;5)(-5;0) harmonic content

Figure A.18: (0;5)(-5;5) harmonic content

Figure A.19: (5;0)(0;5) torque ripple

Figure A.20: (5;0)(-5;0) torque ripple

Figure A.21: (5;0)(-5;5) torque ripple

Figure A.22: (5;0)(0;5) harmonic content

Figure A.23: (5;0)(-5;0) harmonic content

Figure A.24: (5;0)(-5;5) harmonic content

Figure A.25: (5;5)(0;5) torque ripple

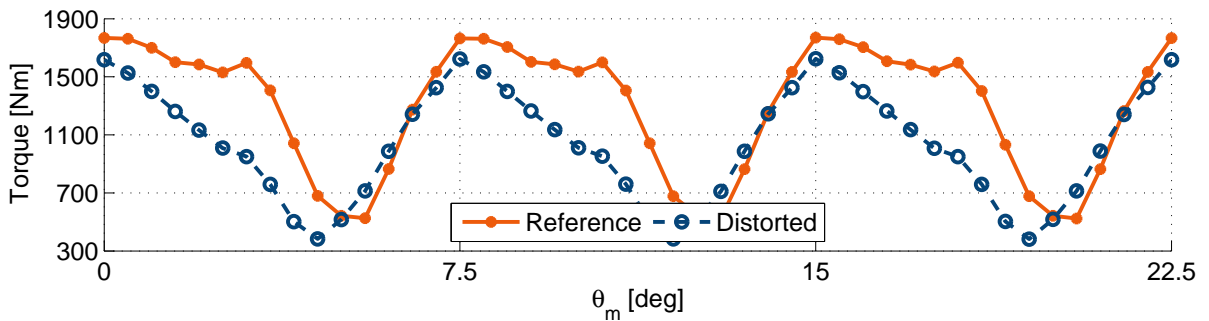
Figure A.26: (5;5)(-5;0) torque ripple
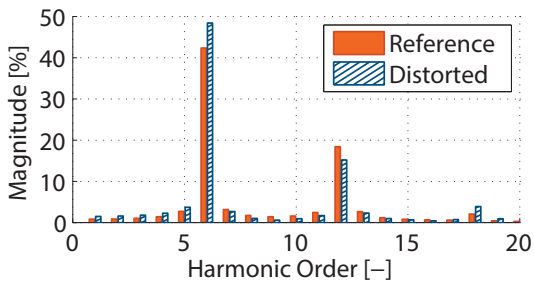

Figure A.27: (5;5)(-5;5) torque ripple
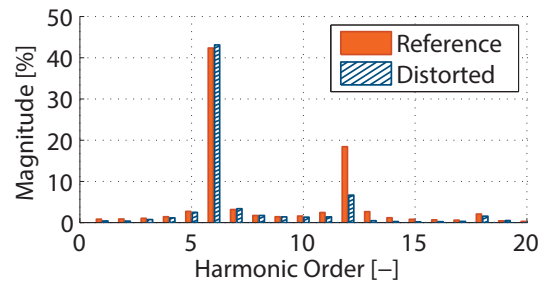

Figure A.28: (5;5)(0;5) harmonic content
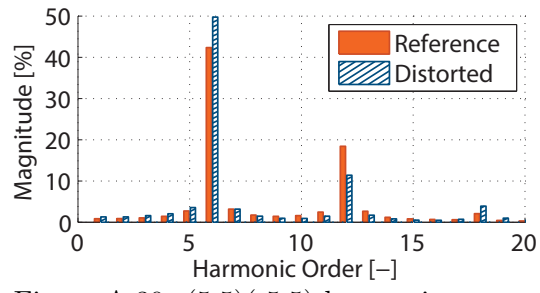

Figure A.29: (5;5)(-5;0) harmonic content

Figure A.30: (5;5)(-5;5) harmonic content

Bibliography

[1] A. Vagati, G. Franceschini, I. Marongiu, and G.P. Troglia. Design criteria of high performance synchronous reluctance motors. In *Industry Applications Society Annual Meeting, 1992., Conference Record of the 1992 IEEE*, pages 66–73 vol.1, Oct 1992.

[2] N. Bianchi and T. M. Jahns. *Design, Analysis and Control of Interior PM Synchronous Machines*, chapter 6, pages 5 – 15. Oct. 2004.

[3] N. Bianchi, M. Dai Pre, L. Alberti, and E. Fornasiero. *Theory and Design of Fractional-Slot PM Machines*. Tutorial Course Notes. IEEE, 2007 edition, Sept. 2007.

[4] P. Alotto, N. Bianchi, and E. Fornasiero. Multi-objective de nondominating-sorting optimization with archive (multidensarch) matlab script, 2010.

[5] P. Marzarotto. Analysis and design of multipole fractional-slot pm assisted rel motors: Technique to increase the torque density with respect the standard solutions. Master's thesis, University of Padua, Department of Industrial Engineering, Jul, 2015.

[6] C.M. Spargo, B.C. Mecrow, and J.D. Widmer. A seminumerical finite-element postprocessing torque ripple analysis technique for synchronous electric machines utilizing the air-gap maxwell stress tensor. *Magnetics, IEEE Transactions on*, 50(5):1–9, May 2014.

[7] M. Liwschitz-Garik and C. C. Whipple. *Alternating Current Machines*. D. Van Nostrand Company, INC, second edition, April 1961.

[8] N. Bianchi and T. M. Jahns. *Design, Analysis and Control of Interior PM Synchronous Machines*, chapter 3, pages 3 – 33. Oct. 2004.